Studies on the Magneto-transport properties of perovskite based Colossal Magneto Resistance (CMR) materials

THESIS

Submitted to
Saurashtra University, Rajkot, India

For the Degree of

Doctor of Philosophy

in Science
in the subject of Physics

By

Chetan M. Thaker

Under the supervision of

Dr. D. G. Kuberkar
Associate Professor
Department of Physics
Saurashtra University
Rajkot, India

October 2005

STATEMENT UNDER O. Ph. D. 7 OF THE SAURASHTRA UNIVERSITY

This is certified that the work presented in the thesis is my own work, carried out under the supervision of ***Dr. D. G. Kuberkar*** *and leads to some important contributions in Physics supported by necessary references.*

Chetan M. Thaker
(Research Student)

This is to certify that the work submitted for Ph.D. degree in Physics to Saurashtra University, Rajkot by ***Mr. Chetan M. Thaker*** *has been the result of more than three years of work under my supervision and is a good contribution in the field of Solid State Physics and Materials Science.*

Dr. D. G. Kuberkar
(Research Guide)
Associate Professor
Department of Physics
Saurashtra University
Rajkot

Dedicated to

My Family

consisting of broad spectrum of teachers, friends

& well-wishers

Acknowledgements

"Right knowledge is the supreme purifier, the greatest secret of all the Vedas and gods"
Shri Adi Sankaracharya

It gives me immense pleasure to express my deep sense of regards to my research guide Dr. D. G. KUBERKAR for his valuable guidance throughout the path of my research. Working with him, has indeed helped me to mature, both, as a student and a humanbeing.

It also gives me a great pleasure to express my bottomless regards to Prof. S. I. Patil, Department of Physics, Pune and his group members Dr. K. P. Adhi, Dr. Arun Banporkar, Dr. Limaye and research students Mr. Mandar Sahastrabudhe, Mr. Pankaj Sagdeo and Mr. S. Sadakale. I shall never forget their humbleness during the time of earthquake crisis by providing me research facilities and academic guidance.

My sincere regards to present and past Heads of the Department of Physics, Saurashtra University for providing me the departmental facilities. I also wish to extend my acknowledgements to all the faculty members of the Department for their moral support.

Specially, I am thankful to Dr. J. A. Bhalodia and Dr. N. A. Shah of this department for providing me moral support during this work.

I am sincerely thankful to Prof. S. K. Malik, DCMP & MS, T I F R, Mumbai for extending PPMS experimental facility and to Prof. S. K. Date, NCL, Pune for the experimental help and giving his valuable time for technical discussions during my visit to his laboratory.

I am thankful to Principal and staff members of M. D. Science College, Porbandar and Principal, Dr. A.V. Doshi and the staff members of M. V. M. Sc. &H. Sc. College, Rajkot. I specially extend my deep regards to the trustees of my college.

Now, it is time to remember my research colleagues, Dr. Sudhindra Rayprol, Dr. Krushna Mavani and especially Dr. D. S. Rana for the enjoyable moments like a family during my research. I could gain subject knowledge by the way of fruitful interactions with them. I also express my deep feelings for Mr. Jaysukh Markna, Ms. Rohini Parmar who have taken care of painstaking computational work. Also I thank Prashant, Piyush, Rujuta and Jayesh for providing me friendly atmosphere during the time of work. I would like to remember my friends Bharat Kataria, Suresh Dalsania and Dhiren Pandya. I remember all the Ph.D. students of the Department of Chemistry especially my student friends Niral Mehta (Pappu), Bhavin Thanki (Tom) and Dushyant Purohit who have helped me for the iodometric titration measurements.

My acknowledgements are also due for Mrs. Preeti D. Kuberkar and Ms. Madhura Kuberkar for the homely reception and hospitality given to me during my stay at Rajkot..

I feel short of words when I put on record the efforts of my family members in supporting me throughout these years with all the hardships they have faced for me. My heartfelt regards to my parents Mr. M. K.Thaker, Mrs. Bhagulata M.Thaker, G. K. Thaker and Mrs. Rekha G. Thaker. I pay tribute to my beloved late grandfather and late grandmother. I wish to thank my brother in law Mr. Yashawant and Mr. Milan. I also thank to my mother in law Ms. Vijyaben Jani for the hospitality during the time of research.

Last but not least, I have no words to express my feelings for my wife MEERA and my beloved son UTSAV at the time of this submission who understood me through out my research career.

Chetan M. Thaker

I thankfully acknowledge University Grants Commission (UGC), New Delhi, India for providing me Teacher fellowship during April 2000 - March 2002 under the UGC - FIP IX plan program.

October, 2005 Chetan M. Thaker

Abstract

The discovery of phenomenon of magneto resistance (MR) which is measure of resistivity drop when subjected to magnetic field and its potentiality in application in magnetic memory devices has spurred an interest in scientific community to synthesize new materials exhibiting large magneto resistance. The studies on property of MR in metals, semiconductors and alloys became field of interest. The discovery of "giant magneto resistance" observed in artificially grown alternate ferromagnetic and non-magnetic metallic layers such as Fe/Cr, Cu/Cr as high as 75% under larger fields triggered the new era of research for still better materials. The next breakthrough in MR materials came with the observance of MR effect in rare earth manganite oxides. In 1993, R. Von Helmolt et. al discovered that $La_{2/3}Ba_{1/3}MnO_3$ exhibit huge magneto resistance around room temperature with many interesting inter related phenomena. The strength of MR in many similar polycrystalline compounds as high as 90% under a few Tesla led the scientists to coin a new term called "colossal magneto resistance (CMR)". The strength of CMR effect in the metallic oxides induced interest in researchers to exploit these compounds for the possible application. Unlike artificially grown metallic multilayers where extrinsic factors such as the interface between the two layers, roughness and grain structure govern the magneto resistance, these compounds have ionic size dependent intrinsic property responsible for colossal magneto resistance. This intrinsic factor in this ABO_3 type of perovskite, with limits on the size of A and B site cations for occurrence of CMR effect, can be controlled by the compositional changes in the compound. The interplay with size of the cations to alter the MR properties of the manganite perovskites evolved plenty of scope in further research in related materials.

The basic manganite oxide $ReMnO_3$ where Re = La, Pr, Nd is a paramagnetic insulator at all the temperatures. It, however, exhibits paramagnetic to antiferromagnetic transition around 150 K. The optimum divalent cation doping at A site drives the resulting material to exhibit properties such as coincident insulator – metal (I-M)

transition and paramagnetic – ferromagnetic (PM-FM) transition. The maximum CMR effect occurs around this coincident transition temperature. Re and Mn ions exist in +3 oxidation state in $ReMnO_3$ perovskite. The divalent Ca^{2+}, Sr^{2+}, Ba^{2+} and Pb^{2+} cations substitution at A site drives Mn at B site to exist in mixed valent (Mn^{3+}/Mn^{4+}) state which is responsible for most of the transport and magnetic properties of the perovskite. Due this mixed valent state of Mn, these compounds are also called as mixed valent manganite oxides. The conduction in these oxides is explained by a phenomenon discovered by C. Zener in 1951 called as "Zener-Double Exchange (ZDE)". All the transport mechanisms such as ZDE occur through Mn – O – Mn network, where as A cation is not directly involved in any conduction mechanism. The Mn^{4+} valence state is formed due to substitution of same amount divalent cation at A-site. The 3d shell of Mn has non-degenerate spin up and spin down states. Four of the 5d spin up orbitals is filled while all the spin down orbitals are vacant in Mn^{3+} ion. The crystal field of oxygen lifts the degeneracy of the 5d orbitals and results in splitting into lower energy 3 t_{2g} and higher energy 2 e_g orbitals. The 2 e_g orbitals are further split into two energy levels called Jahn – Teller splitting that cause orbital ordering of MnO_6 octahedra along the planes where last filled electron lies just at the fermi level. The hole doping removes Jahn – Teller distortion along the planes. At Mn^{3+} - O^{2-} – Mn^{4+} coupling, the last e_g electron in Mn^{3+} feels a net energy difference and it becomes delocalized via O^{2-} to Mn^{4+}. This process of Zener Double exchange accounts for both the metallic and ferromagnetic character of the material below a certain temperature called transition temperature. The phenomenon of ZDE is possible only if the spins of the alternate manganese ions are aligned parallel.

The electrical and magnetic transitions start appearing only after a certain amount of Mn^{4+} has been created and disappears at excess doping of divalent cation. The best transport and magnetic properties appear for $Re_{1-x}A_xMnO_3$; x = 0.33 substituted system. The maximum magnetic disorder occurs at transition temperature, so the application of magnetic field forces the parallel alignment of spins causing huge drop in resistivity to favor ZDE and hence maximum CMR effect. The lattice electron coupling or the polaron formation localizes the e_g electron to show insulating behavior above T_c. The A site cation

radius distorts the structure of the perovskite that controls the buckling of the Mn-O bonds. The smaller size cation buckles Mn-O-Mn bond angle from its ideal 180-degree geometry. The various inter-related phenomena can be summarized as follows. The divalent doping in orbital ordered $ReMnO_3$ perovskite removes the distortion of the MnO_6 octahedra, the lattice electron coupling above transition temperature makes the manganite system paramagnetic insulator, competition between ZDE and super-exchange results in peak resistivity, ZDE below T_c explains the ferromagnetic metallic character, the charge ordering at half doped system makes the system antiferromagnetic insulator at second order transition and the maximum CMR effect at magnetically disordered region near the transition temperature.

As stated earlier, A site cation does not involve in any conduction mechanism but has its ionic size effect on the transport and magnetic properties. A parameter called as "Goldschimdt tolerance factor" relates the different site ionic radii to the transition temperature. It is given as

$$t = (\langle r_A \rangle + r_O) / \sqrt{2}(\langle r_B \rangle + r_O)$$

Where,

$\langle r_A \rangle$ = average A site cation radius

$\langle r_B \rangle$ = average B site cation radius

r_O = radius of oxygen anion

t is 1 for ideal cubic structure perovskites. Electrical and magnetic transition occur for $0.90<t<1$, where structural transitions from cubic to rhombohedral to monoclinic to orthorhombic occur as t approaches from 1 to 0.90. Since doping at B site directly impedes the conduction process, it is very sensitive to unlike cation and only a small amount of substitution is sufficient to alter the transport properties of manganites. Comparatively, the doping at A site can be done more flexibly in large range of doping concentrations. The isovalent light rare earth substitutional studies have been done by various researchers to study the effect of cation size mismatch and average A site cation radius effect on the electronic and magnetic transitions. Only some light rare earth like La, Pr, Nd and Sm based manganite systems show the CMR properties whereas heavy rare

earth like Gd, Ho, Dy etc. due to smaller ionic radii results in the buckling of Mn – O bonds significantly such that e_g band itinerant electron gets localized permanently to their parent atoms. However, these heavy rare earth metals have been replaced partially with A site cation with a fixed carrier density.

Depending upon the transition temperatures and related CMR effect, the manganite systems have been classified as low bandwidth, intermediate bandwidth and large bandwidth manganite systems. The system such as $Pr_{1-x}Ca_xMnO_3$ in which ferromagnetic metallic state is not stabilized and a ferromagnetic insulating state exists in the range between x = 0.15 – 0.30 are classified as low bandwidth manganite systems. This system represents a stable charge-ordered state in a broad density region between x = 0.30 – 0.75. These manganites exhibit I-M transition when subjected to magnetic field, pressure and when exposed to X-rays. Since there is large buckling at Mn-O bond due to smaller size of Pr, the application of even weaker magnetic field results in significant amount of CMR effect. The manganite like $La_{0.7}Sr_{0.3}MnO_3$ shows the transition temperature well above the room temperature around 370 K, so labeled as large bandwidth manganite system. It is believed that, in this compound the hopping amplitude for electrons in e_g band is larger than in other manganites as a consequence of the sizes of the ions involved in chemical compositions. Large bandwidth systems have spins almost parallel at the Mn-O couplings, so the application of magnetic field does not produce any significant change in resistivity in already magnetically ordered region. The drawback of large bandwidth system is that, the large transition temperature is coupled to small CMR effect that has restricted these materials from application point of view. The third type of manganite system that has characteristics of both the low and large bandwidth systems and in which the research is being carried out by a sizeable fraction of researchers is called as intermediate bandwidth manganite system. $La_{1-x}Ca_xMnO_3$ is a typical example of such a system. This compound represents the presence of robust ferromagnetic metallic state. It has also features that represent deviation from double-exchange behavior, including the existence of charge ordered and orbital ordered state. Recently the work is also being focused on intermediate

to low bandwidth materials since these are the ones that exhibit the largest CMR effect, which is associated with the presence of charge ordering tendencies.

Along with the hole-doped manganite systems, efforts have been put to investigate the possibility of obtaining colossal magneto resistance in electron-doped manganites. The compounds like $La_{0.7}Ce_{0.3}MnO_3$ have been found to exhibit several interesting transport and magnetic properties that made the scientific community to synthesize and characterize more electron doped systems. In hole doped systems when average charge on A site is reduced the manganese ions go in a mixture of Mn^{3+}/Mn^{4+} valence states. On the other hand, in electron-doped systems the average charge on A site is increased by aliovalent cation doping at rare earth site. The increased charge on A site will be able to drive the manganese ions in a mixture of Mn^{3+}/Mn^{2+} states. Mn $^{2+}$ valence state of manganese is, like Mn^{4+} valence state, a non Jahn – Teller ion. The process of Zener Double Exchange should operate between two adjacent Mn^{3+} and Mn^{2+} ions in the same way as it operates between Mn^{3+} and Mn^{4+} ions. One would, therefore, expect electron-doped manganites to exhibit metal – insulator transition and ferromagnetism associated with colossal magneto resistance.

Keeping in mind the role of A-site cation doping in modifying the structural, transport and magnetic properties of intermediate bandwidth system like $L_{1-2x}Pr_xCa_xMnO_3$, an attempt is made to investigate above mentioned properties of this system in the context of variation in magnetic and electrical transition temperatures and magneto resistance using X-ray diffraction, resistivity, magnetization, and magneto resistance studies. Also, during the course of present work, the effect of substitution of divalent cations like Ca, Sr and Ba at A site is studied in the light of change in structural, transport, magneto transport and magnetic behavior of the system under investigation. Present work also comprise of research efforts carried out on the possible role of electron doping at A site due to higher valence cations like Ce^{4+}, Th^{4+} and Mo^{6+} etc. in modifying and observing the CMR effect in $Re_{1-x}A_xMnO_3$; A = Th and Mo.

Contents of the thesis – An overview

The first chapter of the thesis deals with the introduction to the subject, historical development of the manganite oxides, the definition of colossal magneto resistance, various phenomena and mechanisms governing mixed valent manganite oxides. Second chapter comprise of the synthesis, characterization techniques and tool used to study CMR materials. Chapter 3 is focused on the study of simultaneous doping of Pr and Ca in $LaMnO_3$ perovskite. The simultaneous doping of Pr and Ca are interesting to study the effect of carrier density and cation size on the transport, magneto transport and magnetic properties of the system. Chapter 4 deals with effect of larger size divalent cation like Sr and Ba doping on transition temperatures and CMR effect in carrier concentration optimized compositions. Chapter 5 describes the results pf the studies on the different electron doped systems. More than +1 aliovalent cation substitution induces the transport and magnetic properties of the CMR materials in the resulting system. It also includes a section that deals with the doping of Th^{4+} at Re^{3+} site that makes it an electron-doped system in $LaMnO_3$ perovskite. In nutshell, this chapter focuses on our effort to establish an electron-doped system exhibiting CMR properties.

Following is a brief discussion of the different manganite systems studied during the course of present doctoral work.

Chapter 1-2 Introduces to manganite and synthesis and characterization techniques, experimental tools used in the present work.

Chapter 3 is devoted to the Pr-Ca doped $La_{1-2x}Pr_xCa_xMnO_3$ ($x = 0.00 – 0.30$) manganite system.

The effect of divalent cations like Ca^{2+}, Sr^{2+}, Ba^{2+} etc is well studied, as different concentrations of divalent cation are responsible for the amount of charge carrier density. It is established that 33% percent hole doped system shows the best transport and magnetic properties. The cation sizes of Ca^{2+} and La^{3+} are comparable, so the different amount of divalent cation, Ca^{2+}, doping shows only the effect of carrier density. The simultaneous substitution of Pr – Ca is aimed to elucidate simultaneously the effect of cation size and carrier density on the transport and magnetic properties of the resulting

system. Pr being smaller cation reduces the average size of the A site cation and has inherent property of mixed phase formation. Due to reduced average ionic size, the system lies between intermediate and low bandwidth manganites. The CMR effect will be interesting factor as nearly low bandwidth manganite category shows maximum MR% at relatively weaker fields.

Chapter 4 Devoted to the bandwidth modification by Sr^{2+} and Ba^{2+} substitution in $La_{0.5}Pr_{0.2}Ca_{0.3}MnO_3$ manganite.

Sr^{2+} and Ba^{2+} being larger size cations, modify the bandwidth of the parent manganite. The substitution of these cations increase the e_g band electron hopping amplitude and hence enhance the transition temperatures along with structural transformations. The substitution of these cations is aimed at reviving the transition temperature up to room temperature. The $La_{0.5}Pr_{0.2}Ca_{0.3}MnO_3$ manganite exhibits transition temperature around 135K with large CMR effect under relatively weaker fields. This composition shows 47% of CMR effect under just 1 Tesla field. This huge CMR effect prompted us to modify the bandwidth by larger size cation substitution and its possible effect on the electronic transitions and magnetic properties. Since only a small amount of Sr^{2+} doping may increase the transition temperature significantly, it becomes imperative to observe the relation between the T_c, CMR effect and magnetization in the applied fields. Similar to the effect of Sr^{2+} substitution, substitution of Ba^{2+} at A site will help us to under stand whether the average A site cation radius plays a prominent role or the individual effect of cations dominate in defining the electrical and magnetic transition temperatures.

Chapter 5 is devoted to electron doped manganite systems.

There have been lots of efforts to establish electron-doped systems, exhibiting the properties similar to hole doped systems but the success is partially achieved. $La_{1-x}Ce_xMnO_3$ electron doped system is the one, which has been widely studied to exhibit most of the inter-related properties, like that in hole doped systems. We synthesized $Y_{0.8}Mo_{0.2}MnO_3$ and investigated the effect of more than +1 aliovalent cation substitution on the structural and electronic behavior. The synthesis of thorium-doped manganite with

stoichiometric compositions $Re_{1-x}Th_xMnO_3$; Re = La, Nd further reflects our efforts to still find a scope to establish the electron doped systems. The drawback in all the electron-doped systems is limitation in purity of structural phase formation. Still these systems have exhibited some interesting properties to be discussed in detail in thesis.

SCOPE FOR THE FUTURE WORK

The structural, transport and magnetotransport measurements on Pr-Ca doped LPCMO and Pr-Ca/Ba/Sr doped LPCMO, LPCSMO and LPCBMO systems of manganites have revealed several interesting properties of these compounds from the fundamental understanding of the cause of CMR behavior, structure-property correlation and the application potentiality of some of them based on the observation of pronounced MR behavior in relatively low applied magnetic fields. Also, the results of the studies on obtaining single phase electron doped manganite system have lead to explore the possibility of synthesizing them using Chemical Solution Deposition (CSD) technique.

From the point of view of future scope of fundamental work on the similar manganite systems, it would be interesting to perform temperature dependant Neutron Diffraction (ND) measurements and its magnetic refinement for understanding the nature and cause of magnetic phase transitions exhibited by these materials. In addition, one should try to study the effect of Swift Heavy Ion (SHI) irradiation on the modifications in microstructural and magnetotransport behavior of doped manganites.

From application point of view, it would be interesting to grow the multilayered thin film structures of the type LPSMO/Al_2O_3/LPSMO, to increase the MR, TCR and FCR property of these compounds.

At the end, it can be mentioned that, the interesting results obtained during the course of present work will lead to further useful investigations in the manganite research.

Index

Chapter – I

Introduction to Magneto resistance materials

1.1 Magnetism based technology

The most promising MRAM consist of memory cells based on magnetic tunnel junctions (MTJ). The underlying physical principle differs from that of GMR. In an MTJ, two ferromagnetic layers are separated by an insulating tunnel barrier. Under a small-applied voltage, electronic current can pass perpendicularly through the device by tunneling across the insulating barrier (in contrast with all other devices mentioned above for which the current flow is horizontal). The ease with which the current can tunnel depends on the relative magnetization of the two ferromagnetic layers. When the magnetizations in the two layers point in the same direction, there is a high probability that electrons can tunnel and the resistance of the memory is low while in the case of opposite directions, the resistance of the memory is high.

1.1.1 Magnetic recording technology

However the GMR head works in a nutshell (without getting into quantum physics that would make your brain melt-and mine.) When the head passes over a magnetic field of one polarity (say, a "0" on the disk), the free layer has its electrons turn to be aligned with those of the pinned layer; this creates a lower resistance in the entire head structure. When the head passes over a magnetic field of the opposite polarity ("1"), the electrons in the free layer rotate so that they are not aligned with those of the pinned layer. This causes an increase in the resistance of the overall structure. The resistance changes are caused by changes to the spin characteristics of electrons in the free layer, and for this reason, IBM has named these structures spin valves. If you imagine a plumbing pipe with a rotatable shut-off valve, that's the general concept behind the name.

1.1.2 Materials exhibiting magnetoresistance

The discovery of phenomenon of magnetoresistance (MR), a measure of resistivity drop when subjected to the magnetic field and its potentiality in applications in magnetic memory devices, has spurred an interest in the scientific community to synthesize new materials exhibiting large magnetoresistance, under low fields at room temperature.

The colossal magnetoresistance (CMR), as the name implies, is the phenomenon of dramatic changes in resistance attained upon application of a magnetic field. Although it was discovered nearly half a century ago [1], there has been heightened interest in the past few years, not only from a fundamental point of view but also from applications point of view.

The MR phenomenon was first reported in 1879 by Edwin Hall, known as Hall – effect [2] in which it was found that, when a conductor is placed in magnetic field (H_x) perpendicular to the direction of current flow (J_y), voltage (E_z) develops across the conductor. The field along the conductor E_y is proportional to the current density J_y so that, $\rho(H) = E_y / H_x$. This expression gives the magnetoresistance MR often called as the Hall Effect (HE) which describes the magnetotransport phenomenon.

a. Magnetoresistance in metals and alloys

Free electron theory assumed that the resistance of a conductor perpendicular to the uniform magnetic field should not depend upon the strength of the field. However it does not show any magnetoresistance due to asymmetric nature of Fermi surface. But in certain cases like copper, silver and gold a small transverse magnetoresistance can be observed, normally less than 1% under few Tesla magnetic fields.

In fact, no single feature of the material or theory can explain the entire MR phenomenon. In normal metals, the Lorentz force is the cause of deviation of electrons trajectories.

The situation is drastically different in magnetic metals and alloys. Here the effect of Lorentz force is too small with respect of the additional effects that contribute to MR.

b. Magnetoresistance in semiconductors

The large MR has been observed in doped magnetic semiconductors, such as $Cd_{1-x}Mn_xSe$. In these types of materials, MR is maximum when the carrier concentration is critical across the metal-insulator boundary because of spin-dependent scattering.

c. Magnetoresistance in alloys

The mixture of gold and gadolinium such as $Au_{0.05}Gd$ alloy exhibits isotropic negative magnetoresistance due to the exchange scattering. But in the case of $Au_{0.98}Tb$ alloy, magnetoresistance predominantly arise from quadrupole scattering giving positive and negative values for longitudinal and transverse fields, respectively.

d. Magnetoresistance in magnetic multilayers and oxides

The giant magnetoresistance (GMR) was discovered in 1988 by Baibich et al [3] in which, the resistance of certain ferromagnetic metals such as Fe and Co drops dramatically as a magnetic field is applied. It is described as a giant since it is much larger effect than had ever been previously seen in metals. The effect is most usually seen in magnetic-nonmagnetic multilayered structures [4].

The colossal magnetoresistance (CMR) is exhibited by manganite oxides and is caused by the suppression of spin fluctuation in strong magnetic field, near a magnetic transition temperature [5, 6]. Around ordering temperature, negative magnetoresistance can reach value much larger even than GMR type materials which is correlated with ferromagnetic ordering. An insulator to metal transition is found usually in the manganese based perovskites type structure having general formula $R_{1-x}A_xMnO_3$ (R: La, Pr, Sm, Nd, Rare Earth metal: A= Sr, Ca, Ba, Pb). Magnetism and metallic behavior is based on double exchange mechanism will be discussed in detail later in this chapter.

1.1.3. Giant magnetoresistance (GMR) and Colossal magnetoresistance (CMR)

a. GMR

The effect is mostly seen in magnetic multilayered structured, where two magnetic layers are closely separated by a thin spacer layer a few nanometer thick [3,4]. It is analogous to a polarization experiment. Suppose the first magnetic layer allows electrons in only one spin state to pass through it easily and if second magnetic layer is aligned then that spin channel can easily pass through the structure and the resistance is low enough. If the second magnetic layer is misaligned then spin channel cannot get through the structure easily and the electrical resistance is high [7].

The band structure in a ferromagnet is exchange split, so that the density of the states is not the same for spin up and down electrons at Fermi level and hence the scattering rates are different for electrons with different spins. Actually, these ideas were used earlier in 1936 by Sir Nevill Mott to explain the sudden decrease in resistivity of ferromagnetic metal as it was cooled through the Curie point.

b. CMR

In 1993, R. Von Helmolt et al [5] discovered that $La_{2/3}Ba_{1/3}MnO_3$ exhibit huge magnetoresistance around room temperature with many interesting inter related phenomena. The strength of MR observed in many similar polycrystalline compounds as high as 90% under a few Tesla led the scientists to coin a new term called "colossal magneto resistance (CMR)" [5-8]. The observation of CMR effect in the metallic oxides induced interest in researchers to exploit these compounds for the possible applications. Unlike artificially grown metallic multilayers where extrinsic factors such as the interface between the two layers, roughness and grain structure govern the magnetoresistance, these compounds have ionic size dependent intrinsic properties responsible for colossal magnetoresistance. These intrinsic factors in this ABO_3 type of perovskite, with limits on the size of A and B site cations for occurrence of CMR effect, can be controlled by the compositional changes in the compound [7]. The interplay with size of the cations to alter the MR properties of the manganite perovskites evolved plenty of scope in further research in related materials.

The basic manganite oxide $ReMnO_3$ where Re = La, Pr, Nd is a paramagnetic insulator at all the temperatures, however, exhibits paramagnetic to antiferromagnetic transition around 150 K. The optimum divalent cation doping at A site drives the resulting material to exhibit properties such as coincident insulator – metal (I-M) transition and paramagnetic – ferromagnetic (PM-FM) transition. The maximum CMR effect occurs around this coincident transition temperature. Re and Mn ions exist in +3 oxidation state in $ReMnO_3$ perovskite. The divalent Ca^{2+}, Sr^{2+}, Ba^{2+} and Pb^{2+} cations substitution at A site drives Mn at B site to exist in mixed valent (Mn^{3+}/Mn^{4+}) state which is responsible for most of the transport and magnetic properties of the perovskite. Due this mixed valent state of Mn, these compounds are also called as mixed valent manganite oxides. The conduction in these oxides is explained by a phenomenon discovered by C. Zener in 1951

[9] called as “Zener-Double Exchange (ZDE)”. All the transport mechanisms such as ZDE occur through Mn – O – Mn network, where as A cation is not directly involved in any conduction mechanism. The Mn^{4+} valence state is formed due to substitution of same amount of divalent cation at A-site. The octahedral crystal field of oxygen octahedra (MnO_6) lifts the five fold degenerate Mn 3d orbitals into three lower energy t_{2g} (d_{xy}, d_{yz} & d_{zx}) and two higher energy e_g ($d_{x^2-y^2}$, d_{z^2}) orbitals. Further, the octahedral crystal field split the two e_g orbitals into two energy levels which is called Jahn – Teller splitting that cause orbital ordering of MnO_6 octahedra along the planes where last filled electron lies just at the fermi level. The hole doping removes Jahn – Teller distortion along the planes. At Mn^{3+}- O^{2-} - Mn^{4+} coupling, the last e_g electron in Mn^{3+} feels a net energy difference and it becomes delocalized via O^{2-} to Mn^{4+}. This process of Zener Double exchange accounts for both the metallic and ferromagnetic character of the material below a certain temperature called transition temperature [10]. The phenomenon of ZDE is possible only if the spins of the alternate manganese ions are aligned parallel.

The A site cation in ABO_3 type perovskite manganite does not involve in any conduction mechanism but has its ionic size effect on the transport and magnetic properties. A parameter called as “Goldschimdt tolerance factor” relates the different site ionic radii to the transition temperature [7, 11]. It is given as

$$t = (\langle r_A \rangle + r_O) / \sqrt{2}(\langle r_B \rangle + r_O)$$

where, $\langle r_A \rangle$ = average A site cation radius

$\langle r_B \rangle$ = average B site cation radius

$\langle r_{O>} \rangle$ = radius of oxygen anion

The value of tolerance factor (t) is 1 for ideal cubic structure perovskites. Electrical and magnetic transition occur for $0.90 < t < 1$, where structural transitions from cubic to rhombohedral to monoclinic to orthorhombic occur as t approaches from 1 to 0.90.

1.2 Origin of magnetoresistance in manganite perovskite

1.2.1 The structural and magnetic properties of $Re_{(1-x)}A_xMnO_3$ perovskite

The physics of manganites is very rich. Manganites exhibit a variety of phases such as paramagnetic state, ferromagnetic metal or insulator, antiferromagnetism, canted antiferromagnetism and charge ordering. Several interesting phenomena including the colossal MR are related to the metal-insulator and magnetic transitions between these phases. Many properties of CMR materials can be tuned by external parameters such as

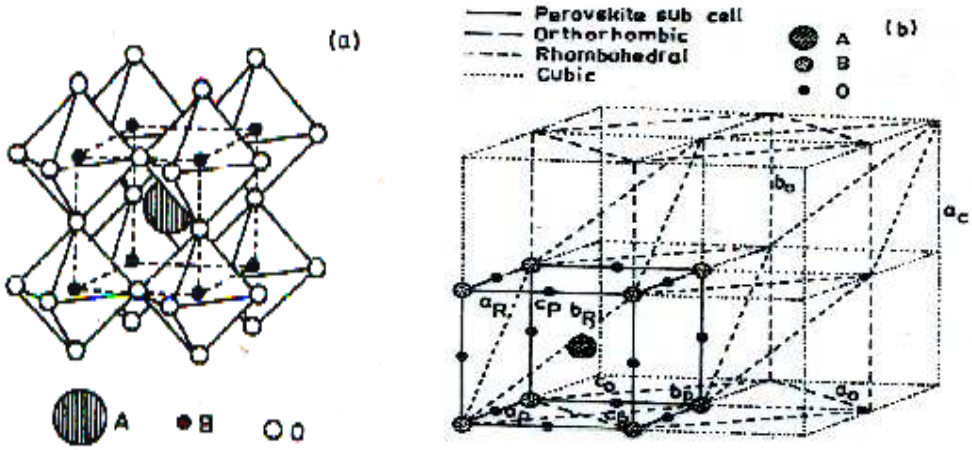

Figure 1.1 **(a)** The cubic perovskite structure. A – larger rare earth cations like La. B – smaller cations like Mn, Co. O – Oxygen anion.

(b) The orthorhombic, rhombohedral and cubic unit cell of perovskite structure. Ref [10].

temperature T, Magnetic field H or by the Chemical Pressure. Many striking electronic properties of these systems are due to strong coupling of electrons to the dynamical lattice distortions. The lattice is the crystal cell of the perovskite type.

The manganese oxides forms in the so-called perovskite crystal lattice (Fig. 1.1). It is a body centered cubic (bcc) structure with a rare earth atom (for example La) at the center (A-site), 8 Mn atoms at the corners (B-site) of the cubic cell and one atom oxygen midway between each pair of Mn atoms. Each cubic cell comprises one La atom, One Mn The valence of La (and other members of La family such as Pr) is +3, the valance of O in

atom (because only $1/8^{th}$ of each of 8 Mn atoms belongs to the cubic cell) and three O atoms (because only $1/4^{th}$ of each of 12 oxygen atom belongs to the cell).

This composition is -2 so the valance of Mn should be +3 to fulfill the charge neutrality. In other words, an undoped lanthanum manganite ($LaMnO_3$) compound corresponds to the ionic composition is La^{+3},Mn^{+3},O_3^{-2}. The electronic configuration of Mn atom is $3d^5\ 4s^2$, which means that the ionized Mn^{+3} has 4d-electrons, which are responsible for its electronic properties. The Jahn-Teller distortion is taking place at Mn^{+3} ion and plays significant role in the Metal-Insulator transition and ferromagnetic to paramagnetic transition. Jahn-Teller (J-T) effect has been described later in this chapter. If we substitute all trivalent rare earth La atoms by a divalent metal such as Ca, we will obtain compound such as $Ca^{+2}Mn^{+4}O_3$ with Mn valence +4. Thus, the Mn ion in the $CaMnO_3$ compound will have 3-d electrons. This compound also has the perovskite structure. Both the perovskites, $LaMnO_3$ and $CaMnO_3$, are AFM insulator with ferromagnetic (FM) n-planes of alternating spin direction [10,11]. For partial substitutions of La system such as $La_{1-x}A_xMnO_3$ ($0<x<1$), Mn ions are mixed valent and average number of d-electrons at the Mn-site is 4-x. An exciting thing is that, although pure La and pure Ca manganites are AFM insulators, the intermediate composition $La_{1-x}A_xMnO_3$ exhibits strong magnetism over a broad range of carrier concentrations and temperatures [7,10].

1.2.2 Zener double-exchange mechanism

It has reported that the lattice distortion brings down T_c by use of hole doping at Ln-site (A-site). Hence T_c can be tuned by changing hole doping concentration and size of ionic radius of divalent cation. Below T_c, the manganites exhibit metal-type conductivity, and ferromagnetism around T_c. These behaviors are explained by Zener's double exchange mechanism [9]. The basic mechanism in this process is, the doping of a d-hole from Mn^{+4} or electron doping from d-shell of Mn^{+3} to Mn^{+4} like Mn^{+3} ($d^4,t_2g^3,e_g^1,S=2$) to Mn^{+4} (d^3, $t_2g^3,s=3/2$) via the oxygen, so that the Mn^{+3} and Mn^{+4} ions change places [9,11].

Mn^{+3} O^{+2} Mn^{+4} ----- Mn^{+4} O^{+2} Mn^{+3}

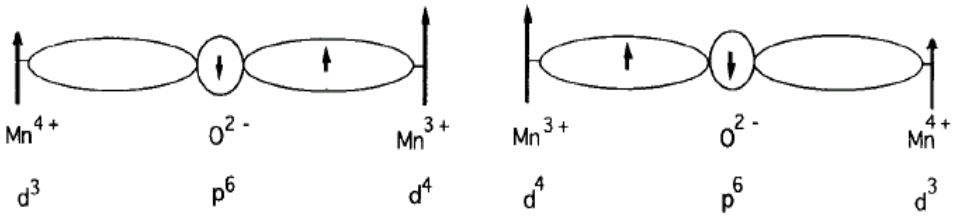

Figure: 1.2 Schematic diagram of Zener Double Exchange mechanism

This creates the transfer of an electron from the Mn^{+3} site to the Central Oxide ion and simultaneously the transfer of an electron from the oxide ion to the Mn^{+4} site. Such a transfer is referred to as double-exchange (DE) [7].

1.2.3 Various mechanisms and properties of manganite perovskites

(a) Jahn-Teller (JT) effect

The rare-earth manganites such as $LaMnO_3$, $PrMnO_3$ and $NdMnO_3$, without hole doping are insulators at all temperatures as a consequence of crystal field at the cation sites in the perovskite structure. In the ideal structure, both A and B sites have cubic point symmetry m 3 m [11]. However, in the real distorted structure, the point symmetry is much lower. These oxides undergo an antiferromagnetic (AFM) transition with $T_N \sim 150$ K. The AFM ordering is of A-Type [7,10]. The Jahn-Teller distortion around Mn^{+3} ions is related to the insulating nature of the compounds and anisotropic magnetic interaction in the structure.

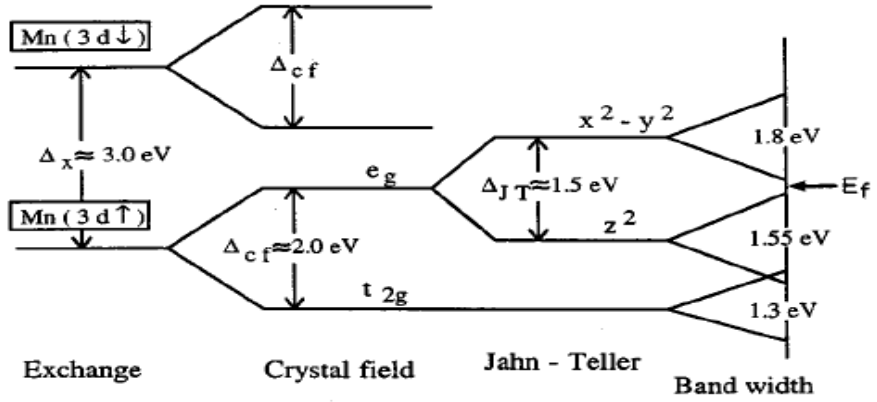

Figure: 1.3 Schematic diagram of band structure of J-T distortion

The structure plays a crucial role in determining the electric transport and magnetic transport properties of these oxides. Because when these parent systems are partly substituted by divalent ions at Ln site they became hole-doped. The Mn^{+4} content increase resulting into decreasing (JT) distortion.

Figure 1.3 shows band diagram of $LaMnO_3$, shows (JT) distortion splits the conduction band and makes the material insulating.

In the energy level diagram for $LaMnO_3$, the values of E_{ex}, E_{cf} and E_{JT} from density functional calculation are around 1.5 – 2 eV and Fermi energy level lies between JT split orbitals. [12,13]. The hole doping reduces JT distortion and makes the material metallic for hole doping ≥ 0.18 [14]. The perovskite structure has an orthorhombic distortion ($b>a>c/\sqrt{2}$) and unit cell consisting of 4-formula units can be mapped into Pbnm or Pnma Symmetry.

(b) Tolerance factor

It has been clearly shown experimentally that for a fixed hole concentration, the properties of manganites strongly depends on a geometrical quantity known as "tolerance factor" [14,15], defined by $t=d_A\text{-}o/(\sqrt{2}d_{Mn}\text{-}o)$ here A-0 is the distance between A site, where the trivalent or divalent non-Mn ions are located, to the nearest oxygen. A ion is at the center of a cube with Mn in the vertices and O in between the Mn ions. d_{Mn}-o is the Mn-O shortest distance. Since for an undistorted cube with a straight Mn-O-Mn link, $d_{A\text{-}o} = \sqrt{2}$ and $d_{Mn\text{-}o}=1$ in units of the Mn-O distance, the t=1 for the perfect system. However, sometimes the A ions are too small to fill the space in the cube centers and for this reason the oxygen tend to move toward the center, reducing $d_{A\text{-}O}$. In general $d_{Mn\text{-}O}$ also changes at the same time. For this reason, the tolerance factor becomes less than unity t<1, [7, 10] and Mn-O-Mn angle θ becomes smaller than 180°. The hopping amplitude for carriers to move from Mn to Mn naturally decreases as θ < 180°. As the tolerance factor decrease, the charge localization increases due to the reduction in the mobility of the carriers. If the tolerance factor is reduced (t<1) then Mn-Mn distance is also reduced. Therefore, it would be expected that having closer Mn-ions result into an increase the electron hopping between them.

A detailed study on different $Ln_{0.7}A_{0.3}MnO_3$ compounds for a variety of Ln and A ions for the dependence of Tc on tolerance factor (t) shows the presence of three dominant regimes (1) a paramagnetic insulator at high-temperature, (2) a low temperature

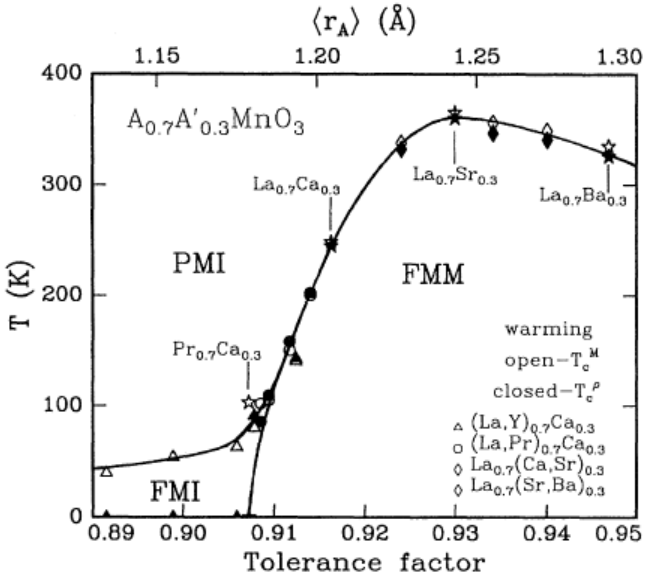

Figure: 1.4 Variation of T_c with tolerance factor (*t*) and average cation radius $<r_A>$

ferromagnetic metal at large tolerance factor, and (3) low –temperature charge-ordered ferromagnetic insulator at small tolerance factor fig. 1.4 [16]. The properties of doped manganites are highly dependent on the tolerance factor (*t*).

(c) Electron-Lattice coupling

The structural and electronic properties of the perovskite crystal clearly have an important effect on Curie temperature and magnetoresistance. However, interaction between the charge carriers and vibrations of the crystal lattice say "phonons" also play a crucial and fundamental role in changing the resistance as the temperature falls towards the Curie temperature, of particular importance are the vibrations of lighter oxygen ions, which push electron towards vacant states in the manganese ion. This strengthens the Jahn-Teller effect and induces a local distortion of the lattice. Such a distortion is known as a "polaron" and leads to self-trapping of the (it can be a source of the high resistivity) charge carriers above the Curie temperature. Below the Curie temperature the self-trapping disappears because the bandwidth broadens and the electrons are much more

mobile [15]. CMR effect is observed over a wide range of compositions of $La_{1-x}Ca_xMnO_3$(x<0.5), but the when x~0.2, a local structural distortion occurs from the strong electron-lattice polarons which arises from the strong electron-lattice coupling [7,11]. But the significant changes in the local structure in the x~0.3 composition in the 80-300k range are observed which are attributed to the formation of small polarons due to the John-Teller distortion when T>Tc, [17,18] these studies have shown that small polarons delocalized as the magnetization increases in the manganite which induces the I-M transition.

(d) Insulator - Metal (I-M) and paramagnetic – ferromagnetic (PM-FM) transition

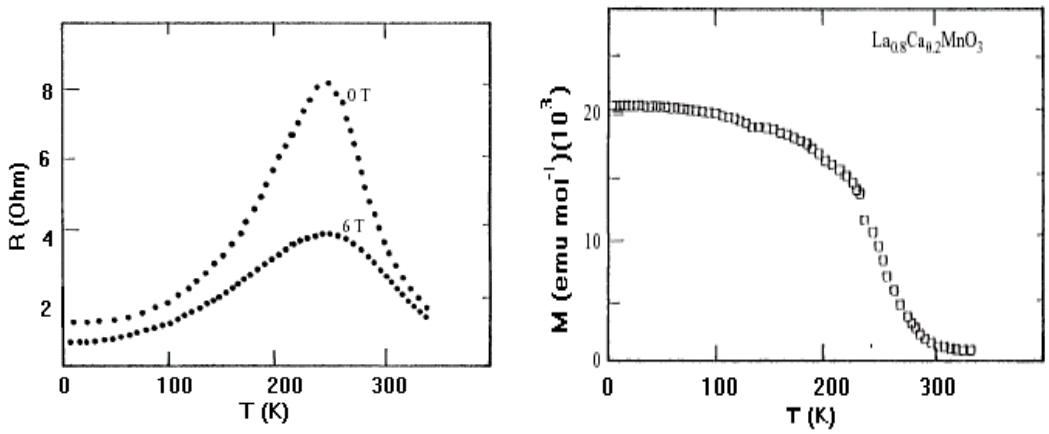

Figure:1.5(a) & (b) Metal-insulator transition and Paramagnetic-Ferromagnetic transition, in $La_{1-x}Ca_xMnO_3$.

In addition to various phenomenon described above, (M-I) the metal-insulator and paramagnetic to ferromagnetic transition (PM-FM) take place in $LaMnO_3$ perovskite with an orthorhombic structure (b>a>c1/2, Pbnm) with small proportion of Mn^{+4} (< 5%), becoming antiferromagnetically ordered below T_N ~150 K. In $LaMnO_3$ if La^{+3} is progressively substituted by a divalent cation, the formula becomes $Ln_{1-x}A_xMnO_3$ (Ln=La,Nd,Sm,Pr and A=Ca,Sr,Ba, Pb..). Systematic investigations show that an empirical relationship exists between electrical conductivity and magnetism [9]. With increase in x (Mn^{+4} Content), the manganites become ferromagnetic, with well-defined curie temperatures T_c and around T_c, it exhibits metal-like conductivity as shown in fig. 1.5(a) & 1.5(b). The simultaneous observations of I-M and PM-FM transitions are

explained by the Zener double exchange mechanism. A metal is in the ferromagnetic phase, whose resistivity decreases as the magnetization increases below Tc. So the ferromagnetism is always coupled with metallic phase in the system.

(e) Role of ionic radii at A-site

The ionic radii at A-site play an important role in modifying the electrical and magnetic transport properties of manganite.

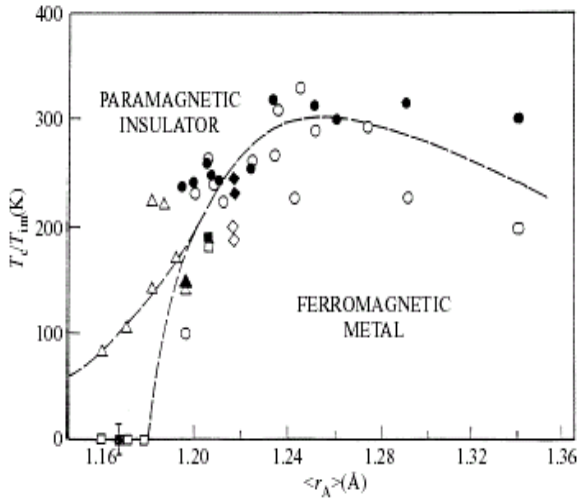

Figure: 1.6 Ionic radius at A-site $<r_A>$ vs. T_c/T_{im}

As divalent cation is introduced at A-site, the ionic radii becomes mixture of Ln= rare earth trivalent and A= divalent cation which is named as average A-site ionic radius ($<r_A>$). The modification in the tolerance factor 't' alters the transition temperature and desired transport properties of manganites can be achieved. The fig. 1.6 shows the variation in transition temperature with average ionic radius $<r_A>$ of A-site [19,20]. The transition temperature is highest when $<r_A>$ ~1.23Å which corresponds to a tolerance factor of 0.93. It may be also noticed that increase in $<r_A>$ the e_g band with increases and MR% decreases [21, 22].

(f) Charge and Orbital Ordering

The charge order, also known as Wigner Crystallization, is driven by inter atomic coulomb interaction. The mobile d electrons can be localized on certain manganese ions to form a regular lattice for particular occupancies of the d band, provided that inter

electronic coulomb interaction is comparable with the conduction-electron bandwidth W [23]. The effect is accentuated by small displacements of the oxygen atoms to accommodate the ordered cation lattice. Charge ordering most likely occurs when the temperature is low and x is a rational fraction especially x= 1/8 or 3/4. The extra fourth d electron may then be delocalized on alternate manganese site in a plane, as shown in fig. 1.7 (a). The carriers in mixed-valent manganites may be strongly coupled to local lattice distortion [24]. Orbital ordering can occur at certain carrier density when the d electrons occupy an asymmetric orbital as shown in fig. 1.7 (b). The driving source is partly direct electrostatic repulsion of the charge. Adjacent octahedra stabilize the effect. Figure 1.7(c) displays the combined effect of charge and orbital order in mixed valent manganites when the doping concentration is x=1/2 .

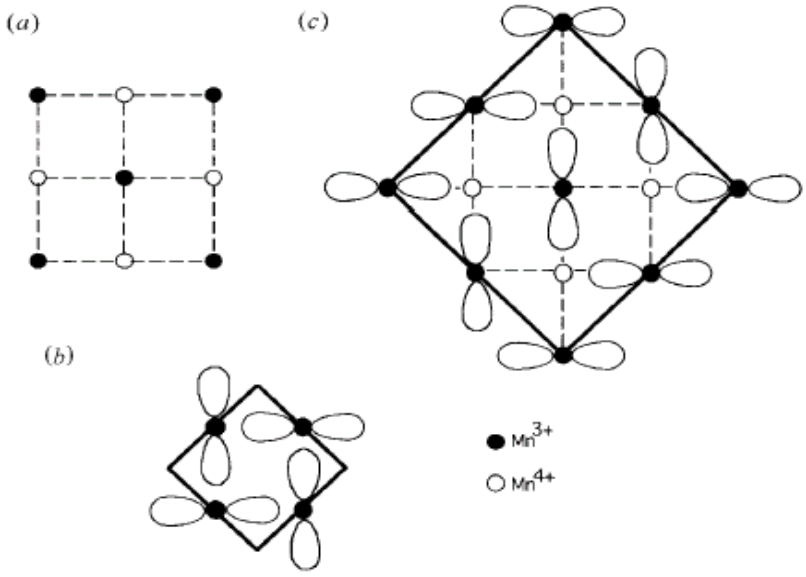

Figure 1.7 (a) charge ordering **(b)** orbital ordering **(c)** charge and orbital ordering.

1.2.4 Phase diagrams of LCMO and LSMO

(a) Phase diagram of $La_{1-x}Ca_xMnO_3$ manganite

The compound $La_{1-x}Ca_xMnO_3$ exhibits a variety of phases when the carrier concentration (x) and temperature (T) are varied [25-27]. These phases are characterized by different magnetic and transport properties. Figure 1.8 shows the phase diagram of

$La_{1-x}Ca_xMnO_3$ manganites. At x=0.0, $LaMnO_3$ is an insulator. The material exhibits a magnetic transition from paramagnetic to AFM insulating state at T_N = 141 K. For 0.0 < x < 0.2, the material remains in an insulating state, but the magnetic order changes in a complicated way showing the crossover from canted antiferromagnetism (CAF) to ferromagnetic insulator (FI). At x ~ 0.2, the ground state becomes the FM metal.

In the region of 0.2 < x < 0.5, the compound is FM metal at $T<T_c$, where T_c is the Curie temperature shown by the solid line. For x>0.5 the material first undergoes paramagnetic-to-charge ordered (CO) insulator transition when temperature is lowered, end the structure becomes AFM and charge-ordered with further cooling. Finally, at x ~1.0

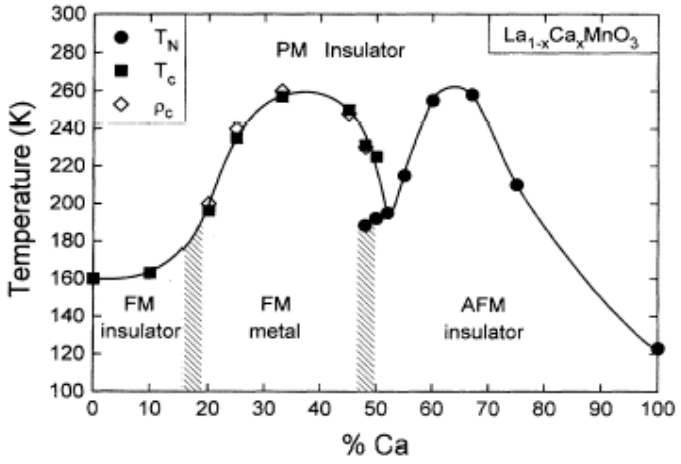

Figure: 1.8 Phase diagram of $La_{1-x}Ca_xMnO_3$ manganite

the compound becomes a pure $CaMnO_3$, which exhibits an insulating behavior with the AFM ordering at $T < T_N$ = 131 K with a different type of AFM ordering than in the pure La-manganite [14].

(b) Phase diagram $La_{1-x}Sr_xMnO_3$ manganite

The phase diagram and low-temperature behavior of $La_{1-x}Sr_xMnO_3$ (LSMO) shows that there are some differences in its phase diagram than that of LCMO (Fig. 1.9) mainly due to the size difference between Ca and Sr ions, Sr being quite larger in size as compared to Ca [28, 29]. As shown in fig. 1.9, there are three distinct ground states, the spin-canted insulator, the FM insulator and the FM metal. At high temperatures there appears to be two distinct phases, paramagnetic insulator (PI) and paramagnetic metal

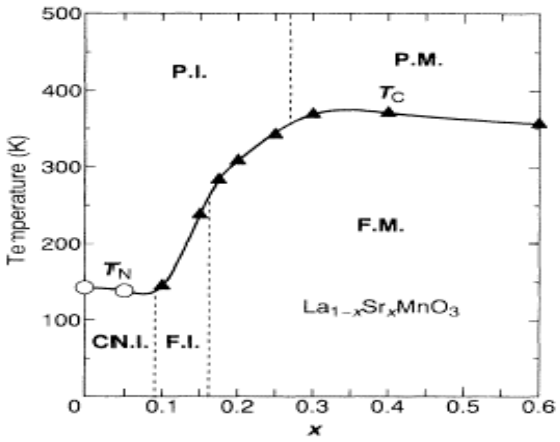

Figure: 1.9 Phase diagram of $La_{1-x}Sr_xMnO_3$

(PM). The vertical lines demarcating these phases are determined by ρ(T) between semiconducting (insulating) and metallic behaviour, as shown in figure. The insulator-metal transition at low temperature is an orthorhombic ($x \leq 0.175$) to rhombohedral ($x > 0.175$) transition. An important aspect of Sr Substitution is, the inability to obtain single-phase material for $x>0.6$. Within the range of phase stability ($x < 0.6$), however, there is a remarkably large variation in transport from good metal for $x > 0.3$ to insulator for $x \leq 0.15$. It should be noted that, the crossover from metallic to insulating behaviour occurs in a very narrow concentration region. At the low end of the substitution a remarkable field-induced structural transition is observed.

1.2.5 Literature survey

During the last decade, majority of the studies are devoted to understand the origin, properties and applications of pure and doped manganites. The parent system $LaMnO_3$ is cation deficient compound [30,31]. The defective chemistry creates wide range of doping possibilities on both the cationic sites. It has been reported that, the doping studies in manganites are not only important from the application point of view but helps to understand rich physics underlying them.

The studies of doping phenomena in manganites can be divided in to the following general types -

a. Self doping

(1) A-site deficient: $Ln_{1-\delta}MnO_3$

(2) B-site deficient : $LnMn_{1-\delta}O_3$

(3) A-site, B-site deficient : $Ln_{1-\delta}Mn_{1-\delta}O_3$

b. Divalent substitutions at A-site

$Ln_{1-x}A_xMnO_3$: A- divalent cation

c. Transition metal substitutions at B-site

$Ln_{1-x}A_xMn_{1-y}T_yMnO_3$: A-divalent cation, T – transition metal ion

a. Self doped Systems

A-site and B-site deficient systems are referred as self doped systems or cation deficient systems. The $La_{1-\delta}MnO_3$ ($0.0 \leq \delta \leq 0.1$) compositions are all ferromagnetic and show insulator metal (I-M) transition, with the resistivity decreasing with increasing δ. $LaMn_{1-\delta}O_3$ compositions show ferromagnetism and the I-M transition only up to $\delta = 0.005$, having the resistivity increase with δ [32]. The investigations on $La_{0.90}MnO_3$ compound shows CMR properties near room temperature. This phase exhibit ferromagnetic transition at $T_C \sim 230 - 260$ K depending on hole density (0.05-0.06). This phase can be indexed in rhombohedral structure but powder X-ray and electron diffractions studies show that, it exhibits monoclinic symmetry [33].

Several studies on the self-doped systems indicate that, there exist four forms of $La_{1-\delta}MnO_3$ system, namely, two orthorhombic, one rhombohedral and one cubic form which depends on the oxygen stoichiometry [34-36]. J. Topfer et al showed that, $LaMnO_3$ system has orthorhombic phase stable over $0.0 \leq \delta \leq 0.06$ and rhombohedral phase, which is stable in the range $0.10 \leq \delta \leq 0.18$ [37, 38].

b. Divalent substitution at A-site

The Mn based mixed oxide based compounds with divalent substitutions at crystallographically distinct A site with stoichiometric formula ABO_3 were first studied by Jonker and Van Santen [1], who coined the name manganites to this systems. Later on Wollan and Koehler [39], investigated $La_{1-x}Ca_xMnO_3$ compounds using neutron scattering. In their study, the antiferomagnetic (AF) and ferromagnetic (FM) phases where characterized and reported to have C- and E- type magnetic unit cells in the structure with $x = 0.5$.

The renewed surge of interest in manganites, in the 1990, started with the experimental observation of large magnetoresistance (MR) effect in $Nd_{0.5}Pb_{0.5}MnO_3$ [40] and in $La_{2/3}Ba_{1/3}MnO_3$ [5]. The MR effect in the thin films was found to be as high as 60 %. The discovery of the so called "Colossal Magnetoresistance" (CMR) effect in the thin films of $La_{0.67}Ca_{0.33}MnO_x$ [41], showed that, the MR effect was three orders of magnitude larger than the typical "giant" MR of superlattice films observed. The report of Xiong et al [42] on the studies of $Nd_{0.7}Sr_{0.3}MnO_\delta$ thin films showed that, the MR effect was as high as 10^6 %, a truly "Colossal". Triggered by such numbers, several experimental and theoretical studies were carried out on these compounds with $x = 0.3$ doping due to its large T_C. However, more recently attention has shifted towards other doping concentrations such as $x < 0.2$ or $x > 0.5$ where interesting feature of competition between various states and phase in manganites have been reported.

Ca and Sr doping

Most of the recent work has been focused on Ca^{+2} and Sr^{+2} substitutions at A-site since the CMR behavior in these compounds varies as a function of divalent cation size and concentration, which is reflected in the difference between the phase diagrams of $La_{1-x}Ca_xMnO_3$ (LCMO) and $La_{1-x}Sr_xMnO_3$ (LSMO) systems [43-45]. At high temperatures, in LCMO, only paramagnetic insulator (PI) phase has been reported while, in LSMO, two distinct phases (PI) and paramagnetic metal (PM) have been observed. It has been also reported that substitution at Ln-site modifies the phase behavior through size effect in $(Nd_{1-y}Sm_y)_{0.5}Sr_{0.5}MnO_3$ [46,47]. This compound exhibits instability at FM ground state. Similar behavior has also been observed in $Pr_{0.5}Sr_{0.5}MnO_3$ and $Pr_{0.7}(Sr\ Ca)_{0.3}MnO_{3-\delta}$

systems [48-50]. The detailed study of low bandwidth $Pr_{1-x}Ca_xMnO_3$ (PCMO) and other properties of the system have been explained by several groups [51-54].

Ba doping

The literature survey reveals that there exists less amount of work related to Ba^{+2} substitution at A-site, probably due to larger size of Ba^{+2} as compared to Sr^{+2}. Thin films of $La_{0.67}Ba_{0.33}MnO_3$ were studied by [5]. Von Helmolt et al [55] also studied the series $La_{(2-x)/3}Ba_{(1+x)/3}Mn_{1-x}Cu_xO_z$ having the end members (x = 0.0 and 1.0) as ferromagnetic $La_{2/3}Ba_{1\backslash 3}MnO_z$ and $La_{1/3}Ba_{2\backslash 3}CuO_z$ superconductor. In the Mn rich region, the perovskite phase is found for x < 0.4. Ju et al [56] studied $La_{0.67}Ba_{0.33}MnO_z$ as a function of oxygen content z. It was found that on lowering z from 2.99 to 2.85, ρ increased by almost six orders of magnitude uniformly over the temperature range 0 – 350 K.

Bi- based Compounds

The series of compounds with $Bi_{1-x}Ca_xMnO_z$ stoichiometry have been studied by several groups [57,58]. Due to stable trivalent state of Bismuth, one would expect similar properties as that of La- based compounds. Interestingly, however, no evidence for metallicity has been found in polycrystalline samples for 0.3 < x < 0.9 for H = 0. The absence of metallic behavior has been ascribed to the high polarizability of Bi^{+3} ion. Bao et al [59], reported neutron diffraction on single crystal with x = 0.82 and showed that, both, Charge Order (CO) and antiferomagnetic (AF) transition occurs at ~ 7 T field. Bismuth doping also has been studied in (Sm, Sr) MnO_3 [60].

Electron doping

The electronic and magnetic properties of perovskite manganites depend on several correlated factors, inducing mixed valence of Mn in to Mn^{+3}/Mn^{+4}.In order to create valence fluctuations at Mn site in to Mn^{+3}/Mn^{+2}, several groups have studied the substitution of the tetravalent elements at A-site. Recently, number of reports have been published which describes the studies on the magnetic, electrical and structural behavior of the samples with nominal composition $La_{1-x}Ce_xMnO_3$ [61-66].

c. B-site doping

In order to obtain more information of Zener Double Exchange (ZDE) mechanism, which is responsible for the FM and I-M transition in CMR manganites, large amount of work has been carried out on studying the effect of doping at B-site in these materials [67-73]. It is reported that, magnetotransport properties of these materials are sensitive to the doping at Mn site. Several groups have studied substitution of bivalent, trivalent or tetravalent elements such as Al, Ga, In, Ti, Fe, Sn, Mg,Ga, Co, Ni…doped at Mn site. Xin chem. et al reports the doping at B-site in $La_{0.67}Ba_{0.33}Mn_{0.90}B_{0\cdot10}O_3$ (B = Ga, Ni, Fe) system. It is seen that there is decrease in ferromagnetism and metallic conductivity because of the destruction of the double-exchange interaction. But the MR values are higher in the samples [73,74]. It is also reported that, the doping of Cr and Ru at Mn site in PCMO system results into high magnetization values and I-M transition which is not limited for a narrow composition range in $La_{0.6}Ca_{0.4}Mn_{1-y}(Cr/Ru)_yO_3$ system [67]. S.B.Ogale et al [75] showed that, partial replacement of Mn by Fe in $La_{0.75}Ca_{0.25}Mn_{1-x}Fe_xO_3$ results into small changes in chemical composition, which leads to dramatic changes in transport properties and an instability of the low-temperature ferromagnetic metallic phase.

1.3 Applications

The CMR materials have good potential for device applications. Several groups have attempted to explore the transport properties, specially half metallicity and transition from insulating to metallic region in the CMR materials for their applications in various devices [76-78]. In brief, the general applications of the CMR materials have been discussed as follows.

1.3.1 CMR materials as Sensor & devices

(a) Magnetic Sensor

Using the CMR effect in thin films, numbers of efforts have been made to fabricate magnetic sensors. For magnetic field sensing applications, low field response at or above the room temperature, the researchers have used the defects or grain boundary effects in microstructure of the manganites [77,78]. The low field sensitivity is due to spin polarized

tunneling between two grains [79-81]. The idea of development of heterostructure is more prominent, which show low field sensitivity at room temperature [82].

The industrial requirements of magnetic sensors using CMR materials should follow the following properties.

1) Operating at or above room temperature.
2) At least 20% response at a field of ≤ 100 Oe
3) Temperature independent MR value over 300 ± 50 K.
4) Acceptable noise values.
5) The dimensions of film approaching 1000°A or less than that.

(b) Microwave CMR Sensor

At microwave frequencies, significant CMR effect has been observed as compared to at low frequency [83]. For the microwave cavity in the anti resonant mode, a very large CMR effect is seen ~ 50 % at very low field which suggests the possible microwave devices.

(c) Spin valve devices.

The spin valve device consists of two ferromagnetic electrodes separated by a nonmagnetic conducting layer [84]. In general, the lower electrode has a large coercive field than the upper electrode. The entire device structure consists of epitaxial multilayer of CMR ferromagnetic electrodes separated by an epitaxial layer of conducting materials. However, devices made using this concept have large series resistance, which can not be explained on the basis of the resistivity of individual layers and this reduces the observed MR. An alternate approach is the trilayer spin tunneling device, where the intermediate layer is an epitaxial insulator. This type of device shows large low-field MR, about factor of two to five, in a field around 100 Oe at 4.2 K.

(d) Electric field effect devices

The field effect transistor (FET) device structure consists of epitaxial multilayer of CMR ferromagnetic layers at the bottom and dielectric layers on the top. This device

structure shows some interesting characteristics depending on the dielectric layer on top as to whether it is a para-electric layer such as STO, or a ferroelectric PZT [85].

(e) Bolometric Sensor

Due to the large temperature co-efficient of resistance (TCR) in CMR materials, their application as bolometer device is possible [86,87]. The CMR materials exhibits I-M transition at Tc and sharp drop of the resistance at transition temperature gives large TCR. The merit of the bolometric device is the TCR and noise volume. The commercial bolometer is based on VO_x, having TCR values around 2.5 to 4%. As compared to VO_x, the TCR values increases from 8 to 18 % in CMR materials. Ravi bathe et al showed 23% TCR in LCMO thin film with silver ion implantation [88].

(f) Spin Polarized injection devices

At low temperatures <100 K, CMR materials show some interesting properties and is found to be advantageous to integrate them with HTSC. A heterostructure consisting of HTSC/CMR has been used for magnetic flux focused devices [89]. The Meissner effect of the superconductor can be used as magnetic lens to enhance the flux coupling to a CMR detector thereby enhancing its sensitivity. And spin polarized electrons are injected from CMR layer into the superconducting channel [90,91].

Motivation for the present work

The doping at A - site can be done more flexibly in large range of concentrations. The isovalent light rare earth substitutional studies have been done by various researchers to study the effect of cation size mismatch and average A site cation radius effect on the electronic and magnetic transitions. Only some light rare earths like La, Pr, Nd and Sm based manganite systems show the CMR properties whereas heavy rare earth like Gd, Ho, Dy etc. due to smaller ionic radii results in the buckling of Mn – O bonds significantly such that e_g band itinerant electron gets localized permanently to their parent atoms.

Depending upon the transition temperatures and related CMR effect, the manganite systems have been classified as low bandwidth, intermediate bandwidth and large bandwidth manganite systems. The system such as $Pr_{1-x}Ca_xMnO_3$ in which ferromagnetic metallic state is not stabilized and a ferromagnetic insulating state exists in the range

between x = 0.15 – 0.4 is classified as ***low bandwidth manganite system***. This system represents a stable charge-ordered state in a broad density region between x = 0.30 – 0.75. Such manganites exhibit I-M transition when subjected to magnetic field, pressure and when exposed to X-rays. Since there is large buckling at Mn-O bond due to smaller size of Pr, the application of even weaker magnetic field results in significant amount of CMR effect. The manganite like $La_{0.7}Sr_{0.3}MnO_3$ shows the transition temperature well above the room temperature around 370K and labeled as ***large bandwidth manganite system***. It is believed that, in this compound the hopping amplitude for electrons in e_g band is larger than in other manganites as a consequence of the sizes of the ions involved in chemical compositions. Large bandwidth systems have spins almost parallel at the Mn-O couplings, so the application of magnetic field does not produce any significant change in resistivity in already magnetically ordered region. The drawback of large bandwidth system is that, the large transition temperature is coupled to small CMR effect that has restricted these materials from application point of view. The third type of manganite system that has characteristics of both, the low and large bandwidth systems and in which the research is being carried out by a sizeable fraction of researchers is called as ***intermediate bandwidth manganite system***. $La_{1-x}Ca_xMnO_3$ is a typical example of such a system. This compound represents the presence of robust ferromagnetic metallic state. It has also features that represent deviation from double-exchange behavior, including the existence of charge ordered and orbital ordered state. Recently the work is also being focused on intermediate to low bandwidth materials since these are the ones that exhibit the largest CMR effect, which is associated with the presence of charge ordering tendencies.

Keeping in mind the role of average A-site cation radius ($<r_A>$) and the amount of divalent cation doping in modifying the structural, transport and magnetic properties of various manganite systems, we have made an attempt to study the simultaneous effect of $<r_A>$ and carrier density in an intermediate bandwidth system $La_{1-2x}Pr_xCa_xMnO_3$ ($0 \leq x \leq 0.3$). Also, an optimally doped systems $(La_{0.5}Pr_{0.2})Ca_{0.3}MnO_3$ has been studied and found to exhibit properties of a nearly low-bandwidth systems. We have separately studied the effect of modification in bandwidth of this system when Ca^{2+} is replaced by with larger cations Sr^{2+} and Ba^{2+}. This results in the interesting properties arising as a result of increase in $<r_A>$ and size-disorder at A-site. Particularly, the Ba^{2+} substitution induces a

local structural distortion and hence, results in phase-segregation. The effect of phase-segregation in inducing the transport and magnetic anomalies has been discussed in subsequent chapters.

In the course of present work, along with the hole-doped manganite systems, efforts have been made to investigate the possibility of obtaining related effects in electron-doped manganites. The compounds like $La_{0.7}Ce_{0.3}MnO_3$ have been found to exhibit several interesting transport and magnetic properties. In hole-doped systems when average charge on A site is reduced, the manganese ions go in a mixture of Mn^{3+}/Mn^{4+} valence states. On the other hand, in electron-doped systems $<r_A>$ is increased by aliovalent cation doping at rare earth site. The increased charge on A-site will be able to drive the manganese ions in a mixture of Mn^{3+}/Mn^{2+} states. Mn^{2+} valence state of manganese, like Mn^{4+} valence state, is a non Jahn–Teller ion. The Zener Double Exchange should occur between two adjacent Mn^{3+} and Mn^{2+} ions in the same way as it occurs between Mn^{3+} and Mn^{4+} ions. One would, therefore, expect electron-doped manganites to exhibit ferromagnetic-metallic behavior coupled with a large magnetoresistance.

The chapter-wise detail of all the subsequent chapters is given below

Chapter 1 describes the phenomenon of magnetoresistance observed in different types of materials with a detailed description about various mechanisms, properties and phases present in the perovskite type manganite materials exhibiting large magnetoresistance.

Chapter 2 of the thesis deals with the various experimental techniques and methods such as X-ray diffraction (XRD), scanning electron microscopy (SEM), d.c. four-probe method for resistivity and magnetoresistance measurements and d.c. and a.c. magnetization measurements. Their need and importance as a characterization tool has also been discussed.

Chapter 3 is based on our investigations of effect of simultaneous increase in $<r_A>$ and carrier density in Pr and Ca substituted antiferromagnetic insulating compound $LaMnO_3$. For this purpose, we have studied the structural, transport, magnetic and magnetotransport properties of $La_{1-2x}Pr_xCa_xMnO_3$ ($0 \leq x \leq 0.3$) manganite system.

Chapter 4 deals with effect of bandwidth modification of $La_{0.5}Pr_{0.2}Ca_{0.3}MnO_3$ compound by substitution of larger size cations Sr^{2+} and Ba^{2+} for smaller cation Ca^{2+}. In this chapter, a detailed investigation of structural, transport, magnetic and magnetotransport properties of $(La_{0.5}Pr_{0.2})(Ca_{0.3-x}A_x)MnO_3$ ($A=Sr^{2+}$ and Ba^{2+}) ($0 \leq x \leq 0.3$) has been made.

Chapter 5 is devoted to the study of the possible role of electron doping at A site due to higher valence cations like Ce^{4+}, Th^{4+} and Mo^{6+} etc. For this purpose we have studied the electron-doped system $Re_{1-x}A_xMnO_3$; A = Th and Mo for structural, transport, magnetic and magnetotransport properties.

References

1. G.H. Jonker and J.H. Van santen, Physica XVI, (3 Mart 1950)
2. Edwin Hall (1879)
3. M.N. Baibich, J.M. Broto, A. Fert, F. Van Dau. Nguyen, F. Petroff, P. Etienme, G. Creuzet, A. Friederich, J. Chazeless Phy. Rev. Lett. **61**, 2472 (1988)
4. R.M. Levy, J. Solid State Phys. **47**, 367 (1994)
5. R. Von Helmolt, J. Wecker, B. Holzapfel, L. Schultz and K. Samwer et al, Phys. Rev. Lett. **71**, 2331 (1993)
6. A. Urushibara et al, Phys. Rev. B **51**, 14103 (1995)
7. Colossol Magnetoresistance, Charge Ordering and related properties of Manganese Oxides Ed. By. C.N.R. Rao, B. Raveau. World Scientific Publishing Co. Pte. Ltd. (1998)
8. R. Mahesh, R. Mahendiran, A. K. Raychaudhuri and C.N.R. Rao, J. Solid State Chem. 114, 297 (1995)
9. C. Zener, Phys. Rev. **82**, 403 (1951)
10. J.B. Goodenough, Rep. Prog. Phys. **67**, 1915-1993 (2004)
11. J.M.D. Coey, M. Viret., Advances in Physics **48**, 2, 167 (1999)
12. S. Satpathy, Z.S. Popovic, F.R. Vukajlovic, J. Appl. Phys. **79**, 4555 (1996)
13. I. Solovyev, N. Hamada, K. Terakura, Phys. Rev. Lett. **76**, 4825 (1996)
14. A. P. Remirez, J. Phys. Conds. Matter **9**, 8171 (1997)
15. E. Dagotto, T. Hotta, A. Moreo, Physics Report **344**, 1-153 (2001)
16. H.Y. Hwang, S.W. Cheong, P.G. Radaelli, M. Marezio and B. Batlogg, Phys. Rev. Lett. **75**, 914 (1995)
17. S.J.L. Billinge, R.G. Difrancesco, G.H. Kwei, J.J. Neumeier and J.D. Thompson, Phys. Rev. Lett. **77**, 715 (1996)

18. T. A. Tyson, J. Mustere de leon, S.D. Conradson, A.R. Bishop, J.J. Neumeier, H. Roder and Junzang, Phys. Rev. B. **53**, 13985 (1996)

19. B. Reveau, J. Solid State Chem. **117**, 424 (1995)

20. J. Fontcuberta, B. Martinez, A. Setfar, S. Pinol, J.L. Garcia-Munoz and X. Ofraders, Phys. Rev. Lett. 76, 1122 (1996)

21. M.R. Ibarra, P.A. Algarabel, C. Marquina, J. Blasco and J. Garcia, Phys. Rev. Lett.**75**, 3541 (1995)

22. R. Mahendiran, R. Mahesh, A.K. Raychaudhury, C. N. R. Rao, Phys. Rev. B. **53**, 12160 (1996)

23. J. R. Cullen and E. Callan, Phys. Rev. **7**, 397 (1973)

24. J. Kanamori, J. Phys. Chem. Solids. **10**, 87 (1959)

25. P. Schiffer, A. P. Ramirez, W. Bao and S.W. Cheong, Phys. Rev. Lett. **75**, 3336 (1995)

26. G. Q. Gong, C. Canedy, G. Xiao, J.Z. Sun, A. Gupta and Gallagher., J. Appl. Phys. Lett. **67**, 1783 (1995)

27. R. Mahesh, R. Mahendiran, A. K. Raychaudhury and C. N. R. Rao, Appl. Phys. Lett. **68**, 2291 (1996)

28. Y. Tokura, A. Urushibara, Y. Moritomo, T. Arima, A. Asimitsu, G. Kido and N. Furukawa., J. Phys. Soc. Japan **63**, 3931 (1994)

29. R. Mahendiran, A. K. Raychaudhury, A. Chainani, D. D. Sharma and S.B. Roy. Appl. Phys. Lett. **66**, 233 (1995)

30. C. N. R. Rao, A. K. Cheetham and R. Mahesh, Chem. Mater. **8**, 2421 (1996)

31. C. N. R. Rao, Phil. Trans. R. Soc. Lond. A, **356**, 23 (1998)

32. Anthony Arulraj, R. Mahesh, G. N. Subbanna, R. Mahendiran, A. K. Raychaudhuri and C. N. R. Rao., J. Solid State Chem. **127**, 87, (1996)

33. A. Maignan, C. Michel, M. Hervieu and B. Raveau, J. Solid State Commun. **101**, 4(1997)

34. R. Mahendiran, S. K Tiwary, A. K. Raychaudhuri , T. V. Ramkrishnan, R. Mahesh, N. Rangavittal and C. N. R. Rao, Phys. Rev., B. **53**, 3348, (1996)

35. B. C. Hauback, H. Fjellvag and N. Sakai, J. Solid State Chem.**124**, (1996)

36. M. Hervieu, R. Mahesh, N. Rangavittal, C. N. R. Rao, Eur. J. Solid State Inorg. Chem. **32**, 79 (1995)

37. J. Topfer and J.B. Goodenough, J. Solid State Chem. **130**, 117, (1997)

38. M. Verelst, N. Rangavittal, C. N. R. Rao and A. Rousset, J. Solid State Chem. **104**, 74, (1993)

39. E. O. Wollan and W. C. Koehler, Phys. Rev. **100**, 545 (1955)

40. R. M. Kusters. J. Singleton, D. A. Keen, R. McGreevy, W. Hayes, Physica B **155**, 362 (1989)

41. S. Jin, T. H. Tiefel, M. McCormack, R. A. Fastnacht, R. Ramesh, L. H. Chen, Science. **264**, 413 (1994)

42. Xiong G. C., Li Q., Ju H., L. Mao, S. N. Senapati, Xi X. X., Greene R. L. and T. Venkatesan, Appl. Phys. Lett. **66,**1427 (1995)

43. A. Urushibara, Y. Moritomo. T. Arima, A. Asamitsu, G. Kido. And Y. Tokura Phys. Rev B **51**, 14103 (1995)

44. A. Asamitsu, Y. Moritomo, Y. Tomioka, T. Arima, and Y. Tokura, Nature **373**, 407 (1995)

45. H. Kawahara, Y. Tomioka, Q. Asamitsu, Y. Moritomo, and Y. Tokura, Science, **270**, 961 (1995)

46. Y. Tomioka, A. Asamitsu, Y. Moritomo, H. Kawahara and Y. Tokuree, Phys. Lett. **74**, 5108 (1995)

47. Y. Tokura, H. Kuwarha, Y. Moritomo, Y. Tomioka and A. Asamitsu, Phys. Rev. Lett. **76**, 3184 (1996)

48. V. Caignaert, A. Maignan and B. Raveau, Solid State Conmun. **95**, 357 (1995)

49. B. Raveau, A. Maignan and V. Caignaert, J. Solid State Chem. **117**, 4243 (1996)

50. A. Maignan, Ch Simon, V. Caignaert and B. Raveau, J. Magn. Magn. Mater. **152**, 25 (1996)

51. Y. Tomioka, A. Asamitsu, H. Kuwahara, Y. Moritomo and Y. Tokura, Phys. Rev. **B 53 R**, 1689 (1996)

52. J. Barrart, M. R. Lees, G. Balakrishnan and D. McK. Paul, Appl. Phys. Lett. **68**, 424 (1996)

53. H. Yoshizawa, H. Kawano, V. Tomioka and Y. Tokura, Phys. Rev. B **52**, R13145 (1995)

54. H. Yoshizawa, H. Kawano, Y. Tomioka and Y. Tokura, J. Phys. Soc. Japan **65**, 1043 (1996)

55. R. Von Hewlmolt, L. Haupt, K. Bamer and U. Sondermann, Solid State Commu. **82,** 641 (1992)

56. H. L. Ju, J. Gopalkrishnan, J.L. Peng, Q. Li. Xiong G. C. T. Venkatensan and R. L. Greene, Phys. Rev. B **51** (1995)

57. V. A. Bokov, N. A, Grigoryan and M. F. Bryzhina, Phys. Status Solid. **20**, 745 (1967)

58. H. Chiba, M. Kikuchi, Y. Muraoka, and Y. Syono, Solid State Commun. **99**, 499 (1996)

59. W. Bao, J. D. Axe, C. H. Chen, and S. W, Cheong. Phys. Rev. Lett. **78**, 543 (1997)

60. F. Damay, A. Maignan, M. Hervieu, N. Nguyen and B. Raveau, C. R. Acad. Paris **322**, 573 (1996)

61. S. Das and P Mandal, Indian J. phys. **71**, 231 (1997)

62. S. Das and P. Mandal Z phys.B Condens.Matter **7**, 104 (1997)

63. P. Mandal and S. Das, Phys. Rev. B. 56, 15073 (1997)

64. J. R. Gebhadt, S. Roy and N. S. Ali, J. Appl. Phys. **85**, 5390 (1999)

65. P. Raychaudhuri, S. Mukharji, A. K. Nigam, J. John, U. D. Vaisnav, and R, Pinto, J. Appl. Phys. Lett. **67**, 3494 (1999)

66. J. Philip and T. R. N. Kutty, J. Phys.: Condens. Mater. **11**, 8537 (1999)

67. B. Reveau, C. Maignan, A. Maignan. M. Hervieu and R. Mahendiran, Physica C, 341-348, **711** (2000)

68. A. Maiganan et al. z. Phys. B. **102**, 19 (1997)

69. C Martin et al., J. Mater. Chem. **6**, 209 (1997)

70. F. Damay et al., J. Solid State Chem. **124**, 385 (1996)

71. A. Maignan et. al., Phil Trans, Roy. Soc. Lond. **356**, 1635 (1998)

72. Xin Chen, Zhinong Wang, Jianwang Cai, Baogen Shen, and Wenshan Zhan, Jinsong Chen, J. Appl. Phys. **86**, 8, 4535 (1999)

73. K. H. Ahn, X. W. Wu, K. Liu, and C. L. Chien, Phys. Rev. B. **54**, 21, 15299 (1996)

74. L. Ridhi and P. Gorria, J. Appl. Phys. **81**, 8 (1997)

75. S. B. Ogale, Shreekala, R., Bathe. R., Bathe. R., Date, S. K. Patil, S. I. Hannoyer, B, Petit, F., Marest, G. Phys. Rev. B. **57**, 7841(1998).

76. J. Z. Sun and A. Gupta, Annu. Rev. Mater. Sci. **28**, 45 (1998)

77. T. Venkatesan, M. Rajeswari, Zi-Wen Dong, S.B, Ogale, and R. Ramesh, Phil, Trans, R. Soc. Lond. A. **356**, 1693 (1998)

78. N. D. Mathur, G. Burnell, S.P. Isaac, T.J. Jackson, B.S. Teo, J.L. MacManus-Dricoll, L.F. Cohen, I. E. Evetts, and M.G. Blamire, Nature **387**, 266 (1997)

79. J. Z. Sun, L. Krusin - Elbaum, P. R. Duncombe, A. Gupta, and R. B. Laibowitwitzpal., Phys. Lett. **70**, 1769 (1997)

80. H. Y. Hwang, S. W. Cheong, N.P. Ong and B. Batlog Phys. Rev. Lett. **77**, 2041 (1996)

81. A. Gupta, G. Q. Gong, G. Xiao, P. R. Duncombe, P. Leoeur, P. Trouilloud, Y. Y. Wang, V. P. Dravid, and J. Z. Sun, Phys. Rev. B. **54**, 15629 (1998)

82. *Colossal Magnetoresistive Oxides* Ed. By Y. Tokura, Gordon and Breach Science Publishers (2000)

83. M. Dominguez, S. M. Bhagat, S.E. Lofland, J. S. Ramchandran, G. C. Xiong, H. L. Ju, T. Venkatesan and R. L. Greene, Euophys. Lett. **32**, 349 (1995)

84. B. Diney, V.S. Sperious, S. Metin, S. S. Parkin, B.A. Gurney, P. Baumgart, and D. R. Wilhoit, Appl. Phys. Lett. **69**, 4774 (1991)

85. S. Mathews, R. Ramesh, T. Venkatesan and J. Benedeho, Science **276**, 238 (1997)

86. A. Goyal, M. Reijeswari, R. Shrakala, S. E. Lofland, S. M. Bhagat, T. Boettcher, C. Kwon, R. Ramesh, and T. Venkatesan, Appl. Phys. Lett. **71**, 2535 (1997)

87. M. Rajeswari, C. H. Chen, A. Goyal, C. Kwo, M. C. Robson, R. Ramesh, T. Venkatesan, and S. Lakeou, Appl. Phys. Lett. **68**, 3555 (1996)

88. Ravi Bathe, K.P. Adhi, S. I. Patil, G. Marest, B. Honneyer and S. B. Ogale, Appl. Phys. Lett. **76**, 2104 (2000)

89. Z. W. Dong. T. Boehcher, C. H. Chen. Takeuchi, M. Rajeswari and T. Venkatesan, Appl. Phys. Lett. **69**, 3432 (1996)

90. Z. W. Dong, R. Ramesh, T. Venkatesan, M. Jackson, Z. Y. chen, S. P. Pai, R. Shreekala, R. P. Sharma C. J. Lobb. And R. L. Grceen, Appl. Phys. Lett. **71**, 1718 (1997)

91. V. A. Vasko. V. A. Larkin, P. A. Kraus. K. R. Nikolaev, D. E. Grupp. C. A. Nordman, and A. M. Goldman, Phys. Rev. Lett. **78**, 1134 (1997)

Chapter – II

2.1 Synthesis Methods

The synthesis of good quality material is a key to obtain the desired physical properties and single-phase structure. Hence the selection of sample preparation method plays an important role. High purity starting materials should be used to avoid the introduction of defects into the structure. It is very important to have single-phase compound of CMR material for detailed investigations. In order to prepare a single-phase sample, the synthesis conditions are also equally important. During synthesis, the parameters like temperature, pressure, gas flow and time for the reaction are needed to be varied according to the requirements in the sample. The selection of all the parameters has to be made to find the conditions, which are best for each sample, and to obtain desired phase. Generally, solid state reaction route or ceramic method is preferred for the synthesis of mixed valent manganite CMR materials.

2.1.1 Solid state reaction method

All the bulk polycrystalline samples under study are synthesized with solid state reaction method [1]. The general steps involved in solid-state reaction method for synthesizing CMR materials are described below.

1. All starting materials are high purity powders of carbonates, oxides, nitrides, etc. They are preheated for appropriate time and temperature in order to remove moisture in them. Powders are weighed for desired composition.
2. In the solid state reaction, for the reaction to take place homogeneously, it is very important to mix and grind the powders thoroughly for long duration to obtain homogeneous distribution in required proportions of the desired stoichiometric compound.
3. The proper grinding of mixed powders using pestle-mortar reduces the particle size as much as possible. This is necessary for obtaining close contact among the atoms.
4. This powdered mixture is then heated in air for the first time. This first calcination helps to remove the CO2 present in the mixture.

5. After the first heating, further number of heatings in atmosphere, are required to obtain phase purity and remove any traces of CO_2 present, if any. It is always better to increase temperature gradually during the series of heating.

6. Before final sintering of samples, fine black powder obtained is pressed into cylindrical pellets.

7. The pellets are sintered in a furnace in air at elevated temperatures to obtain the desired structural phase. The samples are allowed to furnace cool.

8. *Annealing:* After sintering, the samples may have oxygen content slightly less than the required stoichiometry in oxide systems. To reach the optimum oxygen content, the samples have to be annealed, preferably in flowing oxygen. Since most of physical properties of oxides are rather sensitive to oxygen content and ordering, the conditions set during the oxygen annealing are important. For appropriate oxygen content, the sintered pellets are usually kept for oxygen annealing at a desired temperature for a long period of time and then cooled down slowly to ambient temperature.

The solid-state reaction method has proved to be the most suitable to synthesizing the reproducible samples of oxide systems. These steps can be followed for synthesis of manganites by solid-state reaction route. Oxygen annealing is not required in some cases for manganite as these materials posses good stability of oxygen stoichiometry.

Preparation of CMR materials by solid state reaction

- Weigh and mix starting material
- Oxides, carbonates, nitrates etc. decompose by heat ~ 900 $^{\circ}$C
- Grinding and presintering at 1000 $^{\circ}$C & 1100 $^{\circ}$C
- Grinding and long presintering at 1200 $^{\circ}$C to 1300 $^{\circ}$C
- Grinding, add binder if necessary
- Final sintering between 1350 °C to 1400 °C

2.2.2 Sol-gel method

The sol-gel method is known to produce materials from solutions either in bulk, films, fibers or powder forms [2]. Concerning the microstructures, the sol-gel method is yields mainly porous materials, dense materials like glasses and ceramics, organic-inorganic hybrids and nanocomposites.

- Key points of the sol-gel method

1. Gelatinous materials as a precursor play a role of an anticoagulant of growing particles. The preparation of monodispersed particles systematically controlled in mean size and shape have been difficult by conventional methods. In this method, under the conditions of high ionic strength, growing particles are easily aggregated and thus uncontrolled in size and shape. On the other hand, by the sol-gel method, network of a gelatinous precursor prevents the particle aggregation.
2. The supersaturation of the system can be kept at a low level by gradual dissolution of the precursor and the separation of the nucleation and growth stage is performed. The essential conditions to form monodispersed particles are thus achieved.
3. The solid precursor plays an important role as a reservoir of metal ions and/or anions of the product, which makes it possible to produce monodispersed particles in large quantities.

A typical example of the sol-gel method, gel as a precursor, is exemplified below. The main steps follwed during this method are given.

1. Powders, alcohol, required acid and water are taken to prepare solutions. Precursors are made with water in one of them and they are mixed radiply. Generally, these solutions are made at room temperature.
2. Finally, the precursors are mixed in molecular ratio and kept for gelation for some period of time (generally in days).
3. This gel is dried at certain temperature for some period of time in air.
4. This dried powder is ground thoroughly by pestle-mortar and finally heat treatment is given to form the compound in a particular shape.

2.2 Structural and morphological studies

It is very essential to study structural properties of any material in order to determine the structural phase of the sample before carrying out any other studies on the material. Structural properties are closely related to the chemical characteristics of the atoms in the material and thus form the basics on which detailed physical understanding is built. Similarly, morphological studies are important for understanding the growth and packing density of grains in thin films or polycrystalline bulk materials. There are various techniques known to explore the structure and morphology of a material. These are used to ascertain single phase samples and detect deviations from the main structure as well as extracting the actual structure. The different techniques have different advantages and disadvantages and thus complement each other. To study the crystalline nature of a material, two techniques are widely used: 1) X-Ray diffraction (XRD) measurements and 2) Neutron diffraction (ND) measurements.

To study morphology of the samples, generally, Atomic Force Microscopy (AFM) or Scanning Electron Microscopy (SEM) are widely used experimental techniques. Transmission Electron Microscopy (TEM) is a useful tool to obtain cross sectional view of the thin films, especially when thin films are irradiated or exhibit defects in the inner structure. Thermo Gravimetric Analysis (TGA) and Iodometric titration are generally used to determine the oxygen stoichiometry in the materials.

2.2.1 X-Ray Diffraction (XRD)

X-Rays are having very small wavelength so that they can pass through most of the solid materials. The wavelength of X-rays is of the same order of magnitude as the distances between atoms or ions in a molecule or crystal. While passing through a crystal, X-rays are diffracted by atoms at specific angles depending on the X-ray wavelength, the crystal orientation, and the structure of the crystal. X-rays are predominantly diffracted by electrons and analysis of the diffraction angles produces an electron density map of the crystal. Crystalline materials can be described by their unit cell. This is the smallest unit describing the material. In the material the unit cell is then repeated throughout in all directions. This will result in planes of atoms at certain intervals. The diffraction method is based on this aspect of repetition and on Bragg's law which gives a relation between the distance from one atomic plane to the next 'd' and the angle, θ, at which constructive

interference of a reflected monochromatic beam is seen. The Bragg's law follows the equation given below.

$$2d\sin(\theta) = n\lambda \qquad [2.1]$$

where, **d** = interplanar distance, **n** = order of reflection (Integer value), **λ** = wavelength of X-rays, **θ** = angle between incident/ reflected beam and particular crystal planes under consideration.

We can see from eq^{n} 2.1 (Bragg's law) that, we need a beam with single well defined wavelength (monochromatic) in order to avoid interference in more than one direction for each planar distance. To obtain angles, the detector can be rotated. The wavelength of X-rays should be ~ d. Sintered CMR manganite samples contain grains with planes distributed in all directions. Scanning in 2θ, the angle between the incident beam and the diffracted beam, gives a diffraction pattern with peaks corresponding to the different planar distances. Figure 2.1 represents the X-ray diffraction mechanism in crystalline solids.

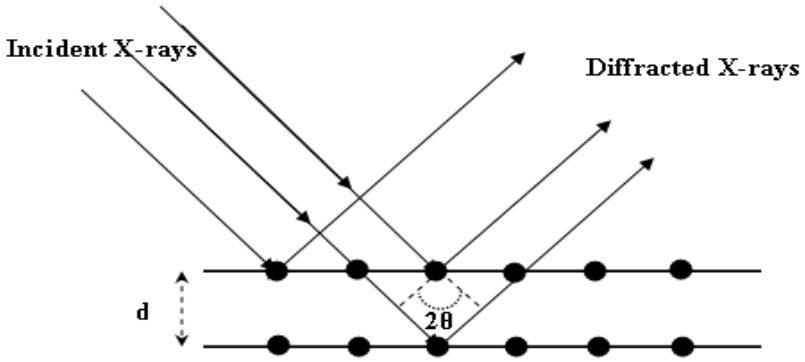

Figure 2.1: Diffraction of X-rays by a crystal planes (Bragg's law).

According to fig. 2.1, two noteworthy things are: a) Incident beam, the normal to the reflecting plane, and the diffracted beam are always coplanar. b) The angle between the diffracted beam and the transmitted beam is always 2θ, which is usually measured experimentally. The detailed description of XRD is given in references [3,4].

The structural studies for the samples under present study were performed by XRD and Rietveld refinement of XRD data. The Rietveld analysis is described below.

Rietveld Analysis

The Rietveld analysis [5,6] is a refinement method for powder diffraction patterns to study the nuclear and magnetic structures. To study the magnetic structure, polarized neutrons are needed. Once the structure is known, the analysis starts with an approximation of the lattice parameters and calculates the diffraction pattern for the structure. The structure is described with a large number of parameters, as is the experimental set-up. There are nine parameters for the experimental equipment: the wavelength, the scale factor, the zero point for 2θ and six parameters for a polynomial background. For the typical $LaMnO_3$ (ABO_3) type perovskite structure, most of the parameters have to be refined. The gradient for the weighted sum of squared difference between the calculated intensities and the measured intensities, R_p, can be determined relative to these parameters. The gradient is then used to change the parameters and this is repeated until a minimum in the Mp function is reached. The definition of R_p and the profile factors have been taken from the FULLPROF manual.

Intensity profile factor R_p is defined as,

$$R_p = 100 \frac{\sum_{i=1,n} |y_i - y_{c,i}|}{\sum_{i=1,n} y_i} \qquad \textbf{[2.2]}$$

where y_i is the observed intensity at angular step i, y_{ci} is the corresponding calculated intensity. To control the quality of the refinement, several agreement factors were calculated. The weighted profile factor R_{wp} is given by,

$$R_{wp} = 100 \left[\frac{\sum_{i=1,n} w_i |y_i - y_{c,i}|^2}{\sum_{i=1,n} w_i y_i^2} \right]^{1/2} \qquad \textbf{[2.3]}$$

and the expectation profile factor,

$$R_{exp} = 100 \left[\frac{n-p}{\sum_i w_i y_i^2} \right]^{1/2} \qquad \textbf{[2.4]}$$

The Bragg R- factor,

$$R_B = 100 \frac{\sum_{\mathbf{h}} \left| {}' I_{obs,\mathbf{h}} {}' - I_{calc,\mathbf{h}} \right|}{\sum_{\mathbf{h}} \left| {}' I_{obs,\mathbf{h}} {}' \right|} \qquad \textbf{[2.5]}$$

and crystallographic R_f – factor

$$R_F = 100 \frac{\sum_{\mathbf{h}} \left| {}' F_{obs,k} {}' - F_{calc,\mathbf{h}} \right|}{\sum_{\mathbf{h}} \left| {}' F_{obs,\mathbf{h}} {}' \right|} \qquad \textbf{[2.6]}$$

and the goodness of fit,

$$\chi^2 = \left[\frac{R_{wp}}{R_{exp}} \right]^2 \qquad \textbf{[2.7]}$$

Here, I_{obs} and I_{calc} are the observed and calculated integrated intensities for the different Bragg peaks j and (n - p) is the number of degrees of freedom. n - is the number of points in the pattern observed and p- is the number of refined parameters.

The refinements of the XRD of the samples in the present work were carried out using FULLPROF program. The order of refining the parameters was: the scale factor, the zero point for 2θ, five of the background parameters, the cell parameters, three of the peak shape parameters, the z co-ordinates, the isotropic displacement parameters, the occupation numbers, the fourth peak shape parameter, the anisotropic displacement parameters and the last background parameter. A few different routes to convergence were tried to confirm an optimal result. The R factors are good indicators if a route is not converging to a reliable result. Anisotropic displacement parameters at the Mn-O sites led to better refinements.

2.2.2 Neutron diffraction (ND)

Neutron diffraction has long been of importance for detecting light atoms, like hydrogen and oxygen, in the presence of heavy atoms like those of metals. There is a basic difference in diffraction of X-rays and neutrons by different materials, which makes

neutron diffraction as an essential tool for structural investigations. As discussed in earlier section, X-rays are scattered by electrons, and more the electrons present, the stronger is the scattering. Neutrons carry no electric charge. They are scattered by the atomic nucleus and the scattering amplitude depends therefore on the energy levels in the nuclei, atomic number and on properties of individual nuclei, which vary rapidly across the periodic table and from one isotope to another. Light atoms can therefore have scattering amplitudes as large as or larger than the heavy ones. This makes it possible to detect reflections from all the atoms in the materials. One complication is that some atoms absorb neutrons to a high degree and therefore give low scattering amplitude. Samarium is one example and hence Sm-123 superconductor cannot be studied by neutron diffraction. Since, while leaving the reactor, the neutrons posses too much high energies and short wavelengths for diffraction, their energy is lowered with a moderator consisting of water. After this process, the thermal neutrons have a wavelength of approximately 1 Å, of the order of the plane spacing, which can be used for experimental purpose.

2.2.3 Scanning Electron Microscopy (SEM)

SEM uses electrons as probes to form an image of the specimen. It is one of the most powerful and productive methods of microscopy yet invented [[i], [ii]]. The SEM has allowed researchers to examine a large variety of specimens. The scanning electron microscope has many advantages over traditional microscopes. The SEM has a large depth of field, which allows more of a specimen to be in focus at one time. The SEM also has much higher resolution; so closely spaced specimens can be magnified at much higher levels. As the SEM uses electromagnets rather than lenses, it is much more controlled in the degree of magnification. All of these advantages, as well as the actual strikingly clear images, make the scanning electron microscope one of the most useful instruments in research today.

Scanning Electron Microscope (SEM) has become a valuable tool for examination and evaluation of materials, both metallic and non-metallic, as well as assemblies and surfaces. This is a non-destructive technique in a way that sample can be extracted as such after scanning. The sample to be investigated is placed on a specimen stage inside a vacuum enclosure of the SEM station and is incident with a finely focused electron beam that can be static or swept in a cyclic fashion over the specimen's surface. The resulting signals that are produced when the scanning electron beam impinges on the surface of the sample

include both secondary emission electrons as well as backscattered electrons. These signals vary as the result of differences in the surface topography as the scanning electron beam is swept across the sample surface.

Working of SEM

The SEM produces a largely magnified image by using electrons instead of light to form an image. A beam of electrons is produced at the top of the microscope by an electron gun. The electron beam follows a vertical path through the microscope, which is held within vacuum. The beam travels through electromagnetic fields and lenses, which focus the beam down toward the sample. Once the beam hits the sample, electrons and X-rays are ejected from the sample.

Detectors collect these X-rays, backscattered electrons and secondary electrons and convert them into a signal that is sent to a screen similar to a television screen. This produces the final image. The secondary emission of electrons (figs. 2.2 and 2.3) from the specimen surface is usually confined to an area near the beam impact zone that permits images to be obtained at a relatively high resolution. These images as seen on a Cathode Ray Tube provide a three dimensional appearance due to the large depth of field of the Scanning Electron Microscope (SEM) and the shadow relief effect of the secondary electrons contrast. Figure 2.2 represents the schematic diagram of SEM explaining the experimental set up.

A typical SEM has a working magnification range of from 10 to 100,000 diameters. A resolution can be attainable ~ 100 Angstroms and a focus of 300 times that of an optical microscope. The large depth of field available with a SEM makes it possible to observe three-dimensional objects. The three-dimensional images produced allow different morphological features to be correctly interrelated and correctly analyzed.

The unique advantage of Scanning Electron Microscopy is that it does not need much samples loading activity and also, the thickness of the specimen is not a consideration. The surface of the sample may clean and smoothened before it is scanned. This helps in achieving better surface morphological and grain size information.

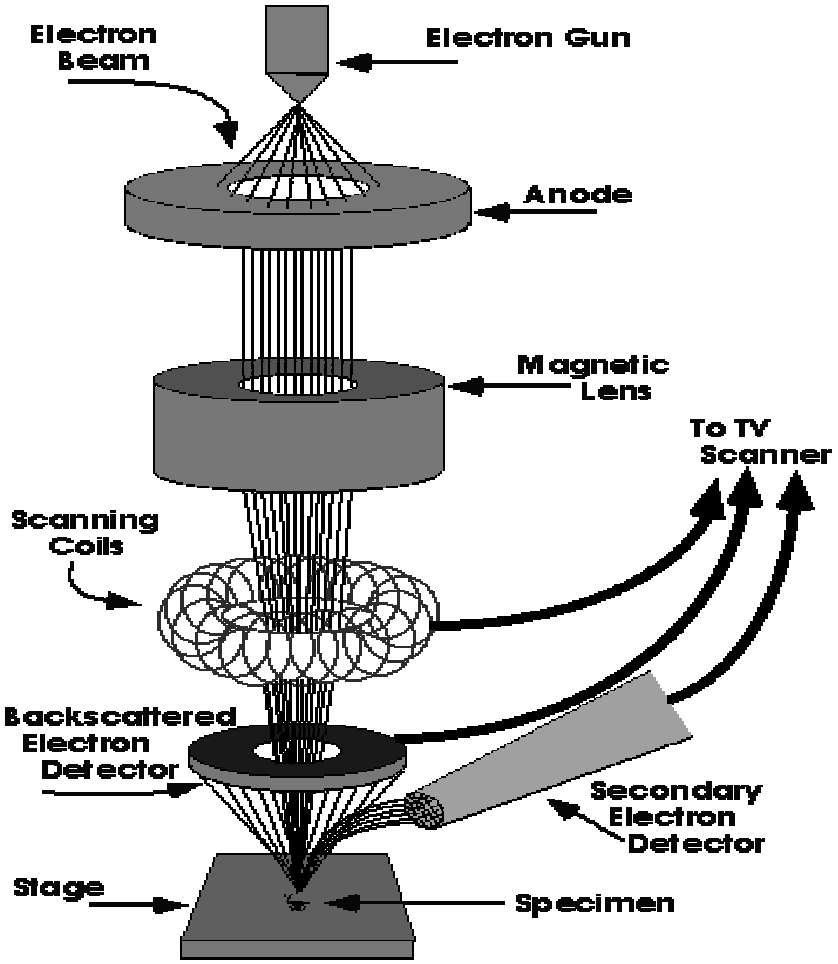

Figure 2.2: A diagram showing the working of scanning electron microscope (SEM) (Diagram courtesy of Iowa State University SEM Homepage).

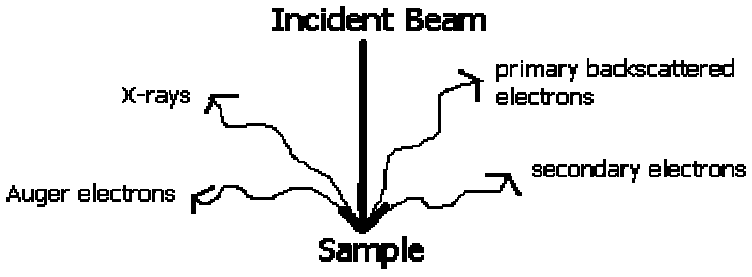

Figure 2.3: The outcomes of incident electron beam in a SEM

2.3 Electrical and Magnetotransport studies

The samples under present studies were characterized for their electrical and magnetotransport properties using the experimental techniques described below.

2.3.1 Standard four probe resistivity measurements

Electrical resistance measurements are rather easy and straightforward to make and provide much useful information about the sample. The normal state of the material is probed and the transition in the CMR material gives us an easily accessible and accurate value of the critical temperature as well as information about the quality of the sample.

A low contact resistance is desirable due to the small resistance of the samples. Hence a standard four-probe technique is used to measure resistance of the samples [9].

The samples were cut in a rectangular bar shape using a diamond saw. For the electrical contacts silver paste was used. The silver paste is applied at the ends for current contacts. Thin copper wires were connected with silver paint as shown in fig. 2.3 and the whole assembly was put onto a sample holder where the wires were connected with leads to the measuring instruments.

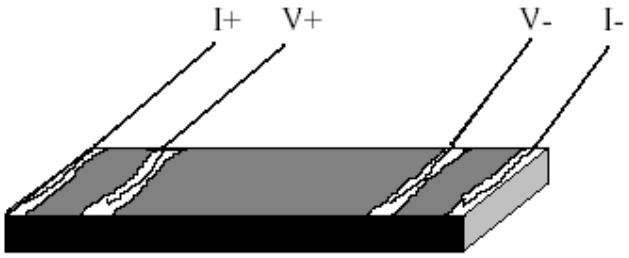

Figure 2.4: Four probe contacts of current and voltage supplies to the sample during the resistivity measurements.

The Kiethley instruments were used for the measurements. Thermal effects are automatically compensated during the measurements.

The samples were cooled down using suitable coolant liquid. The vacuum in the sample chamber was created by using rotary vacuum system. The samples were then heated in a controlled way by using a heater and the resistance was measured with slowly increasing temperature.

2.3.2 Magnetoresistive measurements

To study magneto resistive characteristics of the samples, resistance was measured by using the standard four probe method as explained in the previous section, in the presence of an external magnetic field in a Quantum Design Physical Properties Measurements System (PPMS). At a constant applied field, resistance was measured as a function of temperature (magneto R-T) in the range of RT to ~ 5 K. Most of the manganite samples studied in the present work were characterized using this technique.

2.4 Magnetic property measurements

2.4.1 A. c. susceptibility measurements

As described earlier, if a material exhibits superconductivity then it expels out the magnetic flux lines and shows negative of susceptibility (χ), which is defined as ratio of magnetization (M) to the applied magnetic field (H). Even very small amount of superconductor can display this effect, which can be measured []. Susceptibility is measured as a function of temperature for the materials. The samples under present investigations were also characterized by this technique to determine the magnetic transition temperature. A rectangular bar piece of sample was used for measurements of the samples. The piece of sample was weighed and loaded in the sample holder. Then it was cooled by using liquid He below its T_c (in the same set up which is used for R-T measurements). The sample was then heated in a controlled way and χ was measured by using a lock-in-amplifier.

2.4.2 D.C. magnetization and M-H measurements

For d. c. magnetization measurements of the samples, SQUID magnetometer or Vibrating Sample Magnetometer (VSM) was used. The measurement technique is described below along with the principle and working of the magnetometers used.

2.4.3 SQUID magnetometer

SQUID magnetometer is the most widely used instrument for magnetic characterization in material science. It has been proved as a boon to elucidate many interesting results in superconductors, manganites and ferrites [10]. The superconducting quantum interference device (SQUID) consists of two superconductors separated by thin insulating layers to form two parallel Josephson junctions. The device may be called as a

magnetometer to detect incredibly small magnetic fields. The SQUID has as its active element one or more Josephson junctions. A Josephson junction is a weak link between two superconductors that can support a super current below a critical value I_c. The special properties of the Josephson junction cause the impedance of the SQUID loop to be a periodic function of the magnetic flux threading the SQUID so that a modulation signal supplied to the bias current is used with a lock-in detector to measure the impedance and to linearize the voltage-to-flux relationship. The net result is that a SQUID functions as a flux-to-voltage converter with unrivaled energy sensitivity**.** In most practical systems in use today, the SQUID is located inside a small cylindrical, superconducting magnetic shield in the middle of a liquid helium Dewar, and shown in the fig. 2.6. Superconducting pickup coils, typically configured as gradiometers that detect the difference in one component of the field between two points, are located at the bottom of the Dewar and the sample is placed beneath the magnetometer. The rest of the hardware is designed to minimize helium boil off, eliminate rf interference, and to not contribute Johnson noise or distort any external a. c. fields [10]. The sensitivity of SQUID is associated with measuring changes in magnetic field of one flux quantum as shown in fig. 2.5.

If a constant biasing current is maintained in the SQUID device, the measured voltage oscillates with the changes in phase at the two junctions, which depends upon the change in the magnetic flux. The flux change can be evaluated by counting the oscillations. It may be noted that the sensitivity of SQUID is 10^{-14} Tesla, which is incredibly large to measure any magnetic signal.

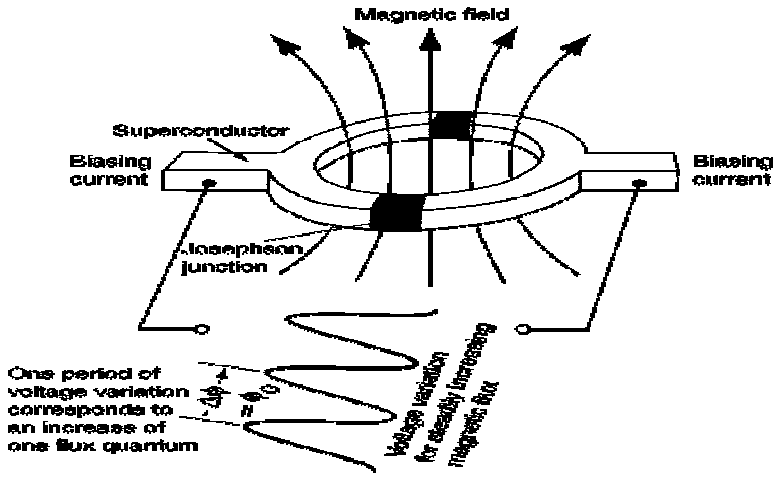

Figure 2.5: Variation of magnetic flux with change in voltage. ` `

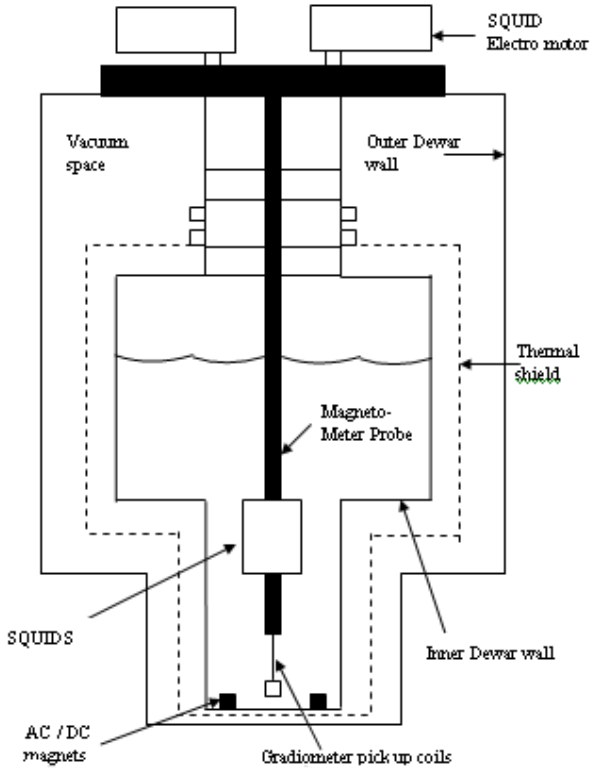

Figure 2.6: A schematic diagram of SQUID magnetometer.

Vibrating Sample Magnetometer

Vibrating sample magnetometer (VSM) is used to measure the magnetic moment of a material [11,12]. A VSM operates on Faraday's Law of Induction. According to Faraday's laws of magnetic induction, an ac voltage is induced which is proportional to the rate of change of magnetic flux associated with the circuit and thus to the amount of magnetic moment within the sample due to the applied magnetic field. A VSM operates by first placing the sample to be studied in a constant magnetic field. If the sample is magnetic, this constant magnetic field will magnetize the sample by aligning the magnetic domains or the individual magnetic spins, with the field. If the constant field is larger, the magnetization will also be larger. The magnetic dipole moment of the sample will create a magnetic field around the sample, sometimes called the magnetic stray field. The sample is vibrated with a certain frequency in the vertical direction near the detection coil. As the sample is moved up and down, this magnetic stray field changes as a function of time and can be sensed by a set of pick-up coils. An ac signal is generated at a frequency determined by the sample oscillation. This electric field can be measured and can give us

information about the changing magnetic field. This current will be proportional to the magnetization of the sample. The greater the magnetization, the greater will be induced current.

Oxford instruments design VSM [13] is used for these measurements with a few Tesla superconducting magnet. The material under investigation is mounted in a sample holder at the end of a carbon fiber rod and inserted in VSM continuous flow Helium Cryostat. The tail of the cryostat lies inside a conventional NbSn superconducting magnet capable of sustained fields up to 12 Tesla.

Once a DC field is applied, the sample is vibrated at a constant frequency of 66 Hz with amplitude of about 1.5mm along the vertical axis of the uniform applied field. Two pickup coils, placed above and below the sample, experience a change of the magnetic flux due to the motion of the sample and, according to Faraday's law, an emf induced is proportional to the rate of that change of flux. This signal, proportional to the magnetization of the sample, passes through a two-stage amplification process and is monitored by the VSM electronics and recorded on a computer via a standard RS232 connection. The sample temperature is measured by a AuFe/Chromel thermocouple in direct contact with a copper heat exchanger situated below the sample.

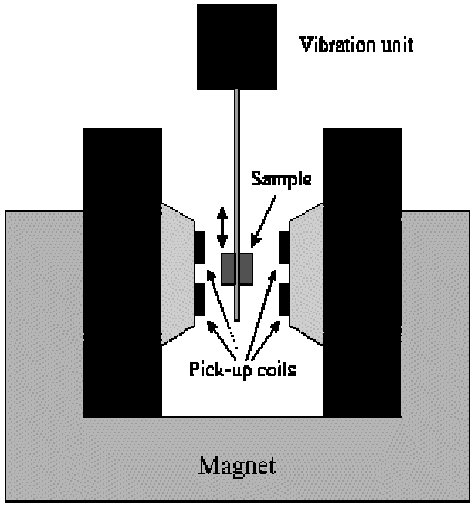

Figure 2.7: A Schematic diagram of VSM.

The temperature control (temperature range: 3.6 - 320 K) is achieved by an Oxford Instruments ITC4 temperature controller. A schematic diagram is shown in fig. 2.7.

The above mentioned measurement systems are used for d. c. magnetization and M versus H measurements of the samples. For d. c. magnetization, a small external field is applied and χ is measured as a function of temperature at constant applied field. For M-H measurements, magnetization (M in emu /gm) is measured at a constant temperature while magnetic filed is varied up to a certain value of positive and negative applied field.

References

1. E. M. Engler, Chem. Tecnol. **17**, 542 (1987).
2. G. Piccaluga, A. Corrias, G. Ennas, A. Musinu, Sol-gel preparation and characterization of Metal-Silica and Metal-Oxide silica nanocomposites (journal) **13**, 4 (2000).
3. A. Taylor, X-ray Metallography, Wiley (1961).
4. A. R. West, Solid State Chemistry and its Application, John Wiley & Sons, Chichester (1984).
5. H. M. Rietveld, J. Appl. Cryst. **2**, 65 (1969).
6. R.A. Young, The Rietveld Method, Oxford University Press Inc, New York, 1993.
7. Encyclopedia.Com (http://www.encyclopedia.com/printable/04033-a.html) and references therein.
8. Iowa State SEM Homepage (http://surf.eng.iastate.edu/~karie/Documentation) and references therein.
9. L. J. Van der pauw, Philips Res. Repts. **16**, 187 (1961).
10. SQUID Manual by Quantum Design
11. E. O. Samwel, T. Bolhuis, J. C. Lodder, Rev Sci Instrum. **69**, 3204 (1998).
12. E. O. Samwel, T. Bolhuis, D. Speliotis, J. C. Lodder, J Mag Magn Mater **193**, 337 (1999).
13. VSM manual by Oxford Instruments.

4. Encyclopedia.Com (http://www.encyclopedia.com/printable/04033-a.html) and references therein.

5. Iowa State SEM Homepage (http://surf.eng.iastate.edu/~karie/Documentation) and references therein.

Chapter – III

3.1 Studies on nearly low bandwidth $La_{1-2x}Pr_xCa_xMnO_3$ manganites.

The $LaMnO_3$ is the best suitable composition of the material, with the divalent doping normally alkaline earths like Ca^{+2}, Sr^{+2}, Ba^{+2} inducing remarkable electrical and magnetic transport properties like, metal-insulator (M-I) transition, paramagnetic to ferromagnetic (PM-FM) transition and charge ordering (CO) state with one more magnetic FM - AFM transition. The renewed Interest in these materials is due to the observation of huge amount of negative resistance exhibited by them under the application of magnetic field. They show remarkably half metallic behavior or spin polarized conduction and other remarkable features, which opened up the door of fascinating world, named as a mixed valent manganites. In nature, the mixed valent manganites means, the material containing Mn^{+3} and Mn^{+4}, which promotes the occurrence of the above mentioned phenomena [1]. Especially, creation of the Mn^{+4} in the material can be achieved by the way of several routes of the doping. Interestingly, reports exit on the creation of Mn^{+4} without doping at the divalent A-site due to the defect structure of perovskite block has attracted the attention of many working in this field [2,3].

The interesting feature of undoped $LaMnO_3$ is that, $LaMnO_{3+\delta}$ can be prepared under oxidizing condition. Although such a $LaMnO_{3+\delta}$ perovskite structure cannot accept excess oxygen in an interstitial site [3], non-stoichiometric excess oxygen fraction can be accommodated as cation vacancy. It may be either at A-site or B-site or at both the sites [4]. This has been described by the defect chemistry of these compounds using either TGA measurements or diffraction experiments [4-6]. Accordingly, the composition of $LaMnO_{3+\delta}$ is generally expressed as $La_{1+\delta}Mn_{1-\delta}O_3$ or $LaMn^{+3}_{1-2\delta}\ Mn^{+4}_{2\delta}O_{3+\delta}$ [4]. The oxygen defect amount δ produced in proportion of Mn^{+4} in sufficient amount, promotes M-I transition and other CMR properties. Several attempts have been made with defect structure of $LaMnO_3$ to obtain transition temperature in wide range of temperature between RT to low temperature.

The defect structure is mainly distinguished by orthorhombic, rhombohedral and cubic phase [7, 8]. The orthorhombic phase is stable over $0.10 \leq \delta \geq 0.18$ [4]. There is an anomaly with the δ value corresponding to amount of Mn^{+4} showing Mn^{+4} does not directly depend on δ [8, 9]. Hence, it can be argued that, the structural behavior of the

compound is the most prominent way to explain different CMR properties. Oxidation creates small polaron holes that become increasingly trapped at cation vacancies. The orthorhombic structure sustains the co-operative J-T distortion while the rhombohedral phase suppresses the co-operative J-T distortion so that the hole-pour matrix becomes ferromagnetic [9]. With highest δ having appropriate tolerance factor ***t*** creates delocalized state and introduces double-exchange mechanism. This ferromagnetic coupling competes with antiferromagnetic superexchange. [10, 11]

All the reports are found in favor of use of wet chemical methods to synthesize defect structure of $LaMnO_3$ [12]. Earlier report suggests that, conventional solid state reaction route does not create sufficient long range ferromagnetic order and insulator - metal (I-M) transition in undoped $LaMnO_3$ samples [13-15].

With an aim to create sufficient long range ferromagnetic order in the undoped $LaMnO_3$ sample by varying the Mn^{+4} content through Solid state reaction route, in this course of present work, we have attempted to synthesize the slightly cation deficient system such as $La_{1-2x}Pr_xCa_xMnO_3$ (LPCMO) (x = 0.00, 0.10 & 0.15). The results of the structural, transport, magnetotransport and magnetic property measurements on the doped LPCMO system have been described in detail in this chapter. The presence of Pr substitution plays a crucial role to achieve high negative MR. The results obtained on this system has prompted us to carry out more studies on the simultaneous doping of Pr, Ca (x = 0.20, 0.30) in LPCMO. The cation size plays a vital role to suppress and revive the transition temperature. The sensitivity of the material to the cation size is understood to have direct impact on Mn-O-Mn bond length that controls the carrier hopping amplitude. Some low bandwidth magnetic system like $Pr_{1-x}Ca_xMnO_3$ (PCMO) are charge ordered at all the compositions, but shows ferromagnetism from x = 0.2 - 0.3 [16, 17]. The system shows coexisting inhomogeneous metal-insulator (M-I), ferromagnetic (FM) and antiferromagnetic (AFM) phases around 100 K. However it exhibits M-I transition under magnetic field and when exposed to X- rays [18-21]. The smaller size of Pr reduces the Mn-O-Mn bond angle making super-exchange competitive with Zener double exchange.

The other manganite system $La_{1-x}Ca_xMnO_3$ (LCMO) shows prominent transport and magnetic transitions for x = 0.18 - 0.50 [22]. Hence, it would be interesting to investigate the structural, transport, magnetic and magnetotransport properties of the

simultaneous Pr-Ca doped for La in $LaMnO_3$ perovskite. Average A-site cation radius $<r_A>$ decrases by the simultaneous substitution of smaller cation Pr and Ca, which leads to nearly a low bandwidth system.

Sample Preparation

The series of samples with stoichiometric compositions $La_{1-2x}Pr_xCa_xMnO_3$ (x = 0.0, 0.10, 0.15, 0.20 & 0.30) and $La_{0.5}Pr_{0.2}Ca_{0.3}MnO_3$ were synthesized using standard solid-state reaction method. The appropriate amounts of pure La_2O_3, Pr_6O_{11}, MnO_2, and $CaCO_3$ chemicals were thoroughly ground and mixed. The calcinations and sintering, with intermittent grindings were done in the temperature range of 900 ºC – 1100 ºC. Samples were annealed under the flow of nitrogen for 12 hrs. followed by oxygen annealing for 24 hrs followed by slow cooling down to room temperature (RT).

3.1.1 Structural studies

The structural studies on all the $La_{1-2x}Pr_xCa_xMnO_3$ (x = 0.0, 0.10, 0.15, 0.20, 0.30) samples have been carried out using XRD facility at Department of Physics, University of Pune and IUC-DAEF, Indore. The measurement parameters were 2θ ranges 20 º - 80º, step size - 0.02º and step time 1.00 sec.

Figs. 3.1, 3.2 and 3.3 shows the XRD patterns for pure $LaMnO_3$ (x = 0.0), $La_{1-2x}Pr_xCa_xMnO_3$ (x = 0.10 & 0.15) respectively.

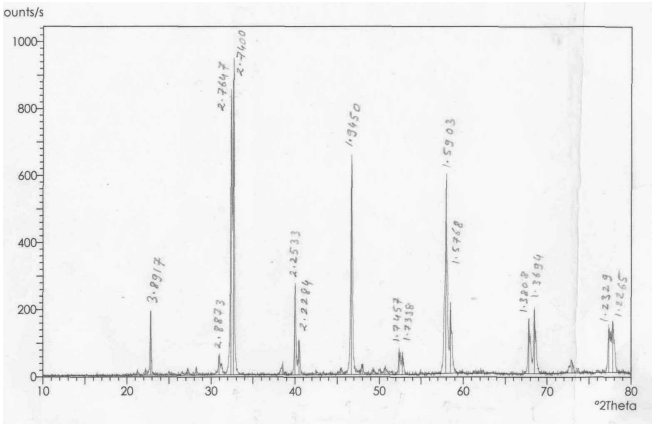

Figure: 3.1 XRD pattern of undoped $LaMnO_3$ (x = 0.0).

The structural study on x = 0.0, i.e. $LaMnO_3$ sample has been carried out in the light of variation in Mn_{+4} content due to the defect structure resulting from the synthesis technique used in sample preparation. It is reported that, the structure of $LaMnO_3$ changes from orthorhombic to rhombohedral as a function of Mn^{+4} [7, 8]. Fig. (3.1) clearly shows

that, the sample x = 0.0 possess a mixed phase orthorhombic and rhombohedral behavior. The doublet peaks indicate the presence of both the phases. The 100 % intensity peak can be indexed in rhombohedral structure with a_0 = 5.523 A, b_0 and c_0 = 13.324 A. The 84 % intensity peak just before 100 % peak in the form of doublet is indexable in orthorhombic structure with space group = Pnma (62). The XRD pattern of x = 0.0 also can be indexed in the similar pattern in which the intensity of rhombohedral structured peaks dominates over the orthorhombic phase peaks [23].

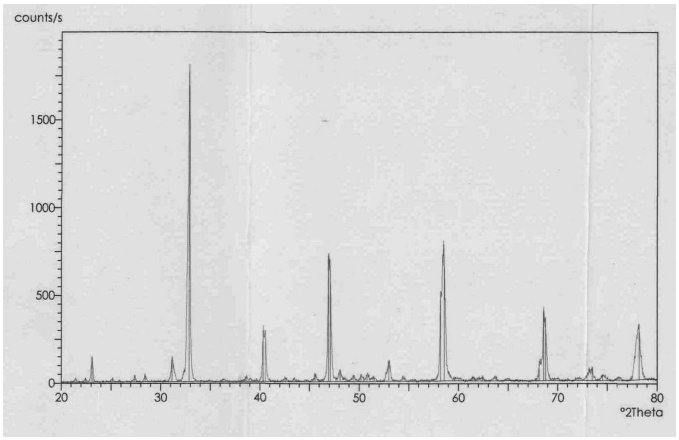

Figure: 3.2 XRD pattern of $La_{1-2x}Pr_xCa_xMnO_3$ (x = 0.10).

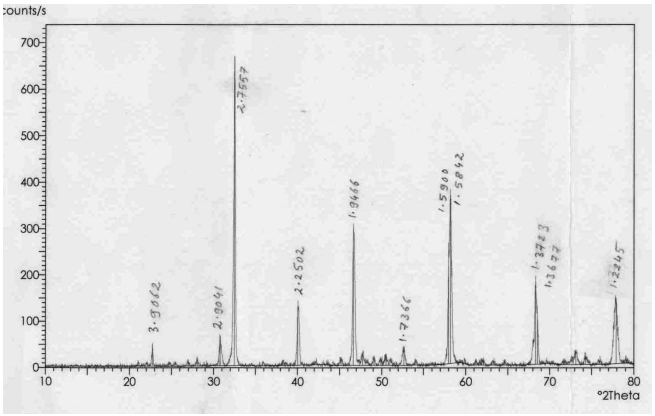

Figure: 3.3 XRD pattern of $La_{1-2x}Pr_xCa_xMnO_3$ (x = 0.15).

The progressive simultaneous substitution of Pr-Ca at La in $LaMnO_3$ results into the conversion of doublet peaks into singlet, as evident from figs. 3.2 and 3.3. For x = 0.10, the three doublets are seen to be dissolved and becomes singlet with 100% maximum peak indexable in rhombohedral reflection. For x = 0.15 (fig. 3.3), the system is structurally converted to orthorhombic phase with the possibility that x = 0.18-0.20 as the

concentration of doping for the occurrence of pure orthorhombic structure exhibiting M-I transition and CMR behavior.

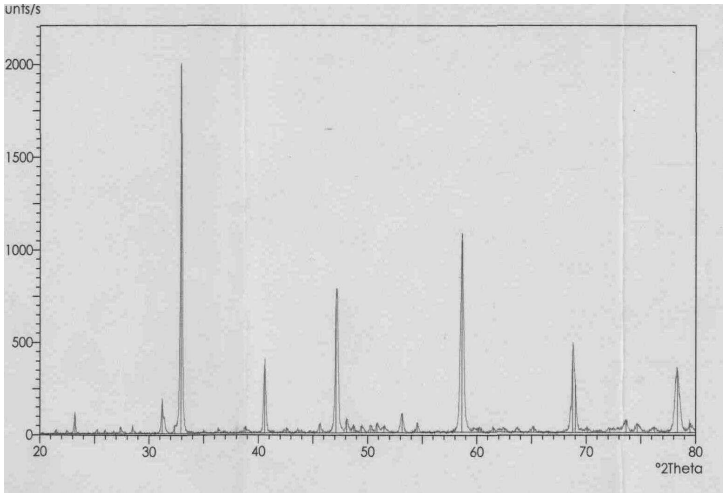

Figure: 3.4 XRD pattern of $La_{1-2x}Pr_xCa_xMnO_3$ (x = 0.20).

Fig. 3.4 shows the observed XRD pattern for x = 0.20 sample showing that almost all the peaks can be indexed in an orthorhombic structure with space group Pbnm (62). The presence of a low intensity peak before 100 % peak in this sample has been discussed at the end of this section.

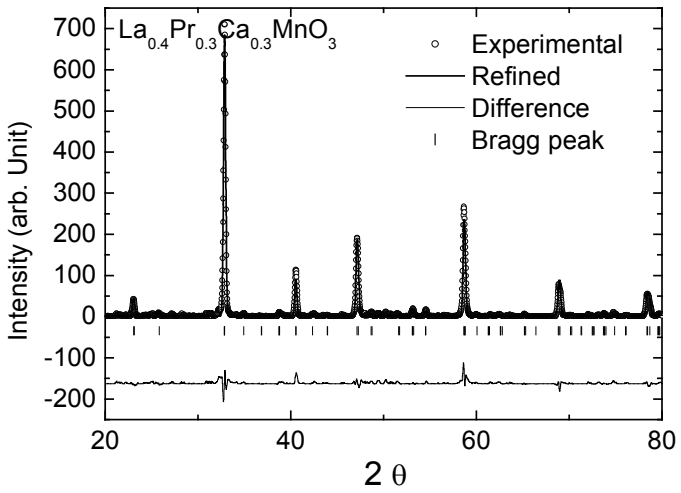

Figure: 3.5 Rietveld fitted XRD pattern of $La_{1-2x}Pr_xCa_xMnO_3$ (x = 0.30).

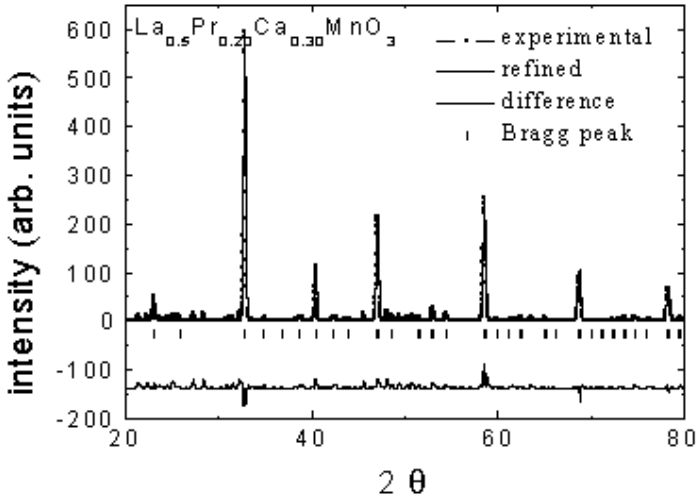

Figure: 3.5 Rietveld fitted XRD pattern of $La_{0.5}Pr_{0.2}Ca_{0.3}MnO_3$ system.

Figs. 3.5 and 3.6 depicts the rietveld fitted XRD patterns for $La_{1-2x}Pr_xCa_xMnO_3$ x = 0.30 and $La_{0.5}Pr_{0.2}Ca_{0.3}MnO_3$ sample respectively. It can be seen from the patterns that samples possess single phase orthorhombic structure.

The weak intensity peak before the 100 % maximum peak in the XRD patterns of all the samples studied cannot be indexed in the rietveld fitting. Moreover, it does not match with the unreacted 100 % La_2O_3 peak. Also, there is an absence of Mn_2O_3 peak in the XRD patterns, which suggest that this peak is indexable under JCPDS $LaMnO_3$ structural data as (0 2 0) symmetry reflection. Earlier work reported by B. Reveau et al, J. B. Goodenough et al and C. N. R. Rao et al have shown that this weak intensity reflection can be indexed under distorted orthorhombic structure as (0 2 0) plane.

3.2 Transport and magnetotransport measurements

$LaMnO_3$

The results of the transport and magnetotransport measurements on $LaMnO_3$ and $La_{1-2x}Pr_xCa_xMnO_3$ (x = 0.10, 0.15, 0.20 & 0.30) samples carried out using standard four probe resistance technique with and without applied magnetic field have been given in this section.

Fig. 3.7 shows the variation of resistance as a function of temperature for pure

$LaMnO_3$ with and without application of magnetic field. The inset figure shows the R-T behavior of $LaMnO_3$ at low temperature up to 5 K.

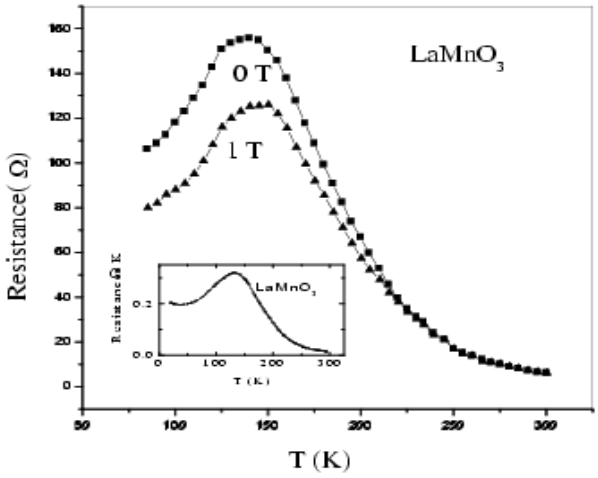

Figure: 3.7 R – T and Magneto R – T plots under 1T field of undoped $LaMnO_3$.

It is clear from the figure that the application of 1T field suppresses the peak resistance by an appreciable value, which can be quantified as negative peak magnetoresistance at I-M transition. The observation of I-M transition in pure $LaMnO_3$ under 0 T can be ascribed to the possible defect structure, which creates sufficient Mn^{4+} (~ 24 %) [7, 8, 23] responsible for FMM state in the sample which break the AFM interactions between Mn^{3+} ion. The observation of slight up turn in the metallic R-T behavior at low temperature (around 50 K), as shown in the inset figure, indicates the development of insulating phase in the FMM matrix. This is an evidence of the presence of orthorhombic distortion in the structure of the sample at low temperature.

$La_{1-2x}Pr_xCa_xMnO_3$ for x = 0.10, 0.15, 0.20, 0.30

In this section, the results of the studies on transport and magnetotransport behavior of Pr-Ca doped LCMO system have been given followed by the discussion on these results.

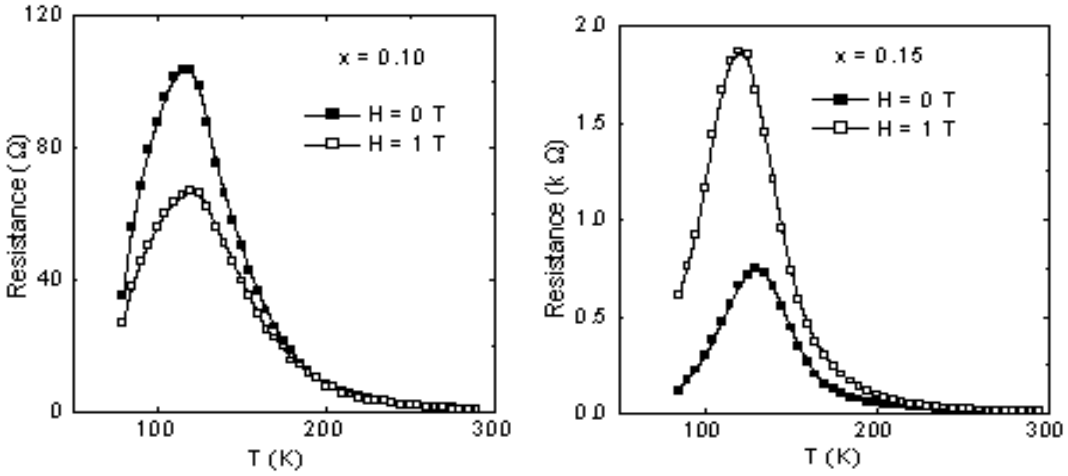

Figure: 3.8 R – T and Magneto R – T plots of $La_{1-2x}Pr_xCa_xMnO_3$ (x = 0.1).

Figure: 3.9 R – T and Magneto R – T plots of $La_{1-2x}Pr_xCa_xMnO_3$ (x = 0.15).

Figures 3.8 and 3.9 show the R-T and magneto R-T behavior of x = 0.10 and 0.15 samples of LPCMO respectively. The values of the I-M transition temperatures for these samples have been tabulated in table 3.1. The increase in Pr concentration results into an increase in peak resistance and narrowing of I-M transition region. As it is difficult to control the cation deficiency in the lower doping regime of Pr-Ca substitution in the solid state reaction method of sample synthesis, the variation in I-M transition temperature (T_p) with doping concentration does not follow any systematic [9].

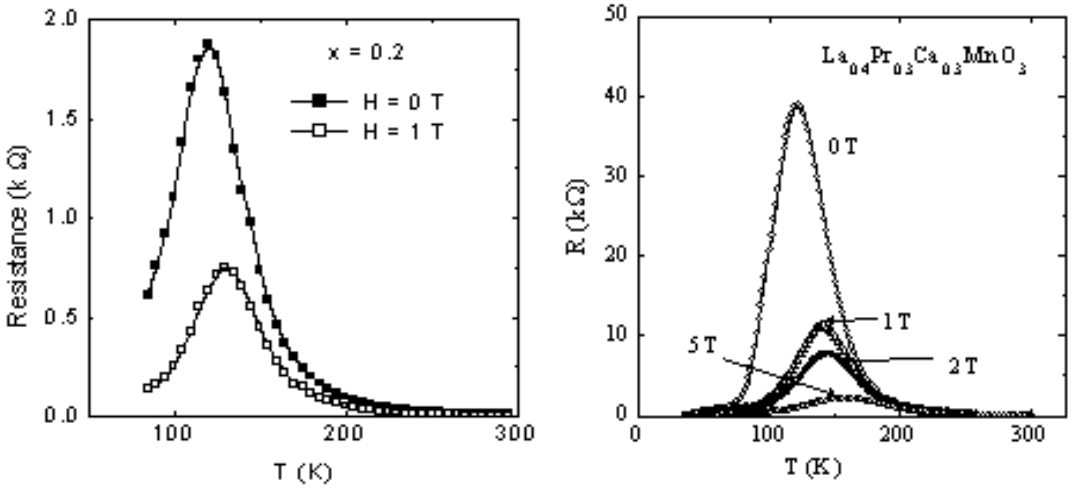

Figure: 3.10 R – T and Magneto R – T plots of $La_{1-2x}Pr_xCa_xMnO_3$ (x = 0.2).

Figure: 3.11 R – T and Magneto R – T plot of $La_{1-2x}Pr_xCa_xMnO_3$ (x = 0.3).

It is evident from figs. 3.10 and 3.11 that, the peak resistance at T_p becomes highest (~ 38 K) for x = 0.30 sample with no change in the T_p value. The samples with x = 0.20 and 0.30 Pr-Ca doping concentrations are well above the minimum limit of 18 % Mn^{4+} content sufficient for long range ferromagnetic material throughout the sample. This is accompanied by structural phase transition from rhombohedral to orthorhombic phase for x = 0.20 and 0.30 samples [5]. In addition, with the increase in Pr-Ca concentration results into sharpening of the I-M transition and enhance suppression of peak resistance at T_p in an applied field of 1 T.

$La_{0.5}Pr_{0.2}Ca_{0.3}MnO_3$

The R-T and magneto R-T measurements on the optimally Ca doped $LaMnO_3$ with Pr doping of 20 % at La site were carried out under an applied fields of 1 T, 2 T and 5 T. From the fig. 3.12, it can be seen that the T_p increases from 122 K to 150 K with the decrease in Pr content from x = 0.30 to 0.20 with Ca content remaining x = 0.30.

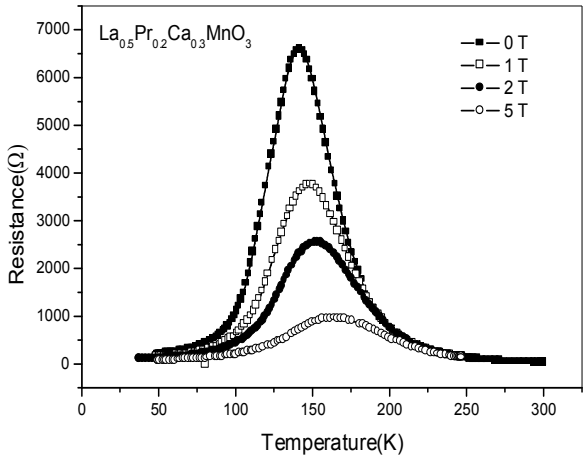

Figure: 3.12 R – T and Magneto R – T plots of $La_{0.5}Pr_{0.2}Ca_{0.3}MnO_3$.

Also, The peak resistance decreases from 38 K (Pr, Ca = 0.30) to 6.8 K (Pr = 0.20, Ca = 0.30) sample. In this sample it is observed that the amount of suppression of peak resistance under 1 T applied magnetic field is reduced as compared to $La_{1-2x}Pr_xCa_xMnO_3$ for x = 0.30 sample.

Conduction in Paramagnetic Insulator (PI) state or Paramagnetic Semiconductor (PS) mode

In this section we have attempted to understand the mechanism of charge conduction in PI state. Although, this state has been explored less effectively for understanding the conduction mechanism due to its insulating nature, but is interesting because it also exhibits negative MR. It is reported that there is a need to investigate the nature of electrical transport for the region $T > T_p$. In an attempt to know whether the nature of conduction above transition temperature in the $La_{1-2x}Pr_xCa_xMnO_3$ for x = 0.30 and $La_{0.5}Pr_{0.2}Ca_{0.3}MnO_3$ systems is governed by variable range hopping (VRH) or small polaron formation, we have fitted the R-T data above T_p in both the models [24, 25]. Figs. 3.13 and 3.14 show the VRH and small polaron fitting plots of $La_{1-2x}Pr_xCa_xMnO_3$; x = 0.30 and $La_{0.5}Pr_{0.2}Ca_{0.3}MnO_3$ samples.

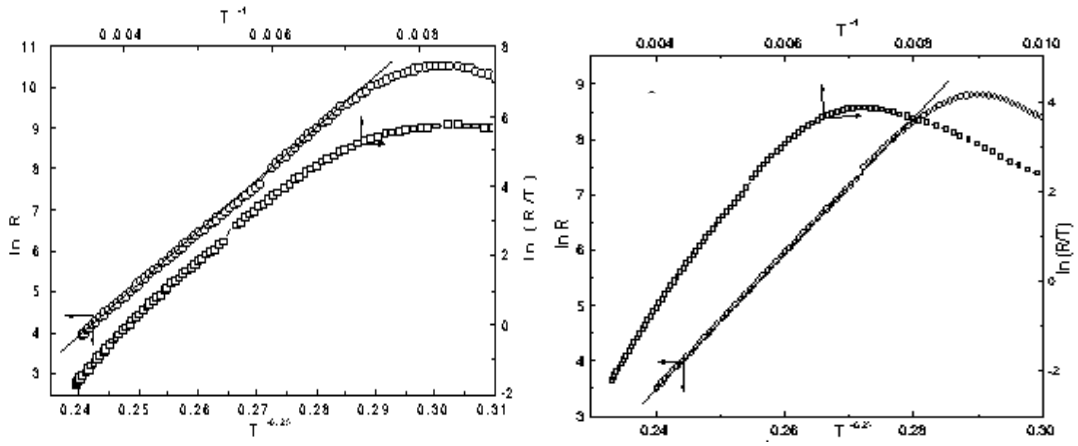

Figure: 3.13 VRH and small polaron model fitting of R-T of $La_{0.4}Pr_{0.3}Ca_{0.3}MnO_3$.
Figure: 3.14 VRH and small polaron model fitting of R-T of $La_{0.5}Pr_{0.2}Ca_{0.3}MnO_3$.

It can be seen from the fitted plots that, Motts type variable range hopping (VRH) model holds good throughout the temperature region above TC corresponding to the expression in the $\rho = \rho_0 \exp(T_0/T)^{1/4}$ while the fitting of R-T data into nearest neighbor small polaron hopping model corresponding to $\rho = AT \exp(E_0/kT)$ is non-linear in the higher temperature regime. This suggests that the charge carrier conduction in the PI state obeys the Motts VRH model. T0 in the equation is related to localization length by equation,

$$KT_0 = 18/L^2 N(E)$$

where L is the localization length of the carriers and N(E) is the density of the states.

3.2.2 Magnetoresistance studies

The values of the magnetoresistance (MR) calculated from the magneto R-T measurements carried out under 1 T for LaMnO3 and $La_{1-2x}Pr_xCa_xMnO_3$ (x = 0.10, 0.15 & 0.20) samples under different fields 1 T, 2 T & 5 T for $La_{0.4}Pr_{0.3}Ca_{0.3}MnO_3$ and $La_{0.5}Pr_{0.2}Ca_{0.3}MnO_3$ samples have been given in Table 3.1.

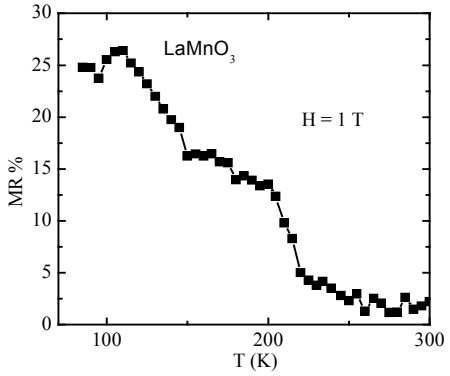

Figure: 3.15 MR % Vs Temperature plot of $LaMnO_3$ under 1T field.

It can be seen from the figure that the presently studied pure $LaMnO_3$ sample exhibits high MR effect under the application of 1 T field having an appreciable rise in its value at 225 K indicative of a reasonable MR% in PI or PS state also. The MR % becomes maximum around T_p.

$La_{1-2x}Pr_xCa_xMnO_3$ (x = 0.10, 0.15, 0.20) system

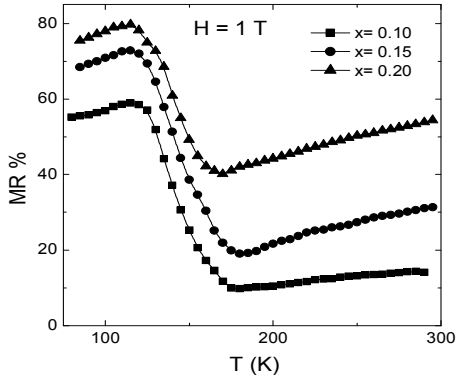

Figure: 3.16 MR % Vs Temperature plot of $La_{1-2\,x}Pr_xCa_xMnO_3$ under 1T field.

Fig. 3.16 depicts the variation of MR % with T (K) for different Pr-Ca (x) doping concentrations in $La_{1-2x}Pr_xCa_xMnO_3$ (x = 0.10, 0.15 & 0.20) systems under 1 T field. The values of the MR % obtained from magneto R-T data at T_p are tabulated in Table 3.1. It can be seen from the figure that, for x = 0.10 and 0.15 samples the MR behavior is almost similar with maximum MR ~ 57 % for x = 0.10 and ~ 70 % for x = 0.15. Both systems are slightly cation deficient systems. The sample x = 0.20 shows high MR% at low temperature up to 200 K having a maximum of ~ 80 % near T_p. In a relatively weak applied field of 1 T, the observation of such a high MR at 125 K is an interesting result.

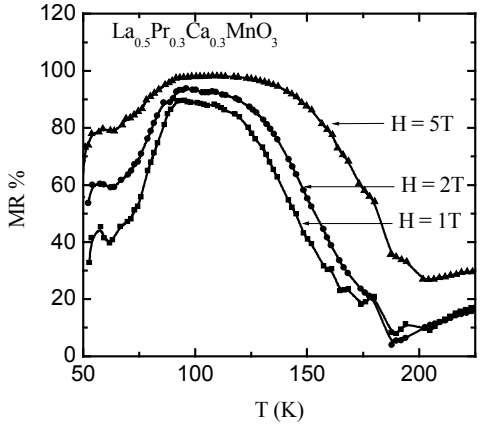

Figure: 3.17 MR % Vs Temperature plot of $La_{0.4}Pr_{0.3}Ca_{0.3}MnO_3$ under 1 T, 2 T and 5 T.

It can be mentioned that, the observation of such an appreciable MR effect (80 % & 85 %) under 1 T for LPCMO (x = 0.20, 0.30), is a result, which should attract the application potential of this sample well above the LN_2 temperature. The origin of this large CMR effect at relatively weaker fields lies in the magnetic disorder at Mn-O couplings and grain boundary effects [27]. The T_C depends upon the transfer integral of e_g electron, which further depends upon the spin arrangements on the adjacent Mn ions. If the Mn-O-Mn bond angle is towards 180º then the spin arrangement on Mn ions is ferromagnetic which favors the transfer of e_g electron easily but deviation from this angle obstructs the conduction of e_g electron and hence T_C occurs at low temperatures. The application of magnetic field forces parallel alignment of the spins and e_g electron transfer increases to show a drop in resistivity and hence CMR effect occurs when spins order ferromagnetically on Mn-O couplings [28]. The grain boundaries also contribute to resistivity by the spin dependent scattering of carriers. The application of magnetic field

reduces the spin dependent scattering of carriers and contributes to CMR effect [27]. The large sensitivity of the LPCMO system at weak fields prompted us to modify the system to a larger bandwidth by the substitution of larger size cation, which will be described in next chapter.

The similar behavior of pronounced MR effect has been observed in sample with x = 0.30 (fig. 3.17). It can be seen from the figure that the peak resistance is ~ 38 K (with a huge suppression in its value under the application of 1 T field resulting into MR ~ 85%. Fig. 3.18 shows the variation of MR% with the temperature for $La_{0.5}Pr_{0.2}Ca_{0.3}MnO_3$ system under 1 T, 2 T and 5 T applied field. The sample exhibiting a peak resistance of ~ 6.8 K exhibit MR ~ 40 % near T_p (140 K) under 1 T while the maximum MR ~ 85 % has been observed in 5 T field.

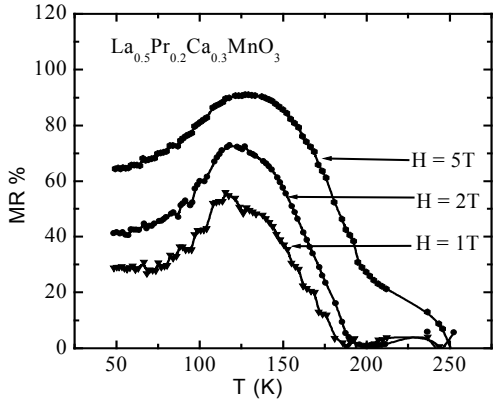

Figure: 3.18 MR % Vs Temperature plot of $La_{0.5}Pr_{0.2}Ca_{0.3}MnO_3$.

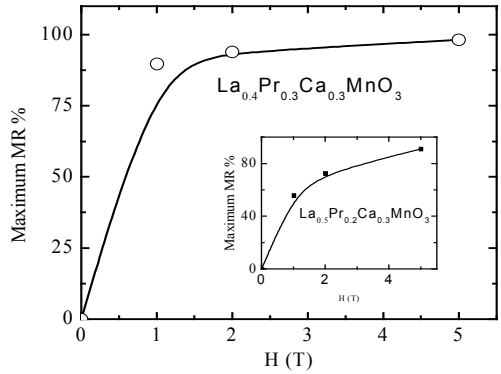

Figure: 3.19 Maximum MR% Vs field for $La_{0.4}Pr_{0.3}Ca_{0.3}MnO_3$ and $La_{0.5}Pr_{0.2}Ca_{0.3}MnO_3$.

Fig. 3.19 and its inset, shows the dependence of maximum MR % observed for x = 0.3 sample and $La_{0.5}Pr_{0.2}Ca_{0.3}MnO_3$ sample at different applied fields. It can be observed from these figures that, in both the samples the MR behavior is sensitive in the fields up to 2 T with the x = 0.30 samples showing an appreciable rise in MR at 1 T field.

3.3 Magnetization measurements

This section describes the results of the magnetic measurements carried out using a.c. susceptibility and D.C. magnetization measurements using VSM facility. The a.c. susceptibility measurements were performed on undoped $LaMnO_3$ and x = 0.10, 0.20 samples while the D.C. magnetization measurements carried out for x = 0.10, 0.15, 0.20 & 0.30 samples.

3.3.1 A. C. susceptibility

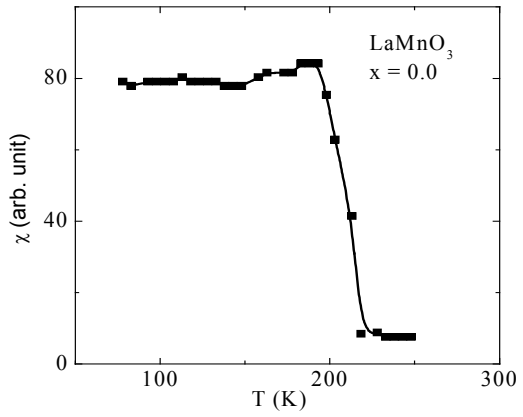

Figure: 3.20 A.C. susceptibility plot of $LaMnO_3$.

Fig. 3.20 shows the temperature dependence of a.c. susceptibility of $LaMnO_3$ sample showing strong ferromagnetic transition at T_C ~ 225 K. In this sample the I-M transition temperature (T_p ~ 140K) does not coincide with magnetic transition (T_C ~ 225 K), which has been often observed in the cation deficient system [8]. The disparity between T_p and T_C shows that there is a possibility of electronic phase separation in the sample. Figs. 3.21 and 3.22 depicts the a.c. susceptibility curves for x = 0.10, 0.20

samples (H = 6 Oe) and x = 0.30 (H = 50 Oe) showing the strong ferromagnetic transition varying with the dopant concentration x.

$La_{1-2x}Pr_xCa_xMnO_3$ (x = 0.10, 0.15, 0.20)

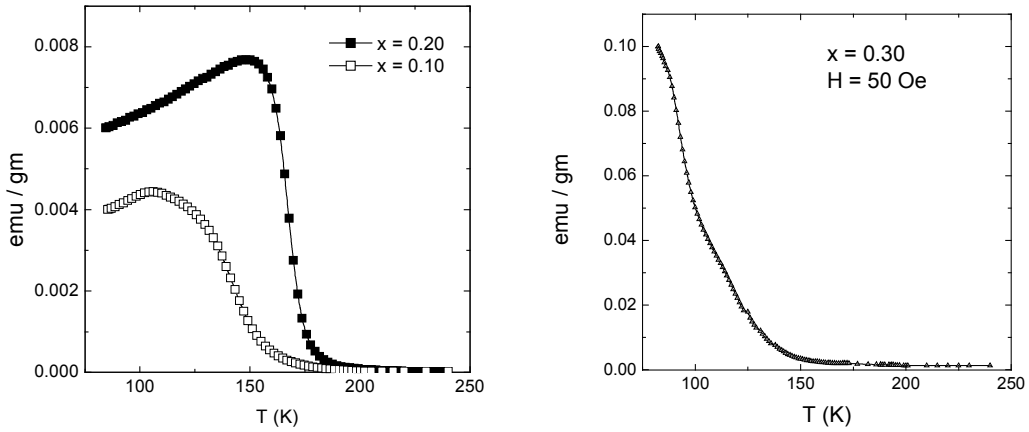

Figure: 3.21 a.c. susceptibility plot of $La_{1-2x}Pr_xCa_xMnO_3$ for x = 0.10, 0.20.

Figure: 3.22 a.c. susceptibility plot of $La_{1-2x}Pr_xCa_xMnO_3$ for x = 0.30.

Fig. 3.23 (a, b, c, d) shows the hysterics curves obtained under 1 T for all the LPCMO (x = 0.10, 0.15, 0.20, 0.30) samples. We have measured hysteresis behavior under 1T because the large MR% has been observed under the same field in these samples. It can be seen from the figures that with the increase in Pr-Ca (x) concentration the emu/gm value increases up to x = 0.20 with an increase in MR% (Table 3.1). In the case of x = 0.30 there is an anomaly showing that the magnetization does not saturate up to 1 T and the emu/gm value is lower in this sample.

3.3.2 D.C. Magnetization

Fig. 3.23 (a, b, c, d) shows the hysterisis curves obtained under 1T for all the LPCMO (x = 0.10, 0.15, 0.20, 0.30) samples. We have measured hysteresis behavior under 1T because the large MR% has been observed under the same field in these samples. It can be seen from the figures that with the increase in Pr-Ca (x) concentration the emu/gm value increases up to x = 0.20 with an increase in MR % (Table 3.1). In the case of x = 0.30 there is an anomaly showing that the magnetization does not saturate up to 1 T and the emu/gm value is lower in this sample.

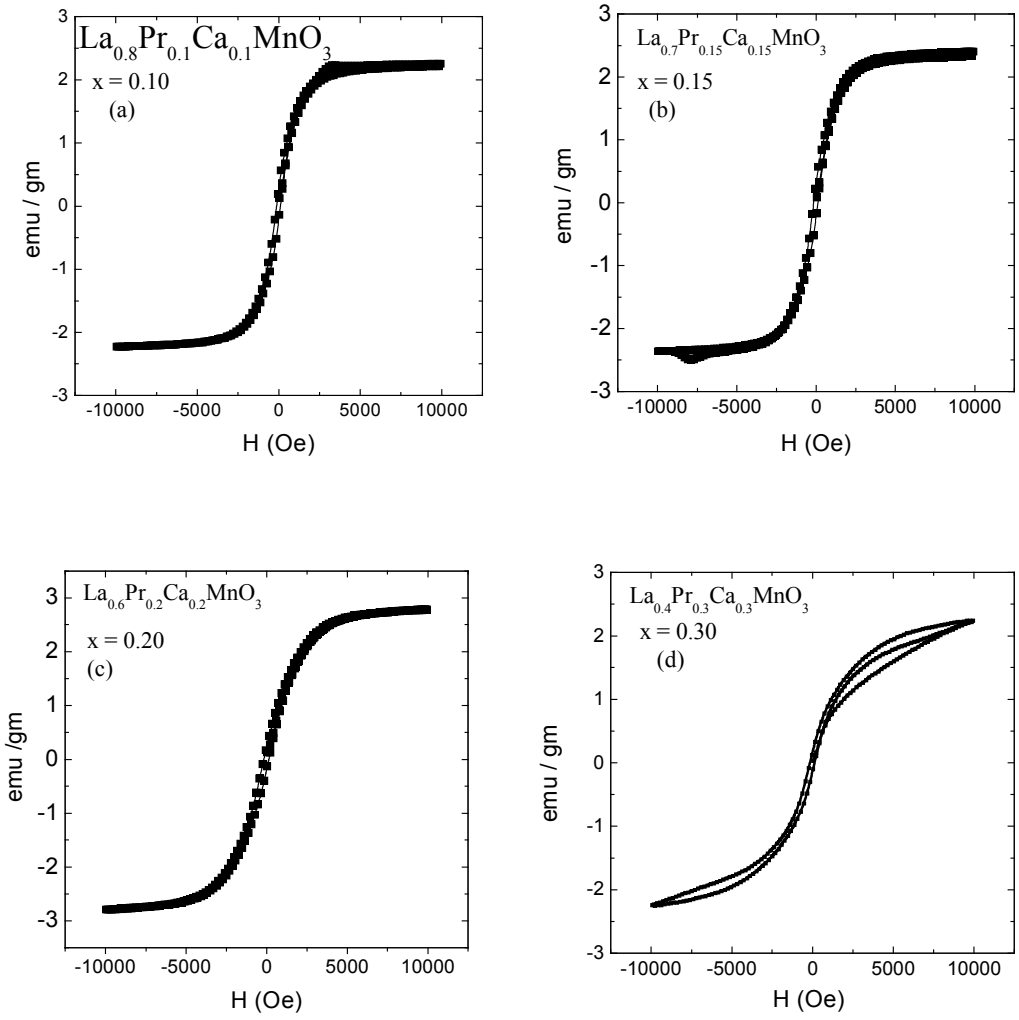

Figure: 3.23 Hysterisis loops of $La_{1-2x}Pr_xCa_xMnO_3$ (x = 0.10, 0.15, 0.20, 0.30) under 1 T.

Table: 3.1 Values of T_p and T_C, MR % (1 T) and emu/gm determined for $La_{1-2x}Pr_xCa_xMnO_3$ (x = 0.10, 0.15, 0.20 and 0.30) and $La_{0.5}Pr_{0.2}Ca_{0.3}MnO_3$ samples.

$La_{1-2x}Pr_xCa_xMnO_3$	~ T_p (K)	~ T_C (K)	~ MR % (1 T)	emu/g
x = 0.10	120	175	57	2.25
x = 0.15	122		72	2.40
x = 0.20	122	184	80	2.78
x = 0.30	122	150	89	2.21
$La_{0.5}Pr_{0.2}Ca_{0.3}MnO_3$	150	160	45	

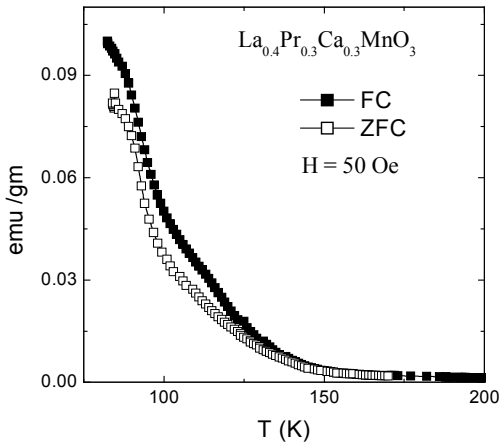

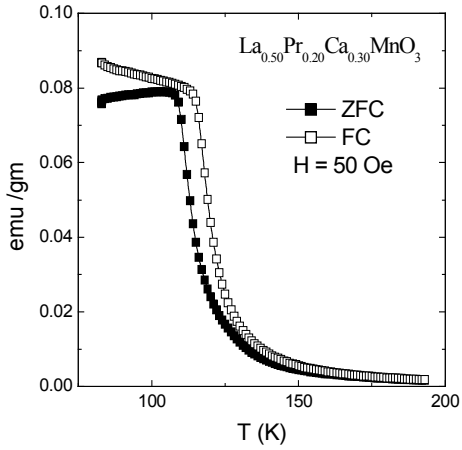

Figure: 3.24 ZFC and FC curves of $La_{0.4}Pr_{0.3}Ca_{0.3}MnO_3$ under 50 Oe.

Figure: 3.25 ZFC and FC curves of $La_{0.5}Pr_{0.2}Ca_{0.3}MnO_3$ under 50 Oe.

Figs. 3.24 and 3.25 shows ZFC and FC curves for $La_{0.4}Pr_{0.3}Ca_{0.3}MnO_3$ (x = 0.30) and $La_{0.5}Pr_{0.2}Ca_{0.3}MnO_3$ samples under 50 Oe fields. The curves for x = 0.30 sample shows the presence of anisotropic nature in the magnetization more pronounced as compared to $La_{0.5}Pr_{0.2}Ca_{0.3}MnO_3$ (fig. 3.25) [29].

3.4 Results and discussion

The observation of large CMR effect at low temperatures at and below T_p in the samples studied in the present work can be attributed to the inter-grain tunneling magnetoresistance. This observation can be explained on the basis of scattering of charge carriers at the interfaces of grain boundaries due to the application of magnetic field. It can be explained as an electron moving from initial grain to the next magnetic grain crosses two interfaces in its journey, each of which may behave as the scattering center [30]. This acts as an insulating barrier to the conduction of the carriers through the grains. Since A-site is occupied by different size cations, so unlike cations may occupy the positions at the faces of the adjacent grains [30, 31]. Hence, due to decrease in $<r_A>$ with Pr-Ca (x) concentration, the Mn environment changes at the interfaces of the connecting grains, which results in equal probability of weak and strong scattering of electrons at the interfaces. The strong scattering can be suppressed by the application of larger magnetic fields, to account for the larger drop in resistance as size disorder increases with x content [32].

The presently studied LPCMO system exhibits strong ferromagnetic behavior. The observation of magnetic anisotropy in higher (x) concentration is possibly due to the coexisting FM and AFM clusters. This coexistence of the mixed phases near the first order transition, results into the non-coincident T_p and T_C behavior [33]. The increasing Pr and Ca content increases the coexisting metal insulator phases and the carrier concentration. It can be interpreted from the magnetization measurements that, in the region where FM part prevails over the metallic one, separate FM droplets exist. The Zener double exchange is operative in these individual FM droplets but not across droplets, thus showing a small FM insulating region. The inhomogeneous cluster formation for different compositions shows lower T_p. At a certain temperature the individual ferromagnetic clusters coalesce into large aggregates resulting into I-M transition [31, 34]. The magnetotransport behavior is observed under 1 T field showing large CMR effect for all the Pr-Ca compositions. The low Curie temperature puts the presently studied system in the category of nearly low bandwidth system, which exhibits non-coincident electric and magnetic transitions [34].

3.5 Conclusion

In the present work, we have synthesized using solid state reaction route, the pure $LaMnO_3$ cation deficient sample and less cation deficient system like $La_{1-2x}Pr_xCa_xMnO_3$ (x = 0.10, 0.15) which have been optimized for long range ferromagnetic order in it, exhibiting I-M transition and appreciable MR behavior under low applied field.

The $La_{1-2x}Pr_xCa_xMnO_3$ (x = 0.20, 0.30) system of simultaneous doping of Pr and Ca showing high MR % under relatively low field 1 T.

References

1. J. M. D. Coey, M. Viret, Advances in Physics **48**, 2, 167 (1999)
2. J. Topfer, Jean-Pierre Doumerc and Jean-Claude Grenier, J. Mater. Chem. **6(9)**, 1511 (1996)
3. J. A. M. van Roosmalen and E.H. P. Cordfunke, J. Solid State Chem. **110**, 100 (1994)
4. J. Topfer and J. B. Goodenough, J. Solid State Chem. **130**, 117 (1997)
5. J. H. Kuo, H.U. Anderson and D.M. Sparlin, J. Solid State Chem. **52** (1989)
6. B. C. Toffield and W. R. Scott, J. Solid State Chem. **10**, 183 (1974)
7. R. Mahendiran, R. Mahesh, A.K. Raychaudhury and C.N.R. Rao, Pramana **44**, L393 (1995)
8. Anthony Arulraj, R. Mahesh, G.N. Subbanna, R. Mahendiran, A.K. Raychaudhury and C.N.R. Rao, J. Solid State Chem. **127**, 87 (1996)
9. C. Zener, Phys. Rev. **82**, 403 (1951)
10. E. O. Wollan and W. C. Kohler, Phys. Rev. **100**, 545 (1955)
11. M. Hervieu, R. Mahesh, N. Rangavittal and C.N.R. Rao, Eur. J. Solid State Inorg. Chem. **32**, 79 (1995)
12. G. H. Jonker and J. H. Van Santen, Physica **16**, 337 (1950)
13. V. I. Pavlov, A.K. Bogush, I.V. Balyko, Crystal Res & Technol **19**, 237 (1984)
14. Thesis R. Mahendiran, Department of Physics, IISC, Bangalore (1996)
16. Y. Tomioka, A. Azamitru, H. Kuwahona, Y. Morimoto and Y. Tokura, Phys. Rev. B, **53**, R1689 (1996)
17. Elbio Dagoito, Takashi Holta, Adrita Moreo, Physics Reports **344**, 1-153 (2001)
18. H Y Hwang, S-W Cheong, P G Radaelli, M Marezio and B Batlogg, Phys. Rev. Lett., **77**, 2041 (1996)
19. K Knizek, Z Jirak, E. Pollert, and F Zounova, J. Solid-state Chem. **100**, 292 (1992)
20. V. Kiryukhin, D. Caga, J. P. Hill, B. Kiemer, A. Vigliante, Y. Tomioka, Y. Tokura, Nature **586**, 813 (1997)
21. D. E. Cox, P. G. Radaelli, M. Marezio, Phys. Rev B **57**, 3305 (1998)

22. A P Ramirez, J. Phys: Condens. Matter **9**, 5171, (1997)

23. A. Maignan, C. Michel, M. Hervieu and B. Raveau, Solid State Comm. **101** (4), 277-281 (1997)

24. Ziese Michael, Srinitiwarawong Chatchai, Phys. Rev. B, **58,** 11519 (1998)

25. Coey J M D, Viret M, Ranno L, Ounadjela K, Phys. Rev. Lett., **75,** 3910 (1995)

26. Viret M, Ranno L, Coey J M D, J. Appl. Phys., **81,** 4964 (1997)

27. A. Gupta, Gong G. Q., Xiao Gang, Duncombe P. R., Lecoeur P., Trouilloud P., Wang Y. Y., Dravid V. P., & and Sun J. Z., Phys. Rev. B., **54**, 629 (1996)

28. Colossol Magnetoresistance, Charge Ordering and related properties of Manganese Oxides Ed. By. C.N.R. Rao, B. Raveau. World Scientific Publishing Co. Pte. Ltd. (1998)

29. Q. G. Gong, A. Gupta, Lecoeur P., Trouilloud P., Phys. Rev. B., **54**, R3742 (1996)

30. Hielman A K, Xue Y Y, Lorenz B, Campbell B J, Cmaidalka J, Wang R L, Chu C W, Phys. Rev.B, **65**, 214423 (2002)

31. X. W. Li, A. Gupta, G. Xiao, and G. Q. Gong, Appl. Phys. Lett. **71**, 1124 (1997)

32. Rodriguez-Martinez L M and Attfield J P, Phys. Rev. B, **54**, R15622 (1996)

33. R. Mahendiran, R. Mahesh, A. K. Raychaudhuri, C. N. R. Rao, Solid State Commun. **99**, 149 (1996)

34. J. M. D. Coey, *Philos.* Trans. R. Soc. London, Ser. A, **356**, 1539 (1998)

Chapter – IV

Introduction

The simultaneous substitution of Pr-Ca induces interesting properties in the resulting manganite system. The $La_{1-2x}Pr_xCa_xMnO_3$ in the previous chapter has been identified as a low bandwidth system exhibiting transition temperature below 120 K with significant CMR effect at relatively weaker fields [1, 2]. However, we have optimized this series with a sample to show that an optimal density $La_{0.5}Pr_{0.2}Ca_{0.3}MnO_3$ composition exhibit low T_p and T_C with a large MR%. In this chapter we have taken this sample as basis for the study of bandwidth modifications and cation size variance effect by Sr^{2+} and Ba^{2+} substitution on the electronic, magnetic and magnetotransport properties of the resulting system. In this endeavor, we have synthesized two series as $La_{0.5}Pr_{0.2}Ca_{0.3-x}Sr_xMnO_3$ (LPCSMO); x = 0.0-0.20 (0.05) and $La_{0.5}Pr_{0.2}Ca_{0.3-x}Ba_xMnO_3$ (LPCBMO); x = 0.0-0.30 (0.05). Lastly, we show that, increasing the cation size variance above a certain limit in $La_{0.4}Pr_{0.3}Ba_{0.3}MnO_3$ results in the phase-segregation indicative from the extra peaks of $BaMnO_3$ in the XRD spectrum. The conductivity in the semiconducting region is dominated by Mott's Variable Range Hopping type of conduction of polarons [3]. The structural, electrical, magnetic and magnetotransport properties have been studied using XRD, magnetoresistance and magnetic susceptibility measurements in the light of bandwidth modification and cation size disorder effects.

As mentioned earlier I-M & PM-FM transition temperatures, which are due to spin-polarized conduction of carriers through Zener-Double exchange depends upon the e_g electron bandwidth and carrier density [4]. $La_{0.7}Ca_{0.3}MnO_3$ (LCMO) and $Pr_{0.7}Ca_{0.3}MnO_3$ (PCMO) are intermediate and low bandwidth systems respectively. The dependence of transition temperature is ascribed to the amount of divalent cation doping and average A-site cation radius which is quantified by a tolerance factor, $t = \langle A\text{-}O\rangle/(\sqrt{2}\langle Mn\text{-}O\rangle)$.

L.M. Rodriguez-Martinez *et al* [5] defined a quantitative factor called size variance, $\sigma^2=\sum x_i r_i^2-\langle r_A\rangle^2$ - - - - (1), where x_i is the fractional occupancy of the cation with ionic radius r_i and $\langle r_A\rangle$ is the average A-site cation radius; characteristic of the mismatch of size of the different cations occupying A-site and studied its effect on the structural and transport behavior [5]. It is an established fact that, the optimal divalent cation doping of 33% in the absence of any cation size mismatch induces the largest possible concomitant electrical and magnetic transition temperatures. The effect of substitution of larger cation Sr^{2+} is interesting to observe the bandwidth modification and cation size mismatch effects. We have studied the $La_{0.5}Pr_{0.2}Ca_{0.3-x}Sr_xMnO_3$ (LPCSMO); x = 0.0-0.20 (0.05) and $La_{0.5}Pr_{0.2}Ca_{0.3-x}Ba_xMnO3$ (LPCBMO); x = 0.0-0.30 (0.05) systems with an aim to investigate the modifications in the transport and MR behavior with increasing bandwidth and size disorder.

4.1 Studies on $(La_{0.5}Pr_{0.2})(Ca_{0.3-x}Sr_x)MnO_3$ (LPCSMO)

x = 0.0-0.20 (0.05) series

4.1.1 Experimental details & structural studies

High purity La_2O_3, Pr_6O_{11}, $CaCO_3$, $SrCO_3$, $BaCO_3$ and MnO_2 powders were taken for synthesizing the thoroughly mixed and calcinated at 950ºC. All the samples were pelletized and sintered in the range of 1100-1400ºC with several intermittent grindings. A.c and d.c. susceptibility measurements were carried out for the magnetic susceptibility studies.

XRD measurements using Cu-K_α radiation were performed for the structural determination and phase purity. The Rietveld refinement program using FULLPROF program was employed. The refined XRD patterns of all the samples are given in figure 4.1, while figure 4.2 shows a typical Rietveld fitted pattern of x=0.15 sample.

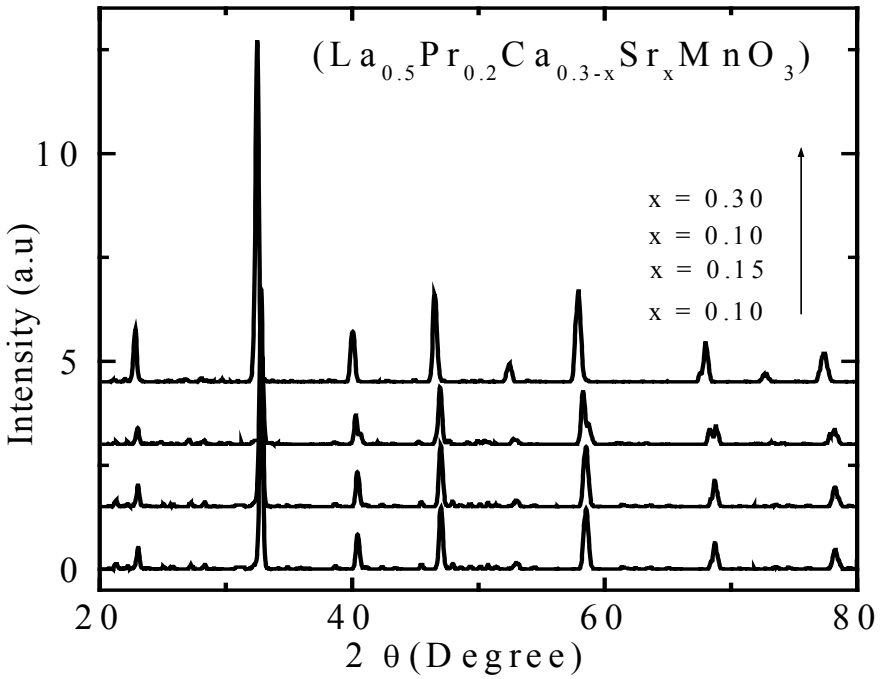

Figure 4.1: XRD pattern of the $La_{0.5}Pr_{0.2}Ca_{0.3-x}Sr_xMnO_3$ (x = 0.0 - 0.20)

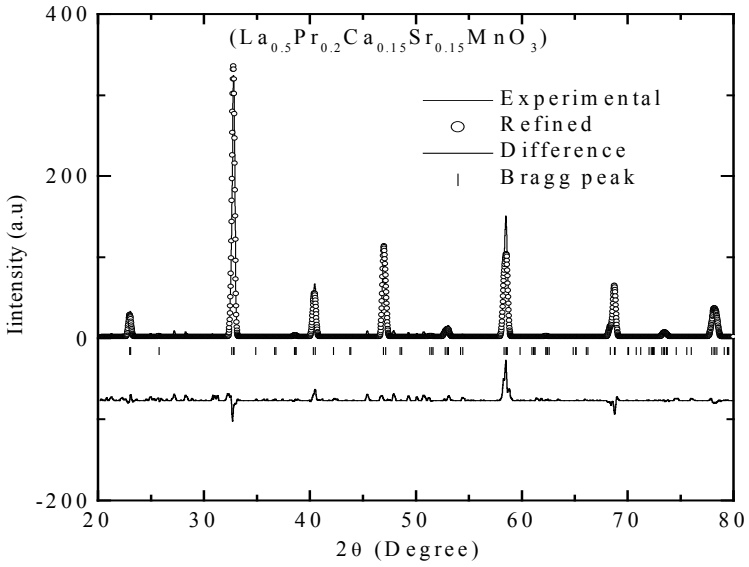

Figure 4.2: Rietveld fitted XRD pattern of the $La_{0.5}Pr_{0.2}Ca_{0.3-x}Sr_xMnO_3$ (x=0.15)

Rietveld refinement using FULPROOF program of all the samples for phase purity and structural investigations reveals a good phase formation with an impurity ~1-2% of mother

compounds for some of the samples. In this series all the samples fit to a distorted orthorhombic structure. The cell parameters and hence the volume increases with increasing Sr concentration, which can be attributed to larger size cation substitution effect. Table – 4.2 shows the variation of cell parameters, cell volume $<r_A>$ and σ^2 wih increasing x.

Table 4.1 : Structure, cell parameters and cell volume of $La_{0.5}Pr_{0.2}Ca_{0.3-x}Sr_xMnO_3$ ($0 \leq x \leq 0.20$) samples.

x	Structure	a (Å)	b (Å)	c (Å)	Volume(Å^3)
0	Orthorhombic (*Pnma*)	5.4576(1)	7.7224(2)	5.4436(2)	229.426
0.05	Orthorhombic (*Pnma*)	5.4482(1)	7.7295(1)	5.4633(1)	230.078
0.10	Orthorhombic (*Pnma*)	5.4559(2)	7.7145(1)	5.4774(2)	230.532
0.15	Orthorhombic (*Pnma*)	5.4859(1)	7.7145(2)	5.4592(1)	231.045
0.20	Orthorhombic (*Pnma*)	5.4995(2)	7.7165(1)	5.4613(2)	231.764

4.1.2 Electronic transport and magnetoresistance

Fig. 4.3 depicts the R-T and magneto R-T behaviour of LPCSMO samples in absence of magnetic field and in applied magnetic fields of 1 Tesla, 2 Tesla and 5 Tesla. The electrical transport behavior of the LPCSMO system, reveals that, as Sr^{2+} concentration increases, the transition temperature increases with a subsequent fall in resistivity, which has its origin in the modification of e_g electron bandwidth as the average A-site cation radius increases by Sr^{2+} substitution.

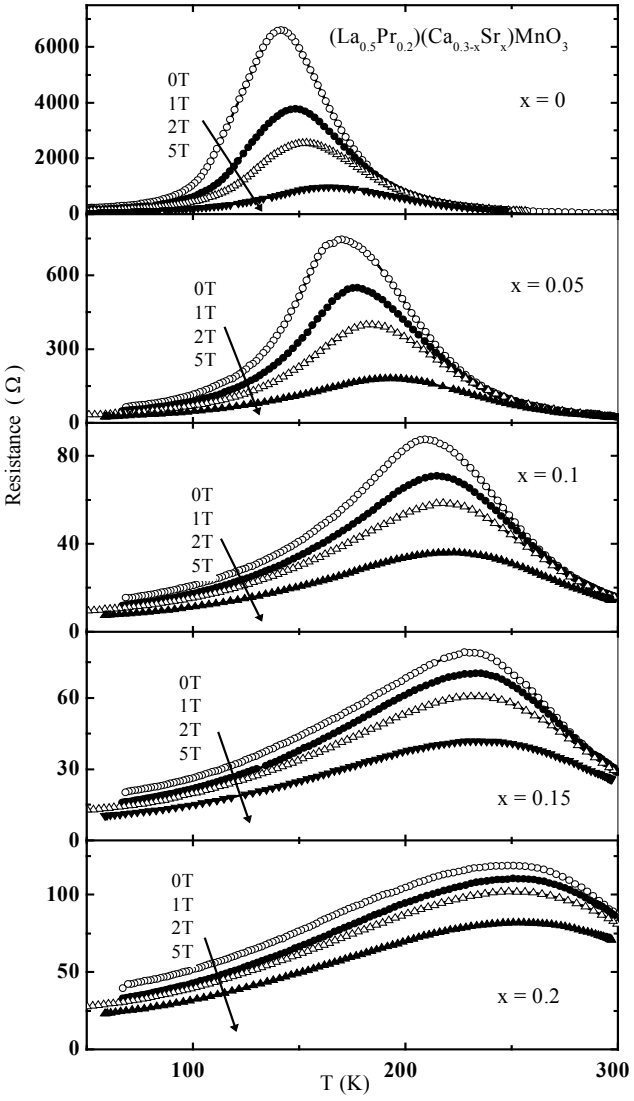

Figure: 4.3 R-T and magneto R-T plots for $La_{0.5}Pr_{0.2}Ca_{0.3-x}Sr_xMnO_3$; x = 0.0 - 0.20 (0.05) series.

In order to understand the conduction mechanism of polarons created as a result of electron-phonon coupling in the semiconducting region, we fitted the R-T data LPCSMO samples in figure 4.4, to nearest neighbor small polaron hopping model [6, 7] corresponding to $\rho = \rho_0 \exp(E_a/kT)$ and the Mott's type Variable Range Hopping model [8, 9] (VRH) corresponding $\rho = \rho_o \exp(T_o/T)^{1/4}$.

As shown in figures 3&4, the data fits linearly in lnρ vs. $T^{-0.25}$ plot, suggesting that, the conduction of the carriers in the semiconducting region obeys the Mott's Variable Range Hopping model. T_o in this equation is related to localization length by a relation,

$$kT_o = 18/L^2 N(E) \quad \text{- - - -} \quad (2)$$

where L is the localization length of the carriers and N(E) is the density of states.

It is observed from the magneto R-T measurements on Sr^{2+} substituted $La_{0.5}Pr_{0.2}Ca_{0.3-x}Sr_xMnO_3$ system (fig.2) that, T_p increases with increasing Sr content and a subsequent fall in MR%. The transition temperature is revived from 140 K to 247 K and CMR effect falls from 46% to 7% at a field of 1T with the 20% substitution of Sr^{2+}. Since the larger cation increases the Mn-O-Mn bond angle towards 180º and the fall in the magnetic disorder at the Mn-O couplings accounts for the low CMR effect [10]. Interestingly the CMR effect increases consistently at low temperature below transition temperature with increasing Sr content. This low temperature large CMR effect is due to the intergrain tunneling magnetoresistance [11]. The drop in the resistance in the higher magnetic field also increases with doping concentrations.

The magnetoresistance also occurs as result of the reduction of the scattering of the carriers at the interfaces due to application of magnetic field. The scattering of the carriers at the interfaces can be understood in the following way [12]. An electron moving from initial grain to the next magnetic grain crosses two interfaces in its journey, each of which may scatter the electron. This acts as an insulating barrier to the conduction of the carriers through the grains. Since A-site is occupied by different size cations, so unlike cations may occupy the positions at the faces of the adjacent grains. Hence, due to increasing size variance, the Mn environment varies at the interfaces of the connecting grains, which results in equal probability of weak and strong scattering of electrons at the interfaces. The

strong scattering can be suppressed by the application of larger magnetic fields, to account for the larger drop in resistance as size disorder increases with Sr content. Another notable factor is that, the trend in the increase in T_C is not linear with Sr concentration, being larger for lower compositions and smaller for higher Sr content. This leads to deviation in the ideal relationship of Tc and tolerance factor [4].

It can be explained by the mismatch of the cations at A-site, which increases with Sr content. The large size variance, as calculated from equation, $\sigma^2 = \sum x_i r_i^2 - < r_A >^2$, induces the strain in the lattice by random displacement of oxygen ions and hence obstructs the Zener-Double exchange.

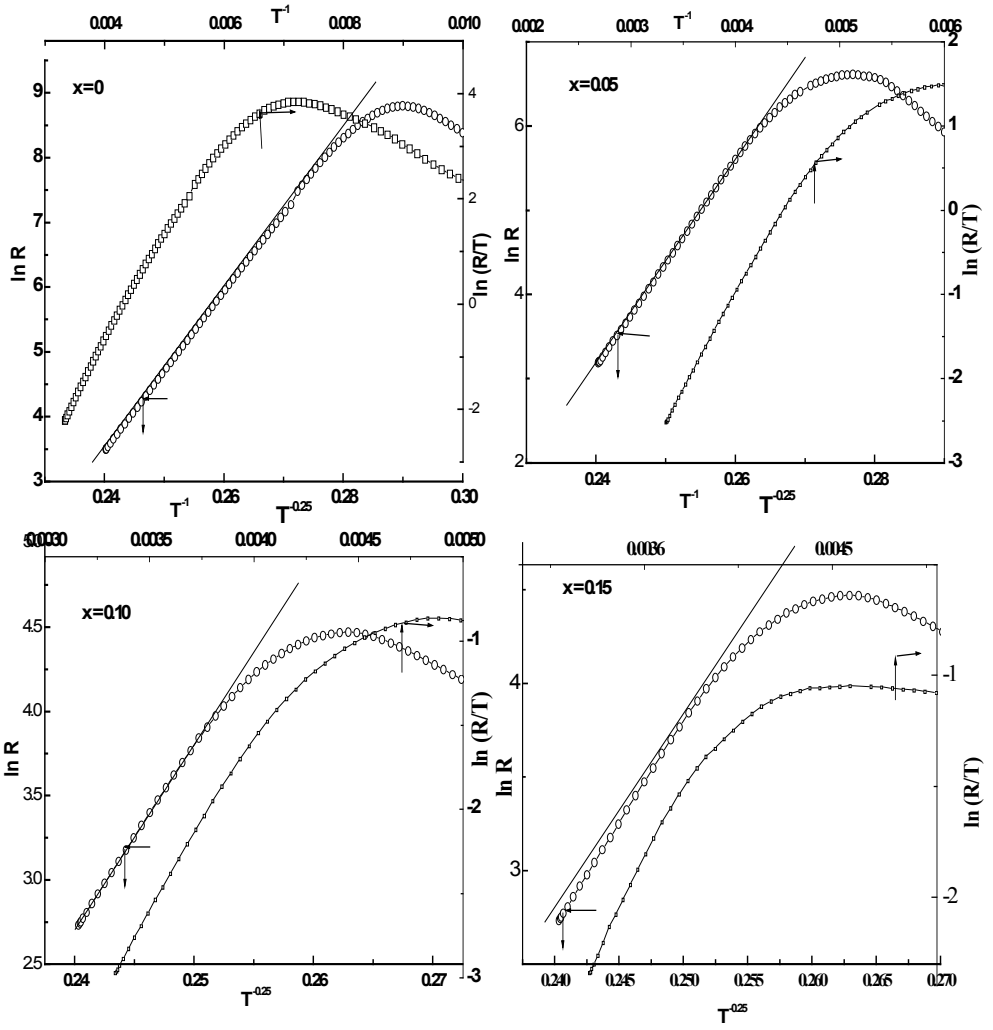

Figure 4.4: Mott's VRH model (ln R vs $T^{-0.25}$) and small polaron model (ln (R/T) vs T^{-1}) fits for $La_{0.5}Pr_{0.2}Ca_{0.3-x}Sr_xMnO_3$; x = 0.0 - 0.15 (0.05) series.

The fitting of the electrical transport data in the semiconducting region reveals that conduction in this region occurs through the Mott's Variable Range hopping of polarons. CMR effect is found to have an inverse relationship with the transition temperature. The A-site disorder increases with Sr concentration and leads to microscopic inhomogenieties in the samples through the random displacement of oxygen anion and showing its influence on the electrical, magnetic and magnetotransport properties.

4.1.3 Magnetization

The magnetic susceptibility plots for LPCSMO samples (fig. 4.5) shows an increasing trend in Curie temperature with increasing Sr content. It is inferred that the magnetic irreversibility decreases with increasing transition temperature.

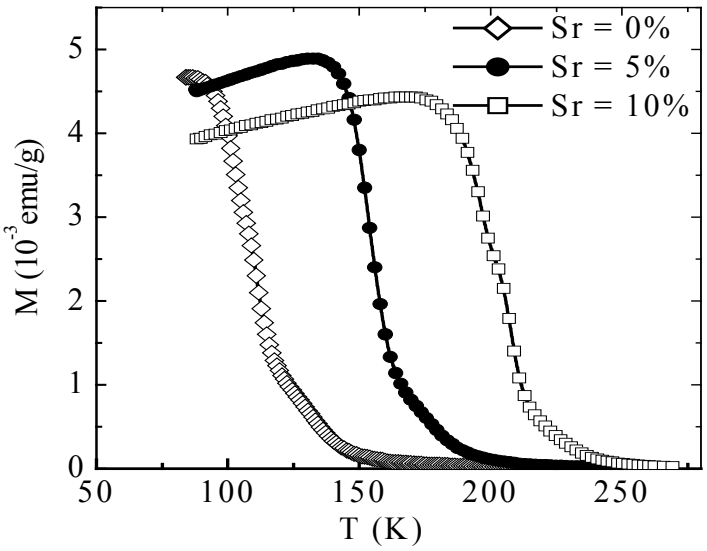

Figure 4.5: Magnetic susceptibility vs Temperature plots for $La_{0.5}Pr_{0.2}Ca_{0.3-x}Sr_xMnO_3$ series.

4.2. Studies on $(La_{0.5}Pr_{0.2})(Ca_{0.3-x}Ba_x)MnO_3$ (LPCBMO) ($0.05 \leq x \leq 0.3$)

In addition to Sr^{2+}, Ba^{2+} is another divalent cation which is interesting for substitution at A-site due to two reasons, namely, 1) due to its larger size (~1.47Å) it enhances the tolerance factor significantly and 2) due to large mismatch with size of the other cations at A-site, it increases the A-site size-disorder. As mentioned earlier, the increasing size disorder increasing the intrinsic inhomogenieties, which may affect the transport, magnetic and magnetotransport properties of the resulting compounds. As shown in the previous section, the $La_{0.5}Pr_{0.2}Ca_{0.3}MnO_3$ is a suitable system for

substitutional studies aiming to elucidate the effect of tolerance factor and size-variance. Keeping this in mind, we have replaced the smaller size divalent cation, Ca^{2+}, by a larger size cation, Ba^{2+}, in the system $(La_{0.5}Pr_{0.2})(Ca_{0.3-x}Ba_x)MnO_3$ ($0.05 \leq x \leq 0.3$) and studied the ionic size and size disorder effect on the structural, transport and magnetic properties. In this series, the size-disorder increases from $0.0001 Å^2$ for x=0 to $0.016 Å^2$. Such a large variation of size-disorder across the series makes all these compounds, an interesting subject of investigations. Other than this series of compounds, we have also tried to synthesize the compound, $La_{0.4}Pr_{0.3}Ba_{0.3}MnO_3$, which possesses the largest size-disorder among all the compounds studied in this section. In the $La_{0.4}Pr_{0.3}Ba_{0.3}MnO_3$ manganite sample, we find the chemical phase-segregation, resulting in secondary phase [14]. The various structural, transport, magnetotransport and magnetic properties are collated in the following sections.

4.2.1 Experimental details

All the $(La_{0.5}Pr_{0.2})(Ca_{0.3-x}Ba_x)MnO_3$ ($0.05 \leq x \leq 0.3$) and $La_{0.4}Pr_{0.3}Ba_{0.3}MnO_3$ compounds were synthesized using conventional solid-state reaction route. Constituent oxides (La_2O_3, Pr_6O_{11}, and MnO_2) and carbonates ($SrCO_3$ and $CaCO_3$) were mixed thoroughly in stoichiometric proportions and calcined at 950°C for 24 hours. These were ground, pelletized and sintered in the temperature range of 1100°C - 1200°C for 100 hours with many intermediate grindings. The final sintering was carried out at 1300°C for 24 hours. X-ray diffraction (XRD) patterns were recorded in the 2θ range of $20^o - 80^o$ on a Siemens diffractometer. Magnetization measurements were performed using a SQUID magnetometer (MPMS XL, Quantum Design). The resistivity and magnetoresistance measurements were carried using d.c. four probe method on a physical property measurement system (PPMS, Quantum Design).

4.2.2 Structural Studies

The XRD patterns of all the $(La_{0.5}Pr_{0.2})(Ca_{0.3-x}Ba_x)MnO_3$ $(0.05 \leq x \leq 0.3)$ (to be referred as LPCBMO) samples were indexed to be single phase compounds crystallizing in a distorted orthorhombic structure. Rietveld refinement technique using FULLPROF software was employed to obtain to refined cell parameters. Figure 4.6 shows the XRD patterns of all the samples while figure 4.7 displays a typical Rietveld refined XRD pattern of x=0.2 and $La_{0.4}Pr_{0.3}Ba_{0.3}MnO_3$ (LPBMO) samples. It is seen that there is an excellent agreement of experimental and fitted patterns of x=0.20 sample and is, therefore, single-phase compound. However, when LPBMO fitted to orthorhombic structure shows some additional peaks in the structure indicated by (*), presumably of $BaMnO_3$ [6]. This sample has maximum A-site size-disorder and may be the cause of the structural phase segregation. This shows that, above a certain critical limit of A-site size-disorder, it exert a structural strain and results in phase-segregation. Table – 4.2 shows the variation of cell parameters, cell volume $\langle r_A \rangle$ and σ^2 with increasing x.

Table 4.2: Structure, cell parameters and cell volume of $(La_{0.5}Pr_{0.2})(Ca_{0.3-x}Ba_x)MnO_3$ $(0.05 \leq x \leq 0.3)$ samples.

$(La_{0.5}Pr_{0.2})(Ca_{0.3-x}Ba_x)MnO_3$ $(0.05 \leq x \leq 0.3)$	a (Å)	b (Å)	c (Å)	Cell Volume
X=0.05	5.46603(2)	7.72868(2)	5.47161(2)	231.149
X=0.10	5.47066(2)	7.73082(2)	5.49513(2)	232.404
X=0.15	5.47913(2)	7.7416(2)	5.51209(2)	233.808
X=0.20	5.48911(2)	7.75494(2)	5.52533(2)	235.201
X=0.25	5.49859(2)	7.76887(2)	5.48911(2)	236.439
X=0.3	5.51182(2)	7.79095(2)	5.54783(2)	238.237

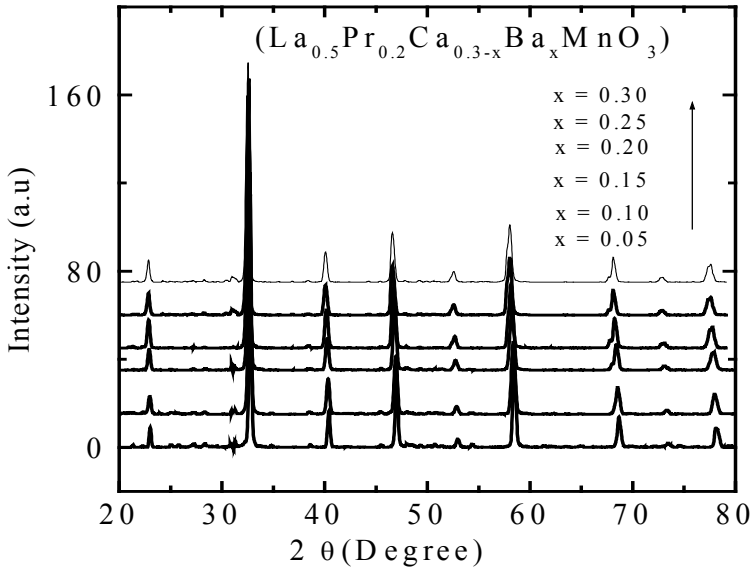

Figure 4.7: XRD patterns of the $(La_{0.5}Pr_{0.2})(Ca_{0.3-x}Ba_x)MnO_3$ ($0.05 \leq x \leq 0.3$) sample

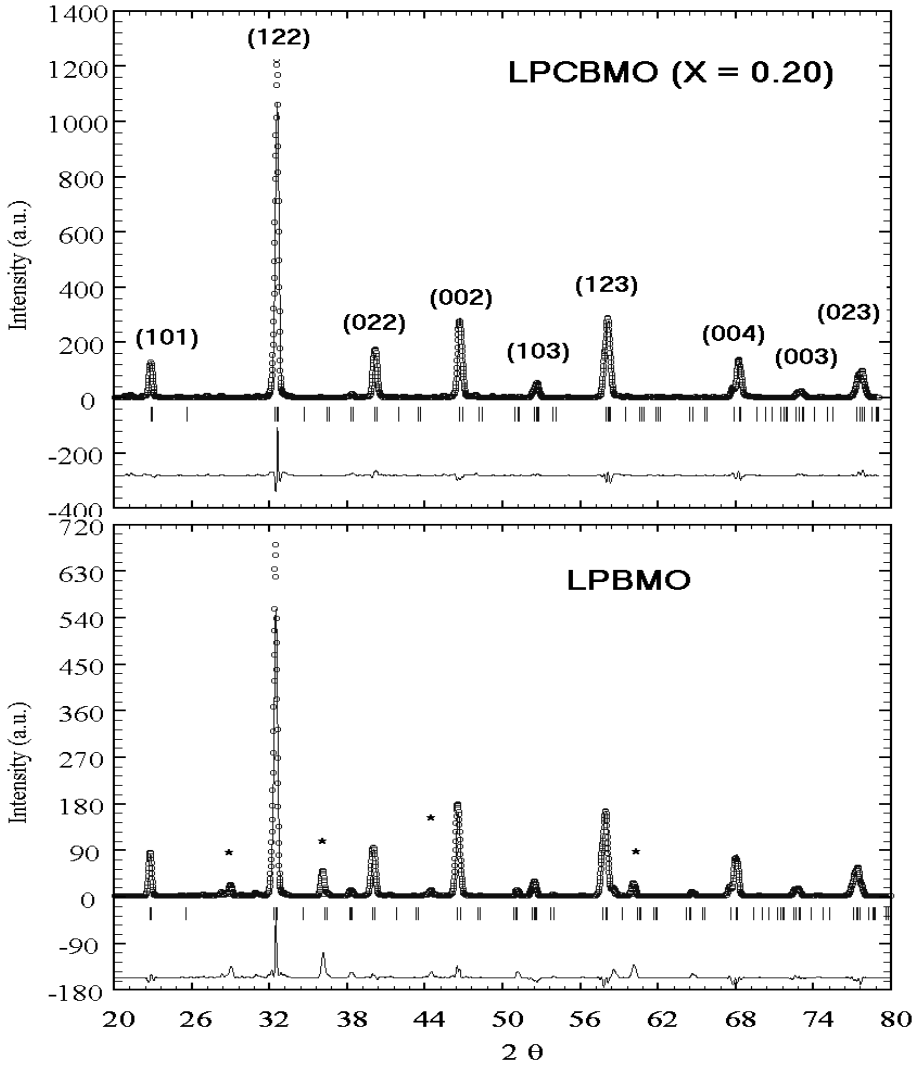

Figure 4.8: Rietveld fitted patterns of $(La_{0.5}Pr_{0.2})(Ca_{0.3-x}Ba_x)MnO_3$ (x=0.20) and $La_{0.4}Pr_{0.3}Ba_{0.3}MnO_3$ samples. The asterisks in the fitted patterns of LPBMO sample (Lower panel) depict the secondary phase of $BaMnO_3$.

4.2.3 Electrical Resistivity

The plots of electrical resistivity as a function of temperature for all the $(La_{0.5}Pr_{0.2})(Ca_{0.3-x}Ba_x)MnO_3$ ($0.05 \leq x \leq 0.3$) in zero field and in a fields of 5T and 9T over a temperature range of 5 K-320 K. The plots are shown in figs. 4.9 and 4.10.

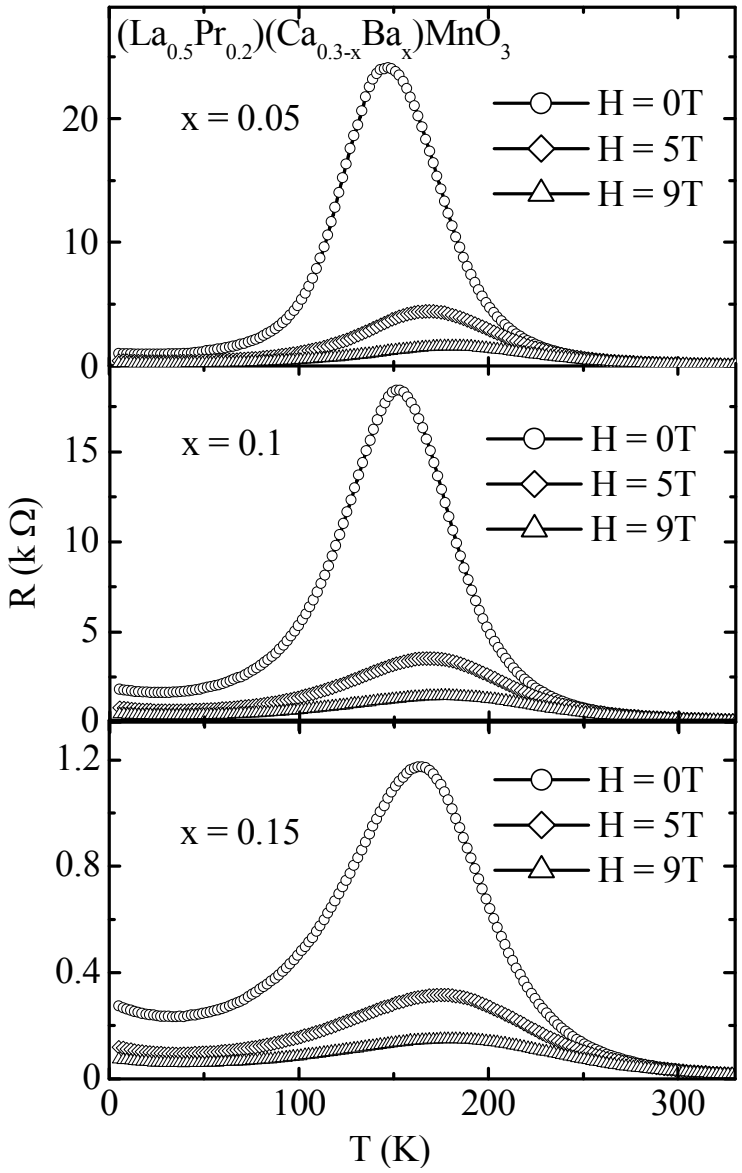

Figure 4.9: Resistivity as a function of temperature in 0T, 5T and 9T in a temperature range of 5 K-320 K for $(La_{0.5}Pr_{0.2})(Ca_{0.3-x}Ba_x)MnO_3$ ($0.05 \leq x \leq 0.15$) samples.

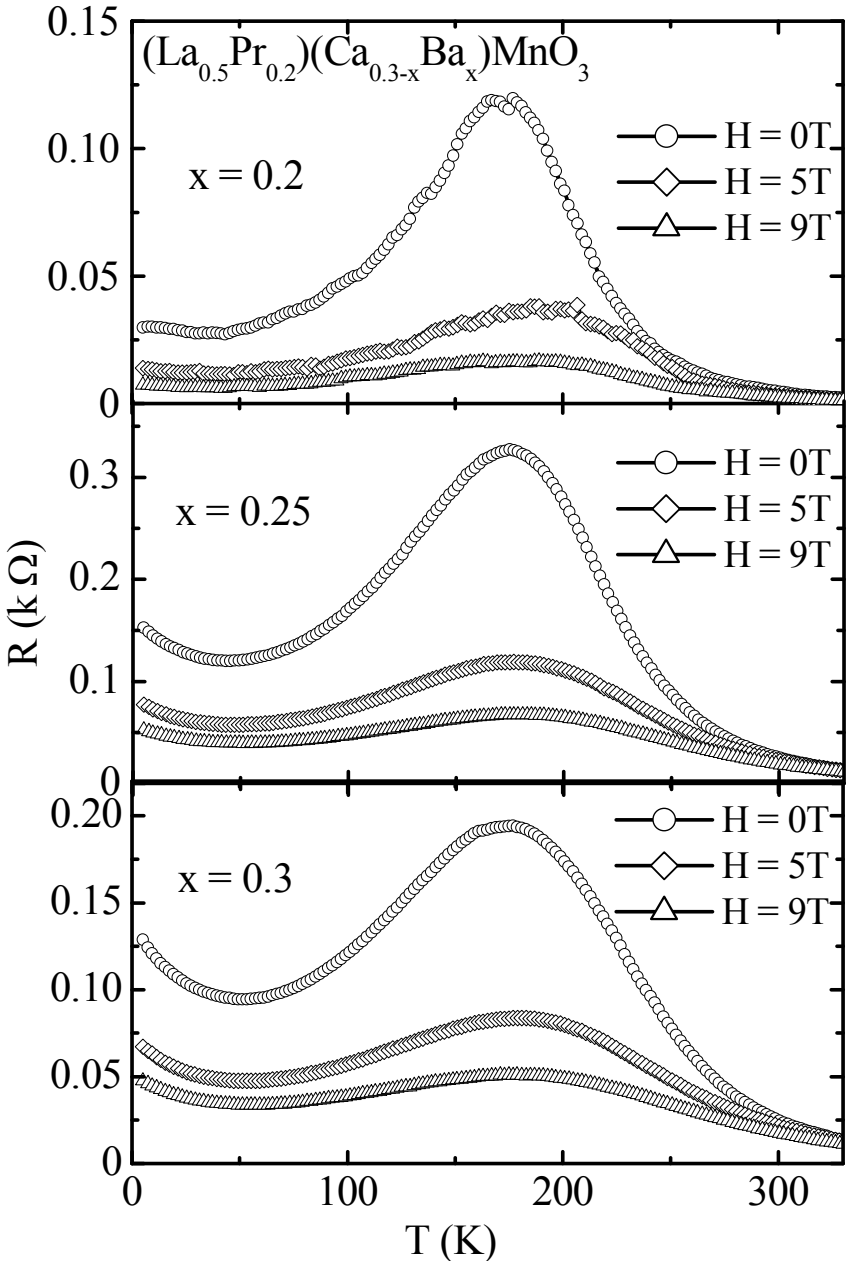

Figure 4.10: Resistivity as a function of temperature in 0T, 5T and 9T in a temperature range of 5 K-320 K for $(La_{0.5}Pr_{0.2})(Ca_{0.3-x}Ba_x)MnO_3$ ($0.20 \leq x \leq 0.30$) samples.

It is seen in figs. 4.9 & 4.10 that all the $(La_{0.5}Pr_{0.2})(Ca_{0.3-x}Ba_x)MnO_3$ ($0.05 \leq x \leq 0.30$) samples exhibit insulator-metal transition. The I-M transition temperature, T_p, increases from ~145 K for x=0.05 sample to ~175 K for x=0.30 sample. This enhancement in T_p may be understood on the basis increase in tolerance factor with increasing Ba^{2+} content.

Progressive substitution of Ba^{2+} (1.47Å) at Ca^{2+} (1.18Å) induces a large increase in average A-site cation radius and hence the tolerance factor increases to a larger extent.

4.2.4 Magnetization measurements

The temperature dependence of magnetization measurements for all the samples were performed in zero-field-cooled (ZFC) and field-cooled (FC) manner. This implies that sample is cooled in zero-field (ZFC) to the lowest temperature and then a certain field is applied for measuring the magnetization of the sample in warming direction. After this temperature of magnetization, the sample is cooled in the same magnetic field (FC) to the lowest temperature and then measured the magnetization while warming. The ZFC and FC magnetization versus temperature for all the $(La_{0.5}Pr_{0.2})(Ca_{0.3-x}Ba_x)MnO_3$ $(0.05 \leq x \leq 0.30)$ samples is shown in fig. 4.11.

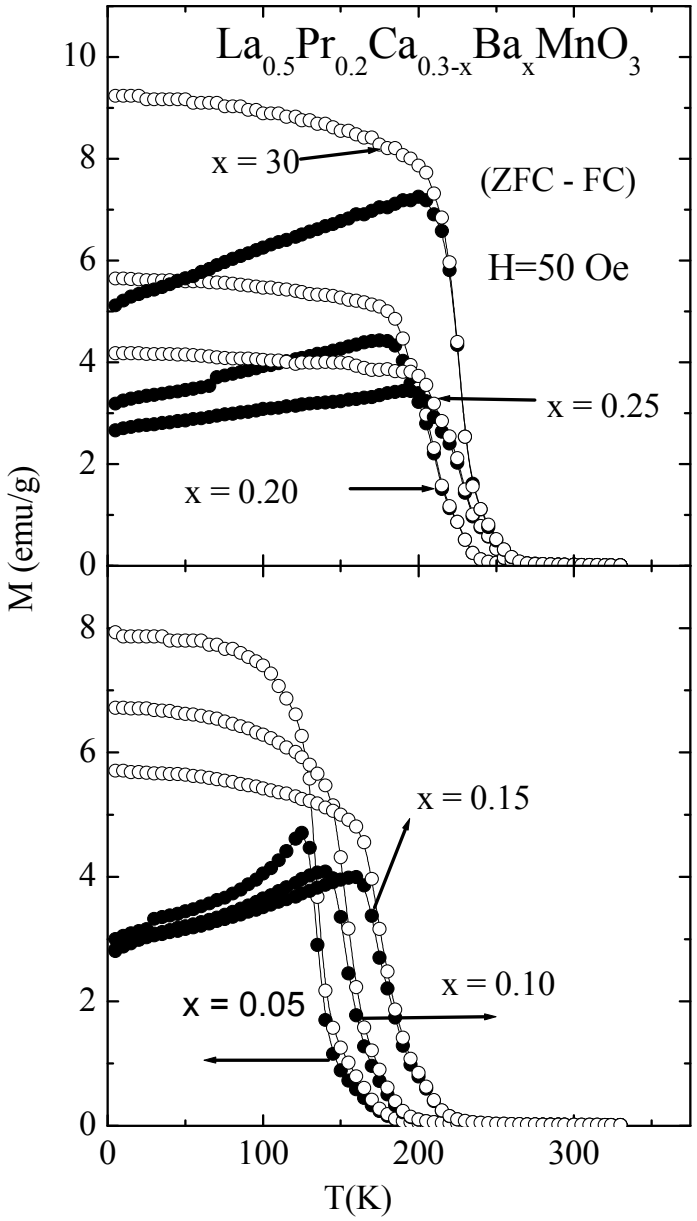

Figure 4.11: Zero-field-cooled (ZFC) and field-cooled (FC) magnetization (M) as a function of temperature for $(La_{0.5}Pr_{0.2})(Ca_{0.3-x}Ba_x)MnO_3$ samples in a field of 50 Oe.

The Curie temperature (T_C) increases from 150K for x=0.05 to 220K for x=0.30. With increasing Ba-substitution, the increasing trend of T_C is similar to increasing trend of the insulator-metal transition temperature (T_p). However, it is seen that the T_C and T_p of

these samples do not match with each other and this disparity increases with increasing Ba-concentration. This disparity is not in accordance with the Zener-Double-Exchange interactions and can be explained on the purview of possible grain boundary localization or phase separation. It is needless to mention that the polycrystalline samples of various micron sized grains, in which properties may vary inside the grain and on the grain boundaries. As the ZDE come into play, the bulk part of the grain become ferromagnetic and metallic while the grain boundaries are still insulating. The grain boundaries may be insulating because of the grain boundary pinning of Mn-ion spins, poor connectivity and grain boundary contamination [15]. This creates the insulating channels at the grain boundaries and does not allow the percolation of the charge carriers and results in insulating behavior even after the onset of T_C. Once the grain boundaries become conducting at lower temperatures, the I-M transitions appear. Other factor that can cause a disparity between T_p and T_C is the phase-separation as explained in [16]. Due to the granular mixture of different electronic densities, the T_C of different grains could be different. For instance, we assume that majority of the grains have large electronic density so that they exhibit T_C at higher temperatures, while the remaining minor fraction have lower T_C. Now, at the onset of the T_C of majority of grains (with higher T_C), the systems tends to be ferromagnetic even as a minority of grain are still paramagnetic-insulating. In such as a situation, though the system will be ferromagnetic, it will continue to exhibit semiconducting/insulating behavior unless all the grains become ferromagnetic. At a certain temperature when the whole system attains ferromagnetism, percolation is possible and the system exhibits I-M transition. The disparity in T_C and T_p in the present system may be because of either or both of the above stated causes. We get an evidence of the phase separation from the d.c. magnetic susceptibility.

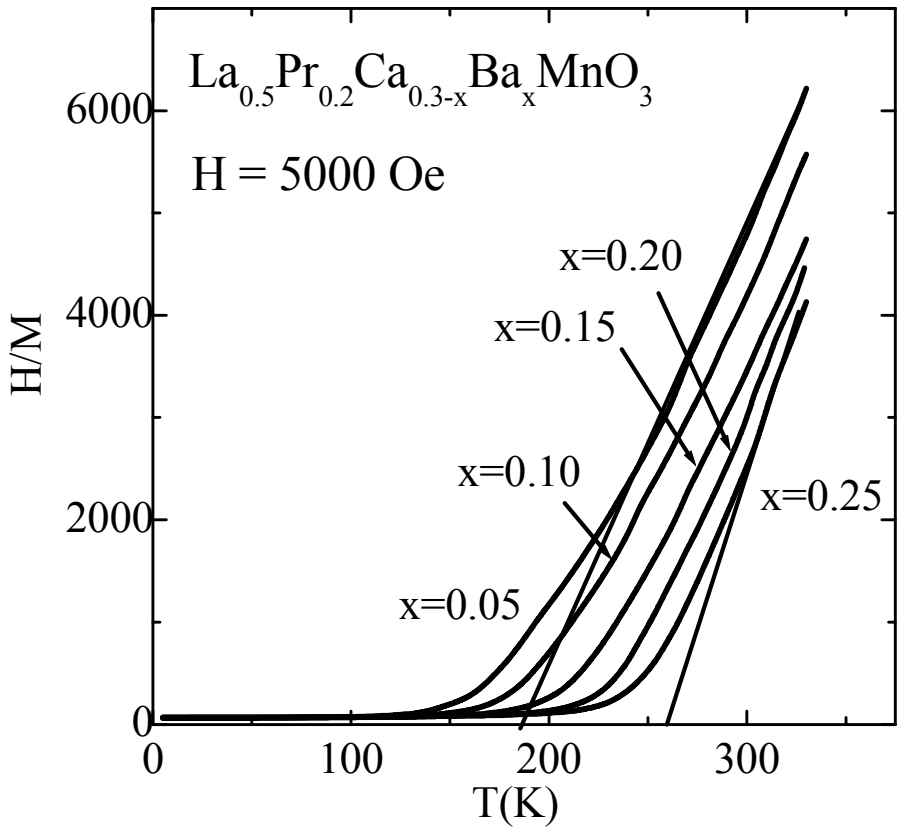

Figure 4.12: Inverse susceptibility (H/M at H = 5 kOe) as a function of temperature for $(La_{0.5}Pr_{0.2})(Ca_{0.3-x}Ba_x)MnO_3$ samples.

Fig. 4.12 shows the inverse susceptibility as a function of temperature for the $(La_{0.5}Pr_{0.2})(Ca_{0.3-x}Ba_x)MnO_3$ ($0.05 \leq x \leq 0.25$) samples when magnetization is acquired in a field of 5kOe. It is seen that there exists a deviation of Curie-Weiss law from the paramagnetic susceptibility of all the samples. This indicates towards the magnetic inhomogeneities or possible existence of ferromagnetic clusters in the paramagnetic region. Such inhomogeneities, which may be present both in paramagnetic and

ferromagnetic regions, suggesting that phase separation could be one cause of disparity of T_C and T_p in these samples.

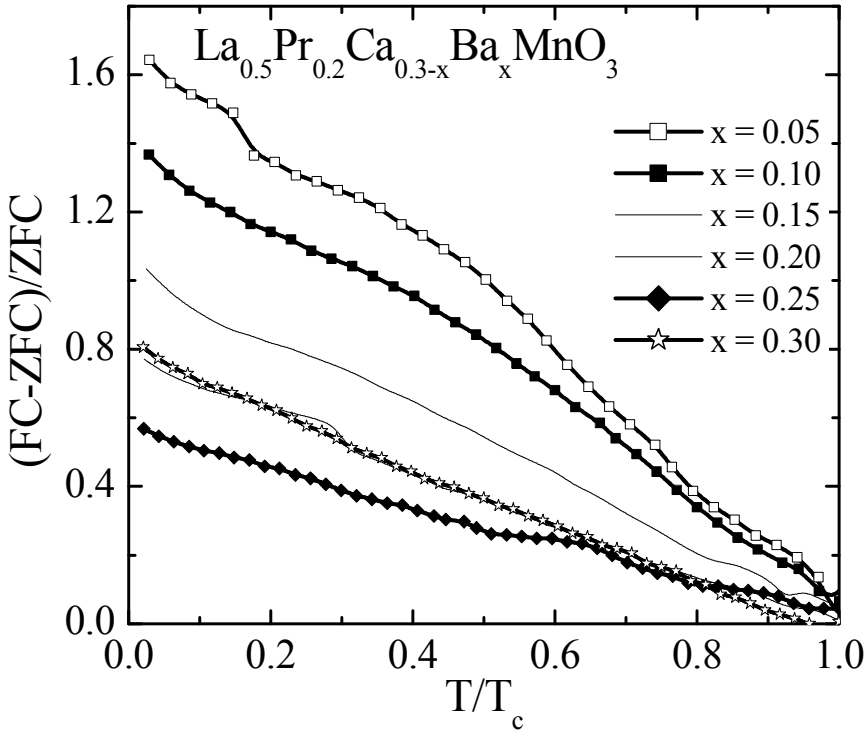

Figure 4.13: Fractional change of magnetization (M_{FC}-M_{ZFC}/M_{ZFC}) versus temperature (T) for all the $(La_{0.5}Pr_{0.2})(Ca_{0.3-x}Ba_x)MnO_3$ samples.

On the other hand, we evidence a large bifurcation of ZFC and FC magnetization curves for all the samples. To quantify this separation, we have plotted a quantity called fraction change in magnetization (M_{FC}-M_{ZFC}/M_{ZFC}) as a function of normalized temperature (T/T_C) in figure 4.13. As seen in this figure that (M_{FC}-M_{ZFC}/M_{ZFC}) decreases as function of increasing Ba^{2+} concentration. The x=0.30 sample does not follow this trend because this sample was prepared in a different batch with a slightly different synthesis route. Also, it is mentioned that generally a bifurcation of M_{ZFC} and M_{FC} arises from grain boundary pinning. In the samples under present study, the a large bifurcation of the two curves in all these Ba^{2+} substituted samples suggests enhanced grain boundary pinning

and, thus, the grain boundary localization [13]. Therefore, this factor is also likely to play a role in the disparity of T_p and T_C of these samples. Thus, by providing experimental evidence of phase-separation and grain boundary localization, we show that these factors cause the I-M transition to occur at lower temperatures than T_C.

4.2.5 Magnetoresistance measurements

The resistance was measured as a function of applied magnetic field at various temperatures for all $(La_{0.5}Pr_{0.2})(Ca_{0.3-x}Ba_x)MnO_3$ ($0.05 \leq x \leq 0.30$) samples. From these data magnetoresistance was calculated using the formula $MR(\%)=\{(\rho_0-\rho_H)/\rho_0\}\times 100$ and the plots of magnetoresistance versus magnetic field isotherms are shown in figs. 4.14 & 4.15. It may be seen that all the samples exhibit maximum MR in the vicinity of their respective I-M transition temperatures. Maximum MR in the vicinity of T_p may be explained on the basis of field induced suppression of spin fluctuation. At the I-M transition, there exists maximum magnetic disorder and magnetic field enhances the ferromagnetic spin ordering. On the other hand, at low temperature we observe two features in MR. One, a large MR of nearly 20% in a low field of 0.5-1 Tesla and other, a low MR at higher fields. Here, a large low-field MR arises from the inter-grain spin-polarized tunneling while a low high-field MR is also because of almost complete spin-polarization at low temperatures.

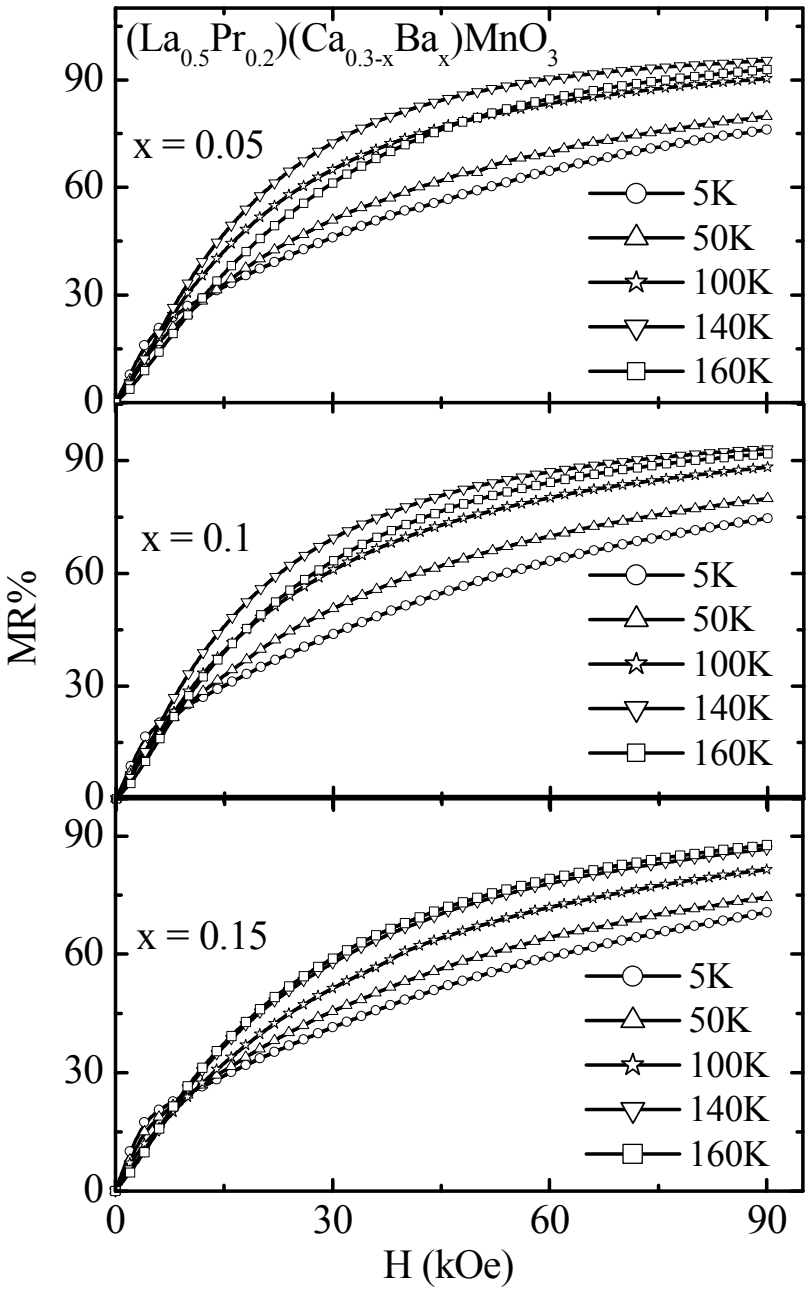

Figure 4.14: Magnetoresistance (MR%) as a function of magnetic field (H) at various temperatures for $(La_{0.5}Pr_{0.2})(Ca_{0.3-x}Ba_x)MnO_3$ ($0.05 \leq x \leq 0.15$) samples.

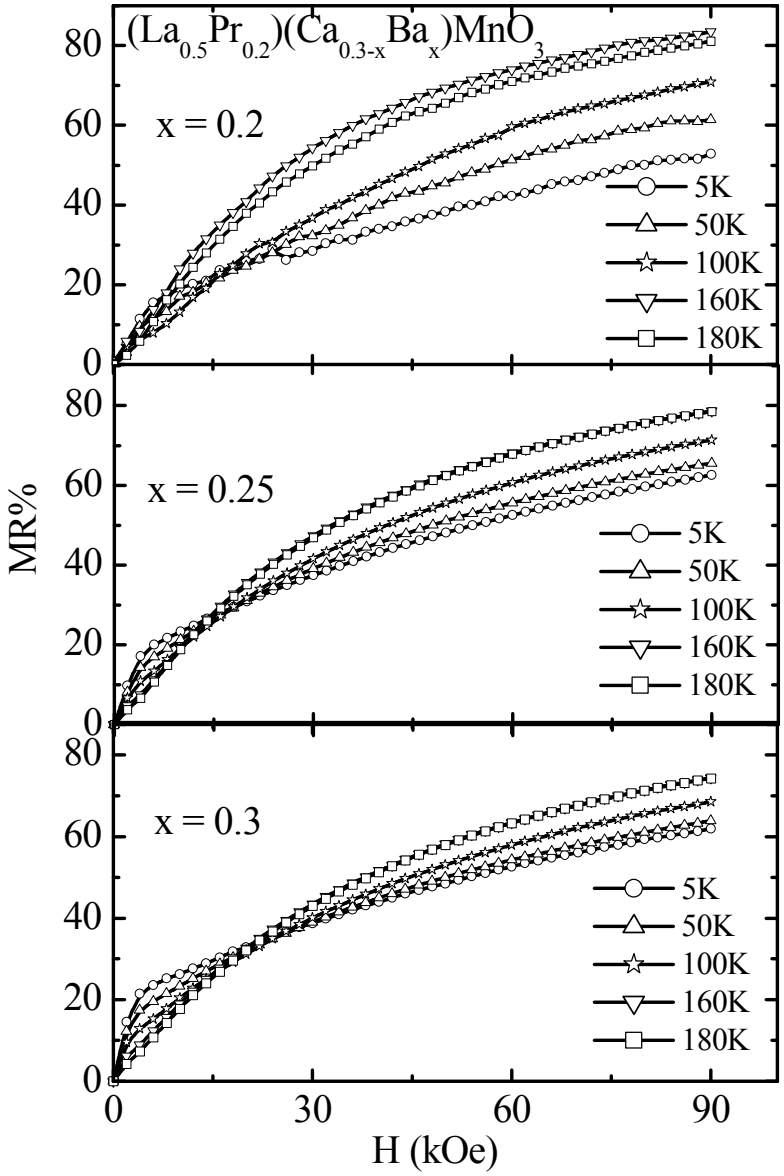

Figure: 4.15 Magnetoresistance (MR%) as a function of magnetic field (H) at various temperatures for $(La_{0.5}Pr_{0.2})(Ca_{0.3-x}Ba_x)MnO_3$ ($0.20 \leq x \leq 0.30$) samples.

In figs. 4.14 & 4.15, we observe that at lower Ba^{2+} substitution, the maximum MR of ~95% for x=0.05 decreases to a maximum of ~75% for x=0.30 sample in the vicinity of their respective I-M transition temperatures. As the temperature decreases below the I-M

transition temperature, the MR starts decreasing. Interestingly, we see two clear trends in MR with decreasing temperature and increasing Ba^{2+} concentration. As the temperature goes below 50K [17], we observe an enhancement in MR in low-fields while the MR in high-fields decreases. Also, it is seen that the low field MR at low temperatures increases with increasing Ba^{2+} content. This trend may be explained as follows [17, 18, 19]. As Ba^{2+} content increases, the increase in T_C suggests that the spin polarization will increase at low temperatures. The enhanced spin polarization will result in larger spin-polarized inter-grain tunneling on the application of small fields. Hence, we observe increasing low-field MR as the T_C increases with increasing Ba^{2+} concentration. The high field MR at low temperatures occurs due to magnetic disorder at Mn-O-Mn bonds (due to Zener-Double-Exchange) and pinning of Mn-ion spins at the grain boundaries. As stated above the spin polarization increases and, hence, the spin magnetic disorder decreases at the Mn-O-Mn bonds, which results in a low high-field MR as the T_C increases.

4.3 Comparative study of $La_{0.5}Pr_{0.2}Ca_{0.3-x}Sr_xMnO_3$ (LPCSMO); x = 0.0-0.30 (0.05) and $La_{0.5}Pr_{0.2}Ca_{0.3-x}Ba_xMnO_3$ (LPCBMO); x = 0.0-0.30 (0.05)

The substitution of Sr^{2+}(~1.31 Å) and Ba^{2+}(~1.47 Å) in $La_{0.5}Pr_{0.2}Ca_{0.3}MnO_3$ results in the LPCSMO and LPCBMO series, which have mixed impact of tolerance factor and size-disorder on the transport and magnetic and magnetotransport properties. Here we compare some of the properties of these two series. In both LPCSMO and LPBMO series, the tolerance factor and size-disorder increases with increasing substitution of Sr^{2+} and Ba^{2+} respectively. The respective increase in average A-site cation radius ($<r_A>$, which represents the tolerance factor) and A-site cation disorder in both the series is depicted in Fig. 4.16.

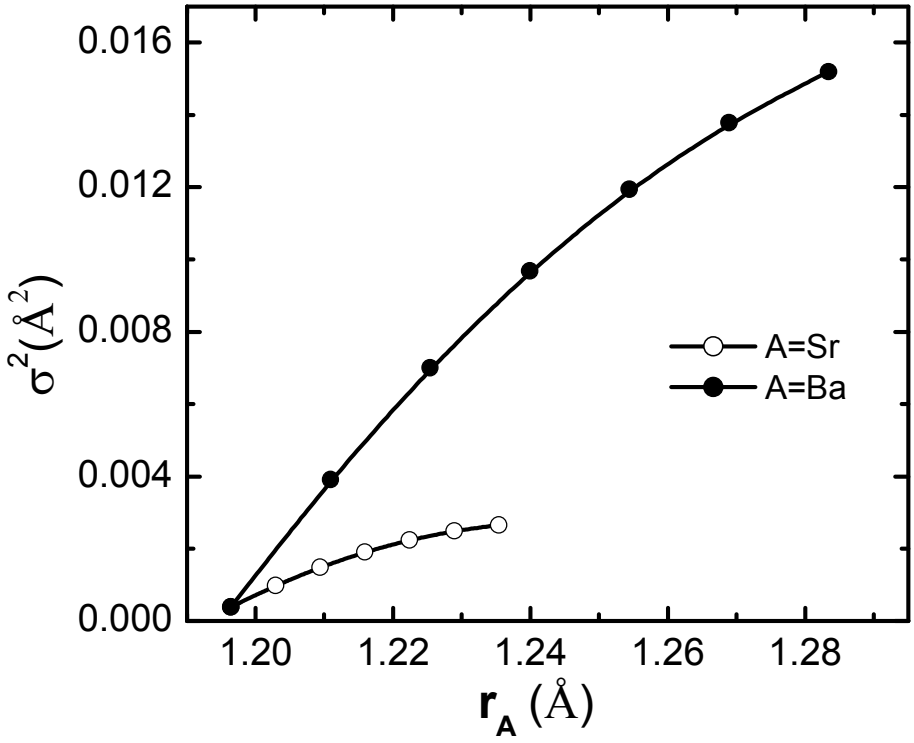

Figure 4.16: Variation of A-site cation size-disorder as a function of $\langle r_A \rangle$ for both the LPCSMO and LPCBMO series.

It is seen from Fig. 4.16 that the increase in σ^2 with increasing $\langle r_A \rangle$ is too large in LPCBMO as compared to that in LPCSMO series. However, in spite of large $\langle r_A \rangle$ (and, therefore, the tolerance factor) of LPBMO series, its electronic and magnetic transition temperatures are lower as compared to LPCSMO series. Table-4.3 lists, for comparison, values of various structural parameters and electronic transition temperatures of these two series.

Table – 4.3: Average A-site cation radius ($<r_A>$), size-disorder (σ^2) and insulator-metal transition temperature (T_p) for $(La_{0.5}Pr_{0.2})(Ca_{0.3-x}A_x)MnO_3$ (A=Sr and Ba).

x	$<r_A>$ (Å) A= Ba(Sr)	σ^2 (Å^2) A=Ba(Sr)	T_p (K) A=Ba(Sr)
0.0	1.196(1.196)	0.00039(0.00039)	140(140)
0.05	1.211(1.203)	0.00391(0.00098)	145(170)
0.10	1.225(1.209)	0.00701(0.00149)	150(205)
0.15	1.239(1.216)	0.00969(0.00191)	164(230)
0.20	1.254(1.222)	0.01195(0.00224)	171(260)
0.25	1.269(1.228)	0.01378(0.00249)	172(----)
0.30	1.284(1.235)	0.0152(0.00266)	175(313)

Similarly, we find a variation in I-M transition temperatures (T_p) as a function of varying size variance (σ^2) for pair of samples of the two series with constant $<r_A>$. Figure 4.17 shows the T_c vs size variance plots for a fixed average A-site ionic radius for $La_{0.5}Pr_{0.2}Ca_{0.3-x}A_xMnO_3$, A = Ba & Sr. For $<r_A>$ =1.21 Å, Ba = 0.05 and Sr = 0.10; for $<r_A>$ = 1.22Å, Ba = 0.10, Sr = 0.20 and for $<r_A>$ = 1.23Å, Ba = 0.15, Sr = 0.30.

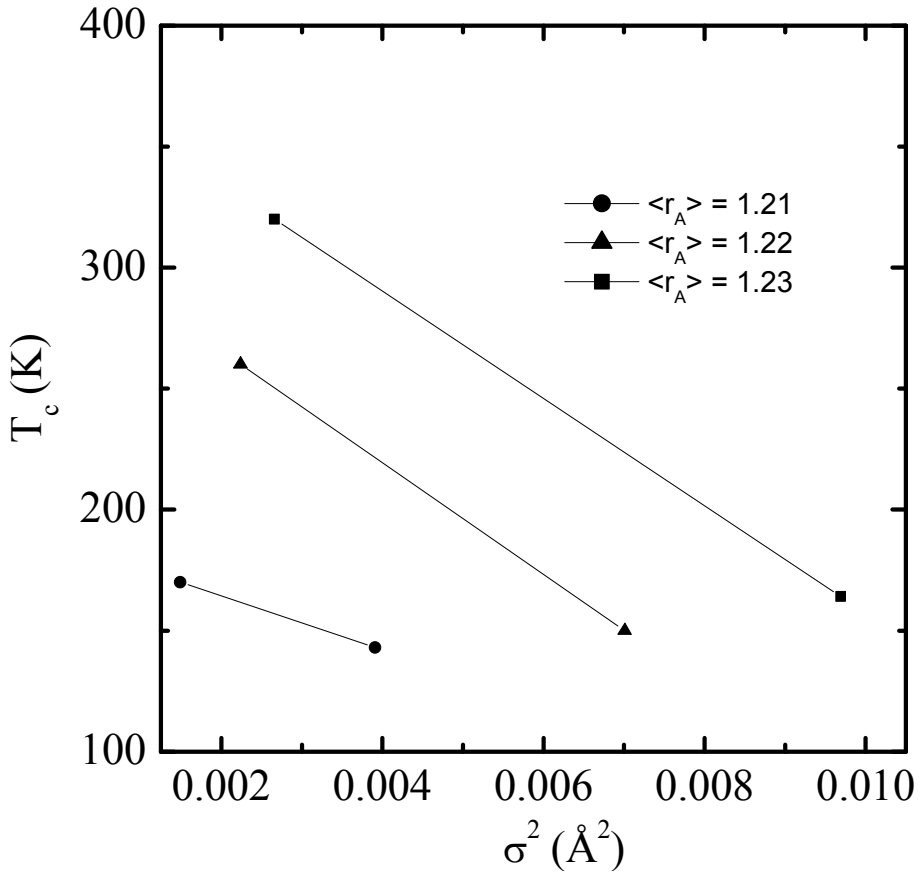

Figure 4.17: Variation of I-M transition temperature (T_p) as a function of varying size-disorder of a pair of samples having constant <r_A> from both the LPCSMO and LPCBMO series.

It is observed from the fig. 4.17 that, the fall in T_c for the set of Sr-Ba doped samples with < r_A> = 1.23 is maximum as compared to samples with < r_A> = 1.22 and 1.21. The samples with maximum drop in T_c possess large variation in the size variance. The values given in Table-3.1 and figs 4.16 and 4.17 reveal that the LPCSMO has more impact of increasing <r_A> on the large enhancement of T_p as the Sr^{2+} concentration increases. In LPCBMO series, though <r_A> increases significantly and should enhance the T_p more than that in LPCSMO series with increasing substitution. However, it is not the

case as the T_p enhancement is slow in LPCBMO series and this may be attributed to the detrimental effect of increasing size-disorder on the T_p.

The Ba being a larger cation puts a strain on the lattice, which is evident from the low rate of rise in T_c and broader nature of transition. The size mismatch at A-site due to larger Ba cation results in the random displacement of oxygen ions and hence influences the Mn-O hybridization [20]. This induces the local spin and position dependent fluctuations in the lattice. The increasing Ba concentration increases the size variance at A site and this affects the motion of electrons significantly. If the size variance at A site increases beyond a limit then structural deformation leads to phase segregation which is evident from the structural studies on $La_{0.4}Pr_{0.3}Ba_{0.3}MnO_3$ sample in which the Pr concentration was increased to enhance the variance for a constant carrier density.

4.4 Conclusions

Effects of competing tolerance factor and size-disorder at A-site on the structural and transport properties have been studied in Sr^{2+} and Ba^{2+} substituted nearly low-bandwidth $La_{0.5}Pr_{0.2}Ca_{0.3}MnO_3$ systems, resulting in the two series as $La_{0.5}Pr_{0.2}Ca_{0.3-x}Sr_xMnO_3$ ($0 \leq x \leq 0.30$) and $La_{0.5}Pr_{0.2}Ca_{0.3-x}Ba_xMnO_3$ ($0 \leq x \leq 0.30$) An increase in substitution of larger cation Ba at Ca site as compared to Sr, results in an enhanced size mismatch, thereby increasing the strain on the lattice and affecting the motion of electrons significantly. This decreases the rate of T_c enhancement due to Ba substitution and results in broader resistive transitions.

References

1. Ramirez A P, J. Phys: Condens. Mater, **9**, 5171 (1997)
2. Coey J M D, Viret M and Von Molnar S, Advances in Phys., **48**, 2, 167 (1999)
3. Von Helmolt R, Wecker J, Holzapsfel B, Schultz L and Samwar K, Phys. Rev. Lett., **71**, 2331 (1993)
4. Gooenough J B, Aust. J. of Phys., **52**, 155 (1999)
5. Rodriguez-Martinez L M and Attfield J P, Phys. Rev. B, **54**, R15622 (1996)
6. Emin D and Holstein T, Phys. Rev. B, **13**, 647 (1976)
7. Ziese Michael, Srinitiwarawong Chatchai, Phys. Rev. B, **58**, 11519 (1998)
8. Coey J M D, Viret M, Ranno L, Ounadjela K, Phys. Rev. Lett., **75,** 3910 (1995)
9. Viret M, Ranno L, Coey J M D, J. Appl. Phys., **81,** 4964 (1997)
10. Gupta A, Gong G Q, Xiao Gang, Duncombe P R, Lecoeur P, Trouilloud P, Wang YY, Dravid V P and Sun J Z, Phys. Rev. B, **54**, 629 (1996)
11. Hwang H Y, Cheong S-W, Ong N P and Batlogg B, Phys. Rev. Lett., **77**, 2041 (1996)
12. Ju Sheng, Sun H, Li Zhen-Ya, Phys Letts A, **300**, 666 (2002)
13. Hielman A K, Xue Y Y, Lorenz B, Campbell B J, Cmaidalka J, Wang R L, Chu C W, Phys. Rev.B, **65**, 214423 (2002)
14. I. E. Dzyaloshinskii, Zh. Eksp. Teor. Fiz. **72**, 1930 (1977) [Sov. Phys. JETP **45**, 1014 (1977)]
15. A. de Andrés, M. García-Hernández, and J. L. Martínez, Phys. Rev. B, **60,** 7328 (1999)
16. E. Dagotto, Takashi Hotta and Adriana Moreo Physics Reports **344**, 1-153, (2003)

17. H. Y. Hwang, S. W. Cheong, N. P. Ong, and B. Batlogg, Phys. Rev. Lett. **77**, 2041 (1996)

18. X. W. Li, A. Gupta, G. Xiao, and G. Q. Gong, Appl. Phys. Lett. **71**, 1124 (1997)

19. J. M. D. Coey, *Philos.* Trans. R. Soc. London, Ser. A, **356**, 1539 (1998)

20. H. L. Ju, J. Gopalakrishnan, J. L. Peng, Qi Li, G. C. Xiong, T. Venkatesan, and R. L. Greene, Phys. Rev. B **51**, 6143 (1995)

Chapter – V

Introduction

The simultaneous substitution of Pr-Ca induces interesting properties in the resulting manganite system. The $La_{1-2x}Pr_xCa_xMnO_3$ in the previous chapter has been identified as a low bandwidth system exhibiting transition temperature below 120 K with significant CMR effect at relatively weaker fields [1, 2]. However, we have optimized this series with a sample to show that an optimal density $La_{0.5}Pr_{0.2}Ca_{0.3}MnO_3$ composition exhibit low T_p and T_C with a large MR%. In this chapter we have taken this sample as basis for the study of bandwidth modifications and cation size variance effect by Sr^{2+} and Ba^{2+} substitution on the electronic, magnetic and magnetotransport properties of the resulting system. In this endeavor, we have synthesized two series as $La_{0.5}Pr_{0.2}Ca_{0.3-x}Sr_xMnO_3$ (LPCSMO); x = 0.0-0.20 (0.05) and $La_{0.5}Pr_{0.2}Ca_{0.3-x}Ba_xMnO_3$ (LPCBMO); x = 0.0-0.30 (0.05). Lastly, we show that, increasing the cation size variance above a certain limit in $La_{0.4}Pr_{0.3}Ba_{0.3}MnO_3$ results in the phase-segregation indicative from the extra peaks of $BaMnO_3$ in the XRD spectrum. The conductivity in the semiconducting region is dominated by Mott's Variable Range Hopping type of conduction of polarons [3]. The structural, electrical, magnetic and magnetotransport properties have been studied using XRD, magnetoresistance and magnetic susceptibility measurements in the light of bandwidth modification and cation size disorder effects.

As mentioned earlier I-M & PM-FM transition temperatures, which are due to spin-polarized conduction of carriers through Zener-Double exchange depends upon the e_g electron bandwidth and carrier density [4]. $La_{0.7}Ca_{0.3}MnO_3$ (LCMO) and $Pr_{0.7}Ca_{0.3}MnO_3$ (PCMO) are intermediate and low bandwidth systems respectively. The dependence of transition temperature is ascribed to the amount of divalent cation doping and average A-site cation radius which is quantified by a tolerance factor, t = <A-O>/(√2<Mn-O>).

L.M. Rodriguez-Martinez *et al* [5] defined a quantitative factor called size variance, $\sigma^2=\sum x_i r_i^2-\langle r_A\rangle^2$ - - - - (1), where x_i is the fractional occupancy of the cation with ionic radius r_i and $\langle r_A\rangle$ is the average A-site cation radius; characteristic of the mismatch of size of the different cations occupying A-site and studied its effect on the structural and transport behavior [5]. It is an established fact that, the optimal divalent cation doping of 33% in the absence of any cation size mismatch induces the largest possible concomitant electrical and magnetic transition temperatures. The effect of substitution of larger cation Sr^{2+} is interesting to observe the bandwidth modification and cation size mismatch effects. We have studied the $La_{0.5}Pr_{0.2}Ca_{0.3-x}Sr_xMnO_3$ (LPCSMO); x = 0.0-0.20 (0.05) and $La_{0.5}Pr_{0.2}Ca_{0.3-x}Ba_xMnO3$ (LPCBMO); x = 0.0-0.30 (0.05) systems with an aim to investigate the modifications in the transport and MR behavior with increasing bandwidth and size disorder.

4.1 Studies on $(La_{0.5}Pr_{0.2})(Ca_{0.3-x}Sr_x)MnO_3$ (LPCSMO)

x = 0.0-0.20 (0.05) series

4.1.1 Experimental details & structural studies

High purity La_2O_3, Pr_6O_{11}, $CaCO_3$, $SrCO_3$, $BaCO_3$ and MnO_2 powders were taken for synthesizing the thoroughly mixed and calcinated at 950ºC. All the samples were pelletized and sintered in the range of 1100-1400ºC with several intermittent grindings. A.c and d.c. susceptibility measurements were carried out for the magnetic susceptibility studies.

XRD measurements using Cu-K_α radiation were performed for the structural determination and phase purity. The Rietveld refinement program using FULLPROF

program was employed. The refined XRD patterns of all the samples are given in figure 4.1, while figure 4.2 shows a typical Rietveld fitted pattern of x=0.15 sample.

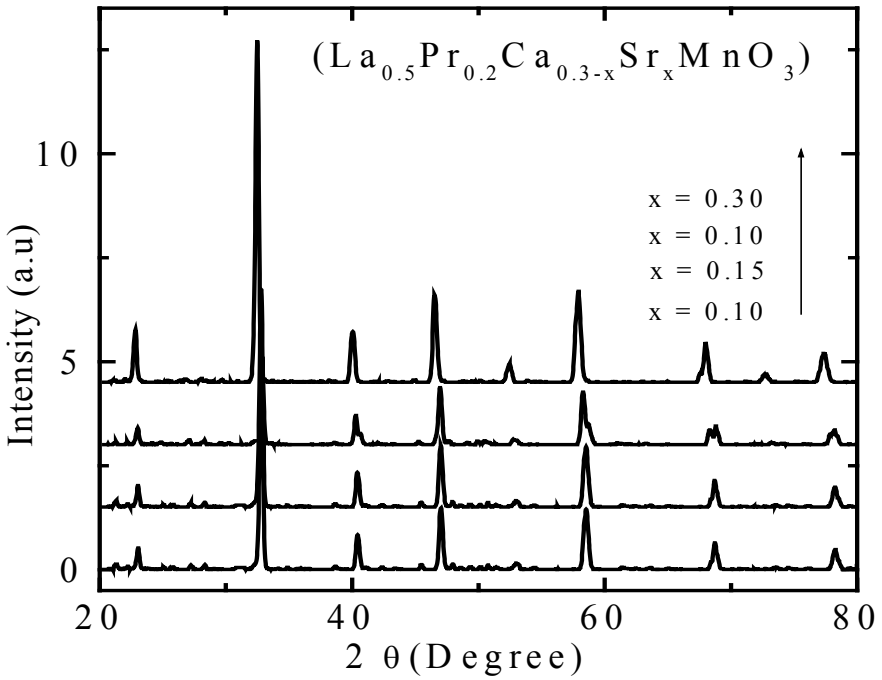

Figure 4.1: XRD pattern of the $La_{0.5}Pr_{0.2}Ca_{0.3-x}Sr_xMnO_3$ (x = 0.0 - 0.20)

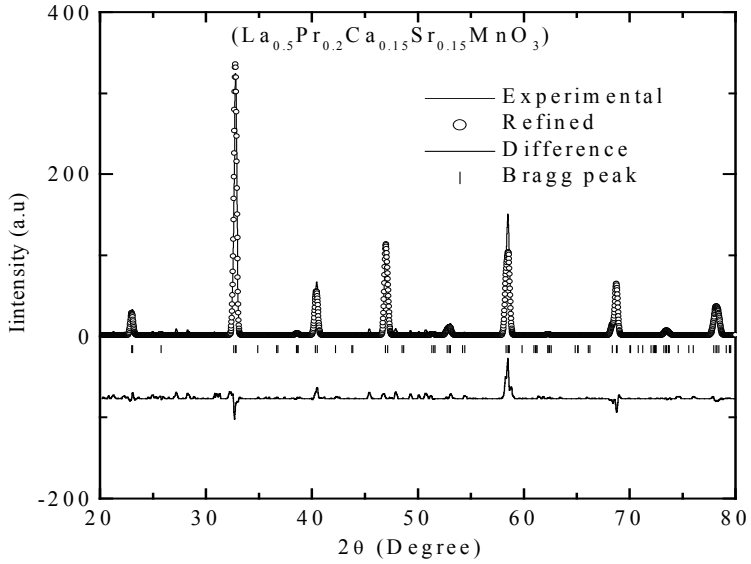

Figure 4.2: Rietveld fitted XRD pattern of the $La_{0.5}Pr_{0.2}Ca_{0.3-x}Sr_xMnO_3$ (x=0.15)

Rietveld refinement using FULPROOF program of all the samples for phase purity and structural investigations reveals a good phase formation with an impurity ~1-2% of mother compounds for some of the samples. In this series all the samples fit to a distorted orthorhombic structure. The cell parameters and hence the volume increases with increasing Sr concentration, which can be attributed to larger size cation substitution effect. Table – 4.2 shows the variation of cell parameters, cell volume $<r_A>$ and σ^2 wih increasing x.

Table 4.1 : Structure, cell parameters and cell volume of $La_{0.5}Pr_{0.2}Ca_{0.3-x}Sr_xMnO_3$ ($0 \leq x \leq 0.20$) samples.

x	Structure	a (Å)	b (Å)	c (Å)	Volume(Å^3)
0	Orthorhombic (*Pnma*)	5.4576(1)	7.7224(2)	5.4436(2)	229.426
0.05	Orthorhombic (*Pnma*)	5.4482(1)	7.7295(1)	5.4633(1)	230.078
0.10	Orthorhombic (*Pnma*)	5.4559(2)	7.7145(1)	5.4774(2)	230.532
0.15	Orthorhombic (*Pnma*)	5.4859(1)	7.7145(2)	5.4592(1)	231.045
0.20	Orthorhombic (*Pnma*)	5.4995(2)	7.7165(1)	5.4613(2)	231.764

4.1.2 Electronic transport and magnetoresistance

Fig. 4.3 depicts the R-T and magneto R-T behaviour of LPCSMO samples in absence of magnetic field and in applied magnetic fields of 1 Tesla, 2 Tesla and 5 Tesla. The electrical transport behavior of the LPCSMO system, reveals that, as Sr^{2+} concentration increases, the transition temperature increases with a subsequent fall in resistivity, which has its origin in the modification of e_g electron bandwidth as the average A-site cation radius increases by Sr^{2+} substitution.

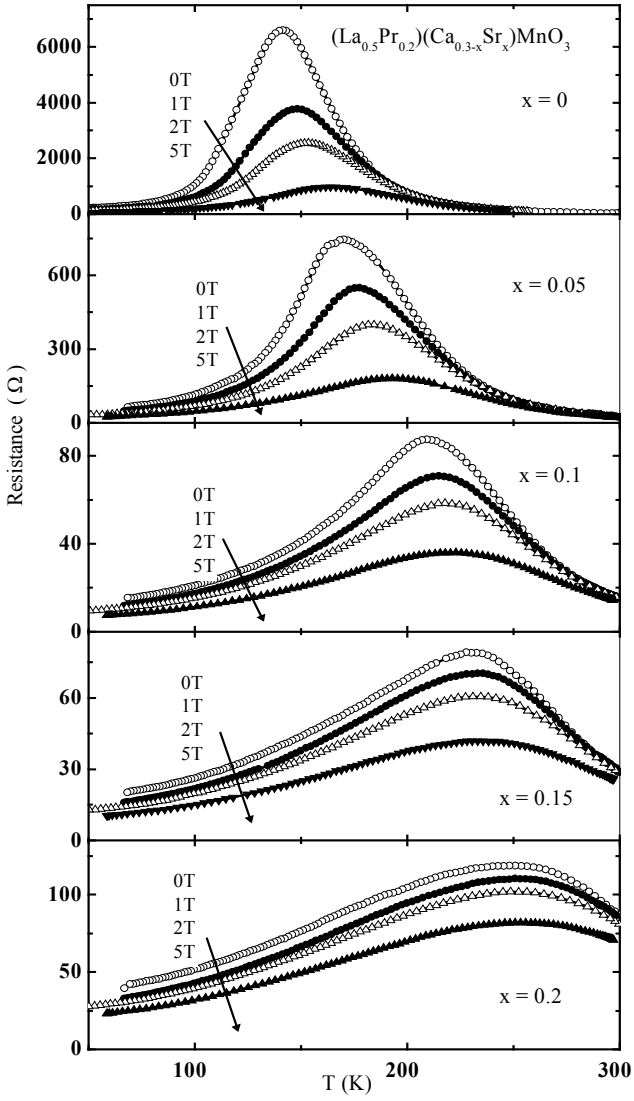

Figure: 4.3 R-T and magneto R-T plots for $La_{0.5}Pr_{0.2}Ca_{0.3-x}Sr_xMnO_3$; x = 0.0 - 0.20 (0.05) series.

In order to understand the conduction mechanism of polarons created as a result of electron-phonon coupling in the semiconducting region, we fitted the R-T data LPCSMO samples in figure 4.4, to nearest neighbor small polaron hopping model [6, 7] corresponding to $\rho = \rho_0 \exp(E_a/kT)$ and the Mott's type Variable Range Hopping model [8, 9] (VRH) corresponding $\rho = \rho_o \exp(T_o/T)^{1/4}$.

As shown in figures 3 & 4, the data fits linearly in ln ρ vs. $T^{-0.25}$ plot, suggesting that, the conduction of the carriers in the semiconducting region obeys the Mott's Variable Range Hopping model. T_o in this equation is related to localization length by a relation,

$$kT_o = 18/L^2 N(E) \quad \text{- - - -} \quad (2)$$

where L is the localization length of the carriers and N(E) is the density of states.

It is observed from the magneto R-T measurements on Sr^{2+} substituted $La_{0.5}Pr_{0.2}Ca_{0.3-x}Sr_xMnO_3$ system (fig.2) that, T_p increases with increasing Sr content and a subsequent fall in MR%. The transition temperature is revived from 140 K to 247 K and CMR effect falls from 46% to 7% at a field of 1T with the 20% substitution of Sr^{2+}. Since the larger cation increases the Mn-O-Mn bond angle towards 180º and the fall in the magnetic disorder at the Mn-O couplings accounts for the low CMR effect [10]. Interestingly the CMR effect increases consistently at low temperature below transition temperature with increasing Sr content. This low temperature large CMR effect is due to the intergrain tunneling magnetoresistance [11]. The drop in the resistance in the higher magnetic field also increases with doping concentrations.

The magnetoresistance also occurs as result of the reduction of the scattering of the carriers at the interfaces due to application of magnetic field. The scattering of the carriers at the interfaces can be understood in the following way [12]. An electron moving from initial grain to the next magnetic grain crosses two interfaces in its journey, each of which may scatter the electron. This acts as an insulating barrier to the conduction of the carriers through the grains. Since A-site is occupied by different size cations, so unlike cations may occupy the positions at the faces of the adjacent grains. Hence, due to increasing size variance, the Mn environment varies at the interfaces of the connecting grains, which results in equal probability of weak and strong scattering of electrons at the interfaces. The

strong scattering can be suppressed by the application of larger magnetic fields, to account for the larger drop in resistance as size disorder increases with Sr content. Another notable factor is that, the trend in the increase in T_C is not linear with Sr concentration, being larger for lower compositions and smaller for higher Sr content. This leads to deviation in the ideal relationship of Tc and tolerance factor [4].

It can be explained by the mismatch of the cations at A-site, which increases with Sr content. The large size variance, as calculated from equation, $\sigma^2 = \sum x_i r_i^2 - < r_A >^2$, induces the strain in the lattice by random displacement of oxygen ions and hence obstructs the Zener-Double exchange.

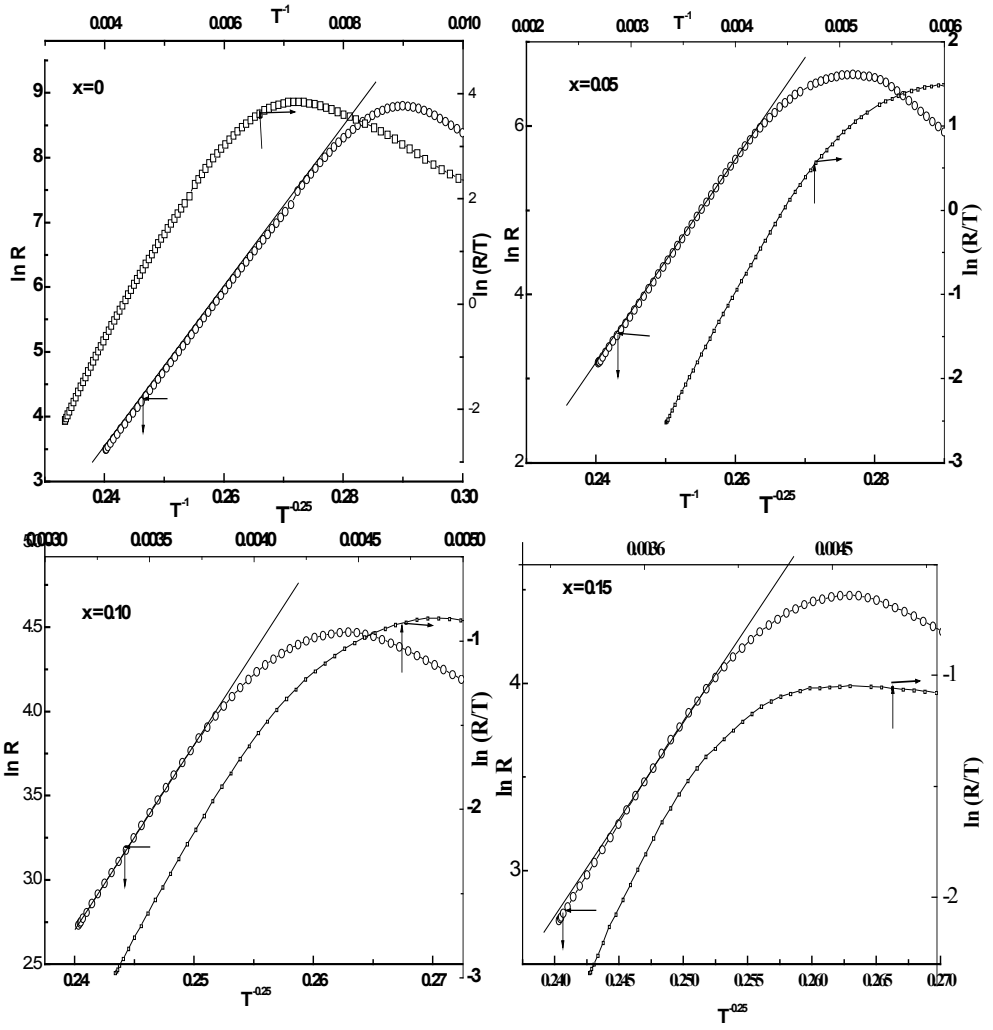

Figure 4.4: Mott's VRH model (ln R vs $T^{-0.25}$) and small polaron model (ln (R/T) vs T^{-1}) fits for $La_{0.5}Pr_{0.2}Ca_{0.3-x}Sr_xMnO_3$; x = 0.0 - 0.15 (0.05) series.

The fitting of the electrical transport data in the semiconducting region reveals that conduction in this region occurs through the Mott's Variable Range hopping of polarons. CMR effect is found to have an inverse relationship with the transition temperature. The A-site disorder increases with Sr concentration and leads to microscopic inhomogenieties in the samples through the random displacement of oxygen anion and showing its influence on the electrical, magnetic and magnetotransport properties.

4.1.3 Magnetization

The magnetic susceptibility plots for LPCSMO samples (fig. 4.5) shows an increasing trend in Curie temperature with increasing Sr content. It is inferred that the magnetic irreversibility decreases with increasing transition temperature.

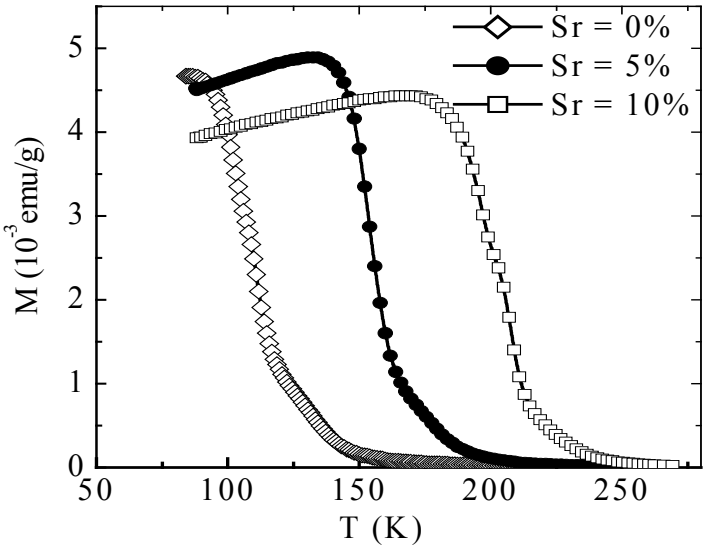

Figure 4.5: Magnetic susceptibility vs Temperature plots for $La_{0.5}Pr_{0.2}Ca_{0.3-x}Sr_xMnO_3$ series.

4.2. Studies on $(La_{0.5}Pr_{0.2})(Ca_{0.3-x}Ba_x)MnO_3$ (LPCBMO) ($0.05 \leq x \leq 0.3$)

In addition to Sr^{2+}, Ba^{2+} is another divalent cation which is interesting for substitution at A-site due to two reasons, namely, 1) due to its larger size (~1.47Å) it enhances the tolerance factor significantly and 2) due to large mismatch with size of the other cations at A-site, it increases the A-site size-disorder. As mentioned earlier, the increasing size disorder increasing the intrinsic inhomogenieties, which may affect the transport, magnetic and magnetotransport properties of the resulting compounds. As shown in the previous section, the $La_{0.5}Pr_{0.2}Ca_{0.3}MnO_3$ is a suitable system for

substitutional studies aiming to elucidate the effect of tolerance factor and size-variance. Keeping this in mind, we have replaced the smaller size divalent cation, Ca^{2+}, by a larger size cation, Ba^{2+}, in the system $(La_{0.5}Pr_{0.2})(Ca_{0.3-x}Ba_x)MnO_3$ ($0.05 \leq x \leq 0.3$) and studied the ionic size and size disorder effect on the structural, transport and magnetic properties. In this series, the size-disorder increases from $0.0001 Å^2$ for x=0 to $0.016 Å^2$. Such a large variation of size-disorder across the series makes all these compounds, an interesting subject of investigations. Other than this series of compounds, we have also tried to synthesize the compound, $La_{0.4}Pr_{0.3}Ba_{0.3}MnO_3$, which possesses the largest size-disorder among all the compounds studied in this section. In the $La_{0.4}Pr_{0.3}Ba_{0.3}MnO_3$ manganite sample, we find the chemical phase-segregation, resulting in secondary phase [14]. The various structural, transport, magnetotransport and magnetic properties are collated in the following sections.

4.2.1 Experimental details

All the $(La_{0.5}Pr_{0.2})(Ca_{0.3-x}Ba_x)MnO_3$ ($0.05 \leq x \leq 0.3$) and $La_{0.4}Pr_{0.3}Ba_{0.3}MnO_3$ compounds were synthesized using conventional solid-state reaction route. Constituent oxides (La_2O_3, Pr_6O_{11}, and MnO_2) and carbonates ($SrCO_3$ and $CaCO_3$) were mixed thoroughly in stoichiometric proportions and calcined at 950°C for 24 hours. These were ground, pelletized and sintered in the temperature range of 1100°C - 1200°C for 100 hours with many intermediate grindings. The final sintering was carried out at 1300°C for 24 hours. X-ray diffraction (XRD) patterns were recorded in the 2θ range of $20^o - 80^o$ on a Siemens diffractometer. Magnetization measurements were performed using a SQUID magnetometer (MPMS XL, Quantum Design). The resistivity and magnetoresistance

measurements were carried using d.c. four probe method on a physical property measurement system (PPMS, Quantum Design).

4.2.2 Structural Studies

The XRD patterns of all the $(La_{0.5}Pr_{0.2})(Ca_{0.3-x}Ba_x)MnO_3$ $(0.05 \leq x \leq 0.3)$ (to be referred as LPCBMO) samples were indexed to be single phase compounds crystallizing in a distorted orthorhombic structure. Rietveld refinement technique using FULLPROF software was employed to obtain to refined cell parameters. Figure 4.6 shows the XRD patterns of all the samples while figure 4.7 displays a typical Rietveld refined XRD pattern of x=0.2 and $La_{0.4}Pr_{0.3}Ba_{0.3}MnO_3$ (LPBMO) samples. It is seen that there is an excellent agreement of experimental and fitted patterns of x=0.20 sample and is, therefore, single-phase compound. However, when LPBMO fitted to orthorhombic structure shows some additional peaks in the structure indicated by (*), presumably of $BaMnO_3$ [6]. This sample has maximum A-site size-disorder and may be the cause of the structural phase segregation. This shows that, above a certain critical limit of A-site size-disorder, it exert a structural strain and results in phase-segregation. Table – 4.2 shows the variation of cell parameters, cell volume $<r_A>$ and σ^2 with increasing x.

Table 4.2: Structure, cell parameters and cell volume of $(La_{0.5}Pr_{0.2})(Ca_{0.3-x}Ba_x)MnO_3$ $(0.05 \leq x \leq 0.3)$ samples.

$(La_{0.5}Pr_{0.2})(Ca_{0.3-x}Ba_x)MnO_3$ $(0.05 \leq x \leq 0.3)$	a (Å)	b (Å)	c (Å)	Cell Volume
X=0.05	5.46603(2)	7.72868(2)	5.47161(2)	231.149
X=0.10	5.47066(2)	7.73082(2)	5.49513(2)	232.404

X=0.15	5.47913(2)	7.7416(2)	5.51209(2)	233.808
X=0.20	5.48911(2)	7.75494(2)	5.52533(2)	235.201
X=0.25	5.49859(2)	7.76887(2)	5.48911(2)	236.439
X=0.3	5.51182(2)	7.79095(2)	5.54783(2)	238.237

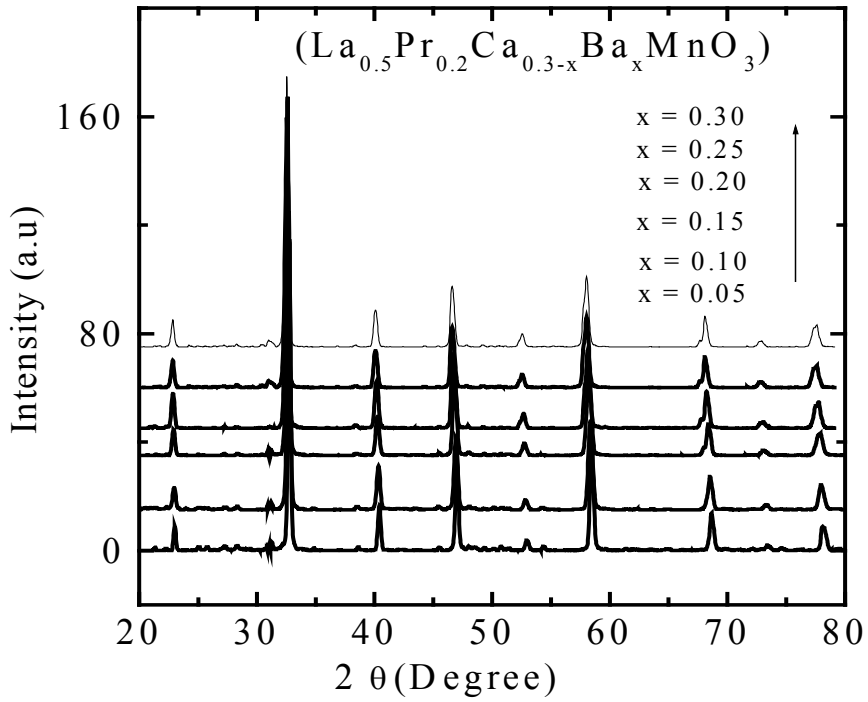

Figure 4.7: XRD patterns of the $(La_{0.5}Pr_{0.2})(Ca_{0.3-x}Ba_x)MnO_3$ ($0.05 \leq x \leq 0.3$) sample

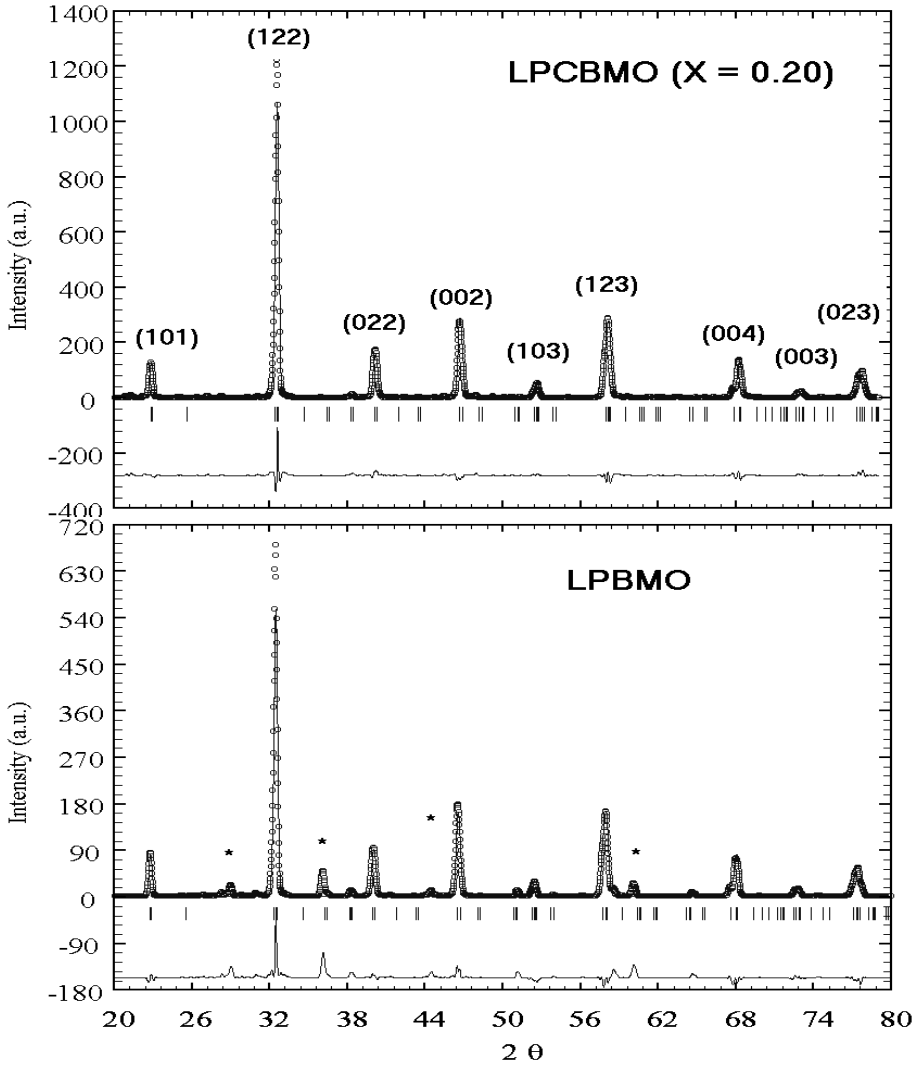

Figure 4.8: Rietveld fitted patterns of $(La_{0.5}Pr_{0.2})(Ca_{0.3-x}Ba_x)MnO_3$ (x=0.20) and $La_{0.4}Pr_{0.3}Ba_{0.3}MnO_3$ samples. The asterisks in the fitted patterns of LPBMO sample (Lower panel) depict the secondary phase of $BaMnO_3$.

4.2.3 Electrical Resistivity

The plots of electrical resistivity as a function of temperature for all the $(La_{0.5}Pr_{0.2})(Ca_{0.3-x}Ba_x)MnO_3$ ($0.05 \leq x \leq 0.3$) in zero field and in a fields of 5T and 9T over a temperature range of 5 K-320 K. The plots are shown in figs. 4.9 and 4.10.

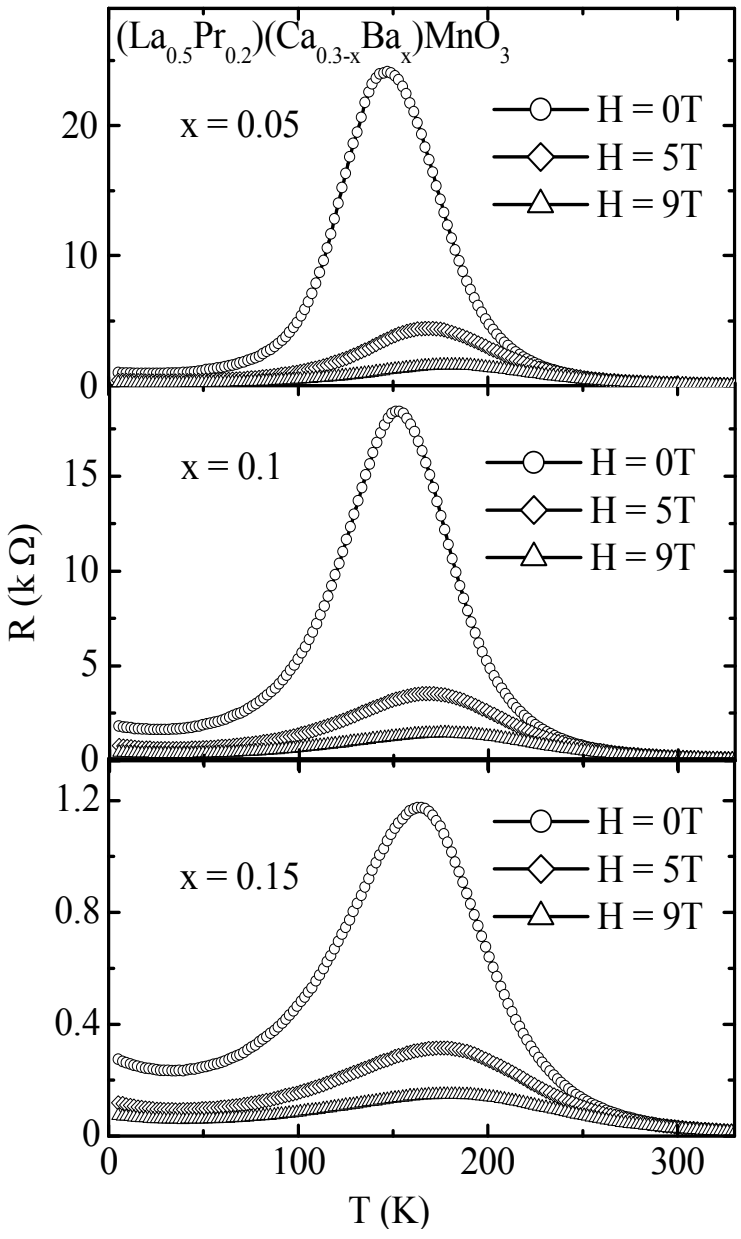

Figure 4.9: Resistivity as a function of temperature in 0T, 5T and 9T in a temperature range of 5 K-320 K for $(La_{0.5}Pr_{0.2})(Ca_{0.3-x}Ba_x)MnO_3$ ($0.05 \leq x \leq 0.15$) samples.

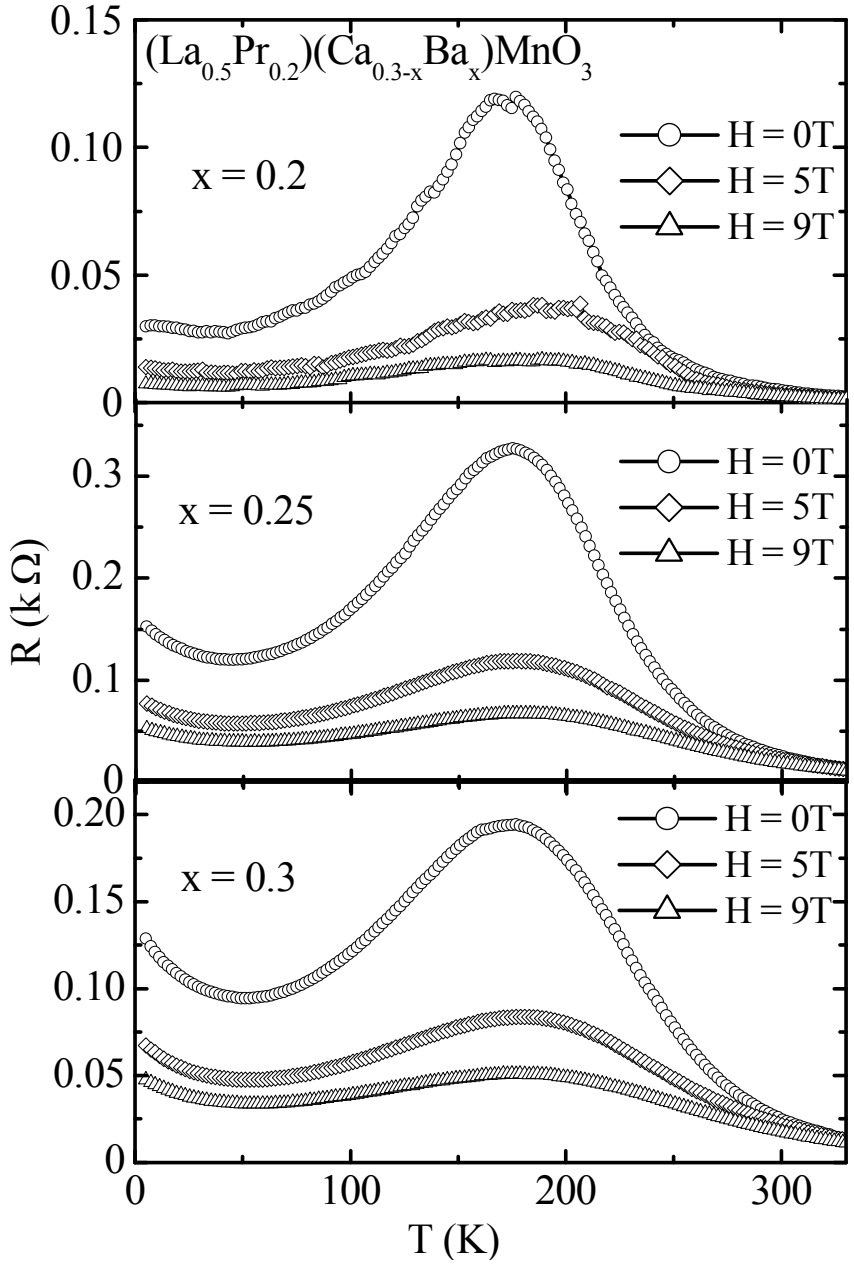

Figure 4.10: Resistivity as a function of temperature in 0T, 5T and 9T in a temperature range of 5 K-320 K for $(La_{0.5}Pr_{0.2})(Ca_{0.3-x}Ba_x)MnO_3$ ($0.20 \leq x \leq 0.30$) samples.

It is seen in figs. 4.9 & 4.10 that all the $(La_{0.5}Pr_{0.2})(Ca_{0.3-x}Ba_x)MnO_3$ $(0.05 \leq x \leq 0.30)$ samples exhibit insulator-metal transition. The I-M transition temperature, T_p, increases from ~145 K for x=0.05 sample to ~175 K for x=0.30 sample. This enhancement in T_p may be understood on the basis increase in tolerance factor with increasing Ba^{2+} content. Progressive substitution of Ba^{2+} (1.47Å) at Ca^{2+} (1.18Å) induces a large increase in average A-site cation radius and hence the tolerance factor increases to a larger extent.

4.2.4 Magnetization measurements

The temperature dependence of magnetization measurements for all the samples were performed in zero-field-cooled (ZFC) and field-cooled (FC) manner. This implies that sample is cooled in zero-field (ZFC) to the lowest temperature and then a certain field is applied for measuring the magnetization of the sample in warming direction. After this temperature of magnetization, the sample is cooled in the same magnetic field (FC) to the lowest temperature and then measured the magnetization while warming. The ZFC and FC magnetization versus temperature for all the $(La_{0.5}Pr_{0.2})(Ca_{0.3-x}Ba_x)MnO_3$ $(0.05 \leq x \leq 0.30)$ samples is shown in fig. 4.11.

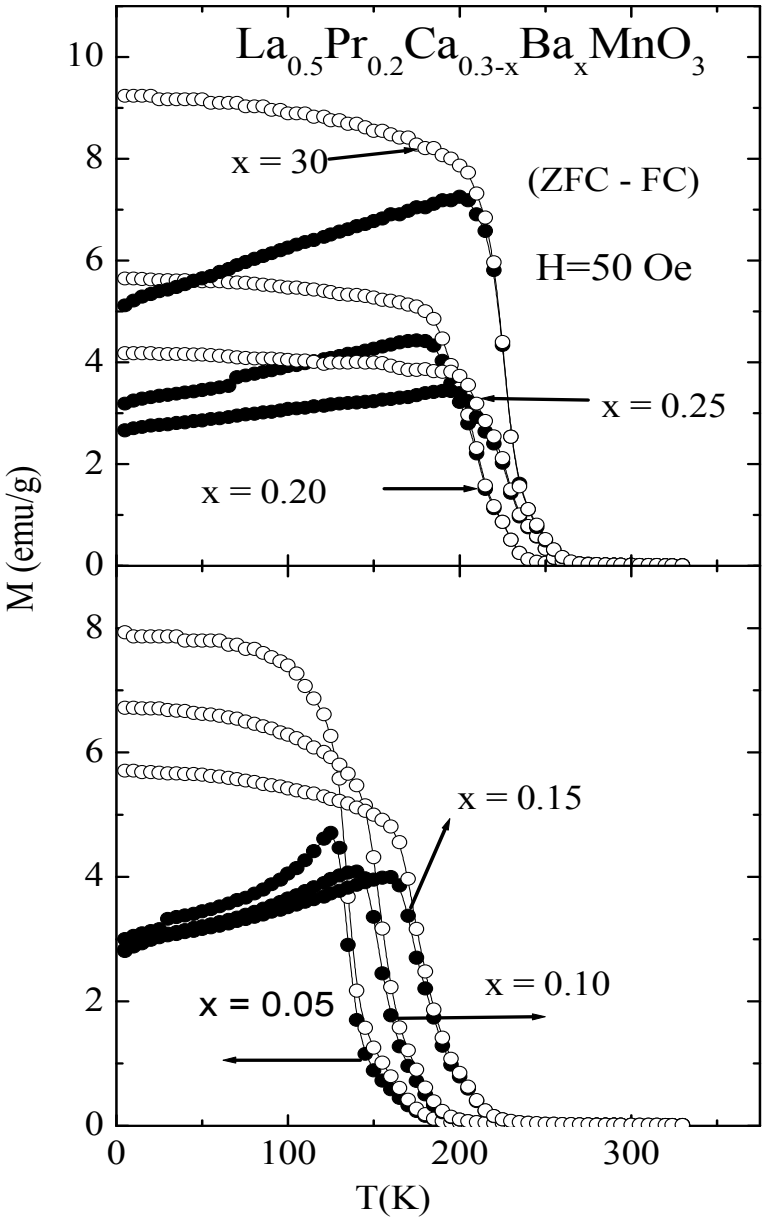

Figure 4.11: Zero-field-cooled (ZFC) and field-cooled (FC) magnetization (M) as a function of temperature for $(La_{0.5}Pr_{0.2})(Ca_{0.3-x}Ba_x)MnO_3$ samples in a field of 50 Oe.

The Curie temperature (T_C) increases from 150K for x=0.05 to 220K for x=0.30. With increasing Ba-substitution, the increasing trend of T_C is similar to increasing trend of the insulator-metal transition temperature (T_p). However, it is seen that the T_C and T_p of

these samples do not match with each other and this disparity increases with increasing Ba-concentration. This disparity is not in accordance with the Zener-Double-Exchange interactions and can be explained on the purview of possible grain boundary localization or phase separation. It is needless to mention that the polycrystalline samples of various micron sized grains, in which properties may vary inside the grain and on the grain boundaries. As the ZDE come into play, the bulk part of the grain become ferromagnetic and metallic while the grain boundaries are still insulating. The grain boundaries may be insulating because of the grain boundary pinning of Mn-ion spins, poor connectivity and grain boundary contamination [15]. This creates the insulating channels at the grain boundaries and does not allow the percolation of the charge carriers and results in insulating behavior even after the onset of T_C. Once the grain boundaries become conducting at lower temperatures, the I-M transitions appear. Other factor that can cause a disparity between T_p and T_C is the phase-separation as explained in [16]. Due to the granular mixture of different electronic densities, the T_C of different grains could be different. For instance, we assume that majority of the grains have large electronic density so that they exhibit T_C at higher temperatures, while the remaining minor fraction have lower T_C. Now, at the onset of the T_C of majority of grains (with higher T_C), the systems tends to be ferromagnetic even as a minority of grain are still paramagnetic-insulating. In such as a situation, though the system will be ferromagnetic, it will continue to exhibit semiconducting/insulating behavior unless all the grains become ferromagnetic. At a certain temperature when the whole system attains ferromagnetism, percolation is possible and the system exhibits I-M transition. The disparity in T_C and T_p in the present system may be because of either or both of the above stated causes. We get an evidence of the phase separation from the d.c. magnetic susceptibility.

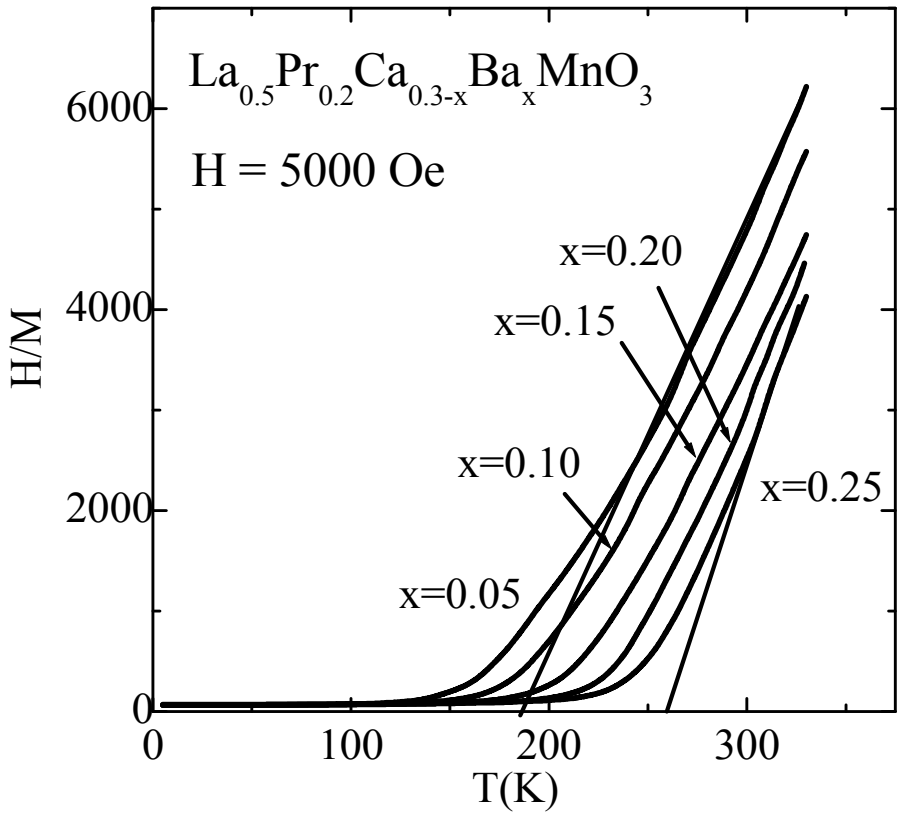

Figure 4.12: Inverse susceptibility (H/M at H = 5 kOe) as a function of temperature for $(La_{0.5}Pr_{0.2})(Ca_{0.3-x}Ba_x)MnO_3$ samples.

Fig. 4.12 shows the inverse susceptibility as a function of temperature for the $(La_{0.5}Pr_{0.2})(Ca_{0.3-x}Ba_x)MnO_3$ ($0.05 \leq x \leq 0.25$) samples when magnetization is acquired in a field of 5kOe. It is seen that there exists a deviation of Curie-Weiss law from the paramagnetic susceptibility of all the samples. This indicates towards the magnetic inhomogeneities or possible existence of ferromagnetic clusters in the paramagnetic region. Such inhomogeneities, which may be present both in paramagnetic and

ferromagnetic regions, suggesting that phase separation could be one cause of disparity of T_C and T_p in these samples.

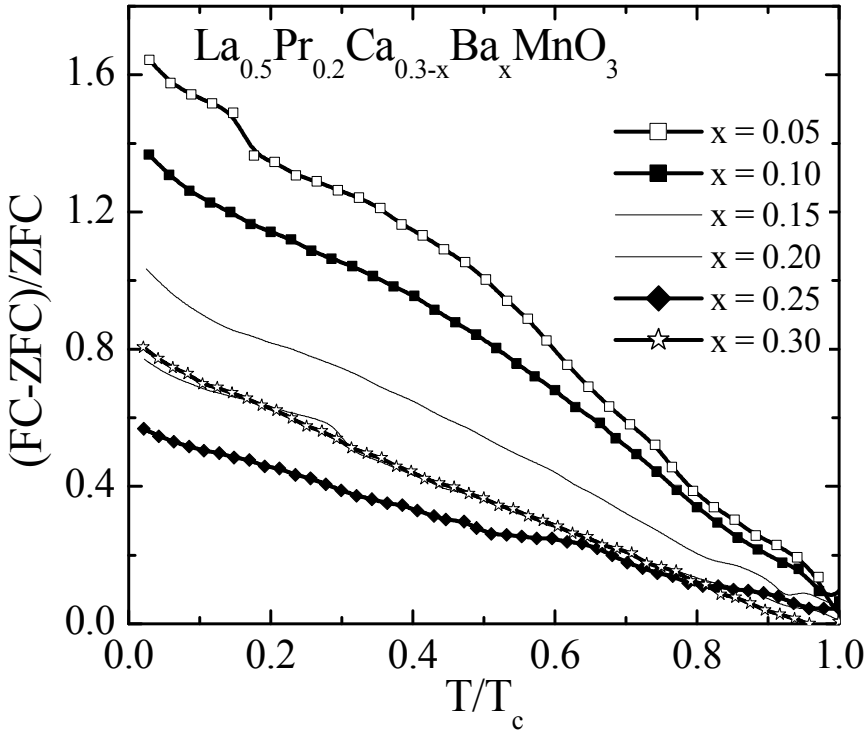

Figure 4.13: Fractional change of magnetization (M_{FC}-M_{ZFC}/M_{ZFC}) versus temperature (T) for all the $(La_{0.5}Pr_{0.2})(Ca_{0.3-x}Ba_x)MnO_3$ samples.

On the other hand, we evidence a large bifurcation of ZFC and FC magnetization curves for all the samples. To quantify this separation, we have plotted a quantity called fraction change in magnetization (M_{FC}-M_{ZFC}/M_{ZFC}) as a function of normalized temperature (T/T_C) in figure 4.13. As seen in this figure that (M_{FC}-M_{ZFC}/M_{ZFC}) decreases as function of increasing Ba^{2+} concentration. The x=0.30 sample does not follow this trend because this sample was prepared in a different batch with a slightly different synthesis route. Also, it is mentioned that generally a bifurcation of M_{ZFC} and M_{FC} arises from grain boundary pinning. In the samples under present study, the a large bifurcation of the two

curves in all these Ba^{2+} substituted samples suggests enhanced grain boundary pinning and, thus, the grain boundary localization [13]. Therefore, this factor is also likely to play a role in the disparity of T_p and T_C of these samples. Thus, by providing experimental evidence of phase-separation and grain boundary localization, we show that these factors cause the I-M transition to occur at lower temperatures than T_C.

4.2.5 Magnetoresistance measurements

The resistance was measured as a function of applied magnetic field at various temperatures for all $(La_{0.5}Pr_{0.2})(Ca_{0.3-x}Ba_x)MnO_3$ ($0.05 \leq x \leq 0.30$) samples. From these data magnetoresistance was calculated using the formula $MR(\%)=\{(\rho_0-\rho_H)/\rho_0\}\times 100$ and the plots of magnetoresistance versus magnetic field isotherms are shown in figs. 4.14 & 4.15. It may be seen that all the samples exhibit maximum MR in the vicinity of their respective I-M transition temperatures. Maximum MR in the vicinity of T_p may be explained on the basis of field induced suppression of spin fluctuation. At the I-M transition, there exists maximum magnetic disorder and magnetic field enhances the ferromagnetic spin ordering. On the other hand, at low temperature we observe two features in MR. One, a large MR of nearly 20% in a low field of 0.5-1 Tesla and other, a low MR at higher fields. Here, a large low-field MR arises from the inter-grain spin-polarized tunneling while a low high-field MR is also because of almost complete spin-polarization at low temperatures.

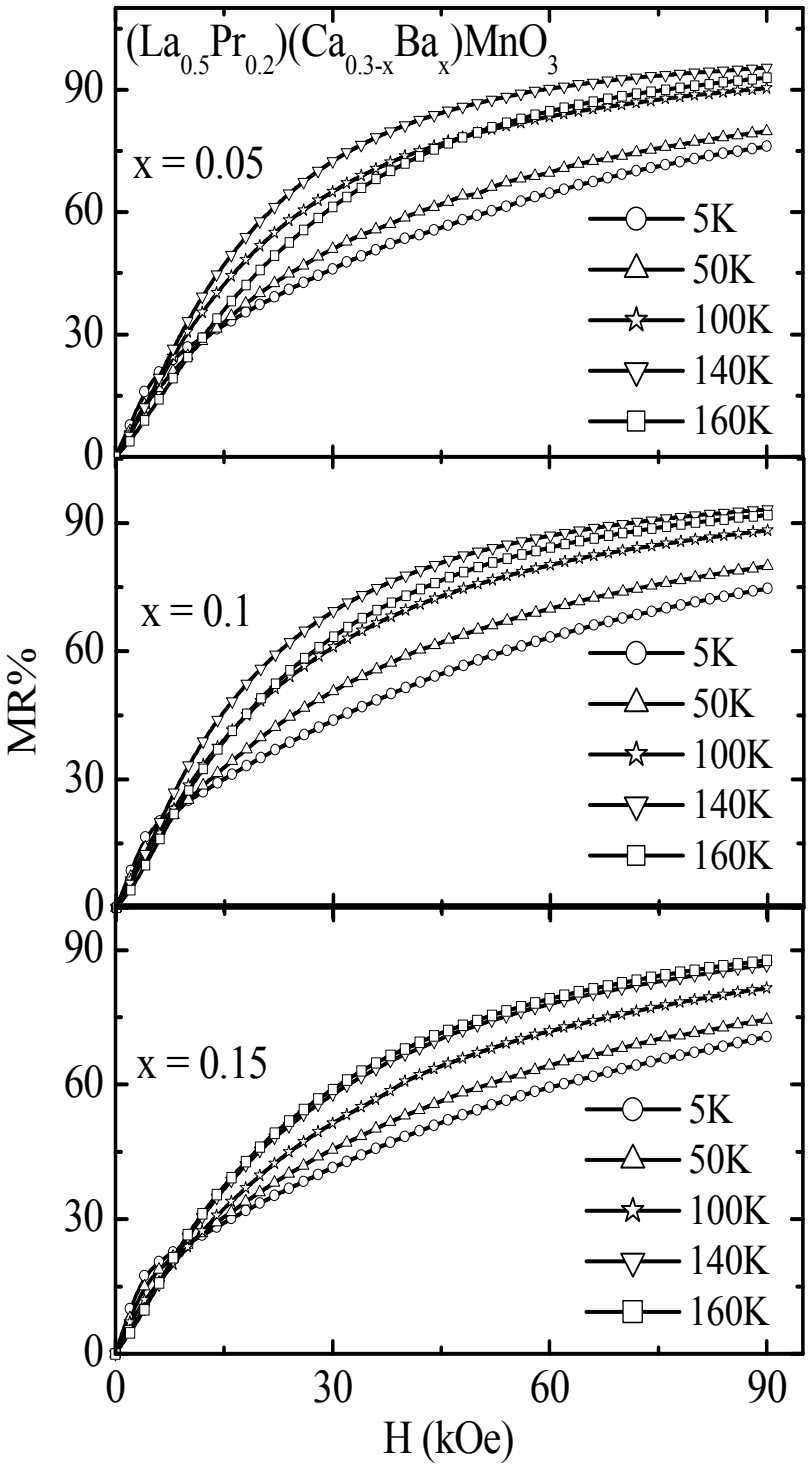

Figure 4.14: Magnetoresistance (MR%) as a function of magnetic field (H) at various temperatures for $(La_{0.5}Pr_{0.2})(Ca_{0.3-x}Ba_x)MnO_3$ ($0.05 \leq x \leq 0.15$) samples.

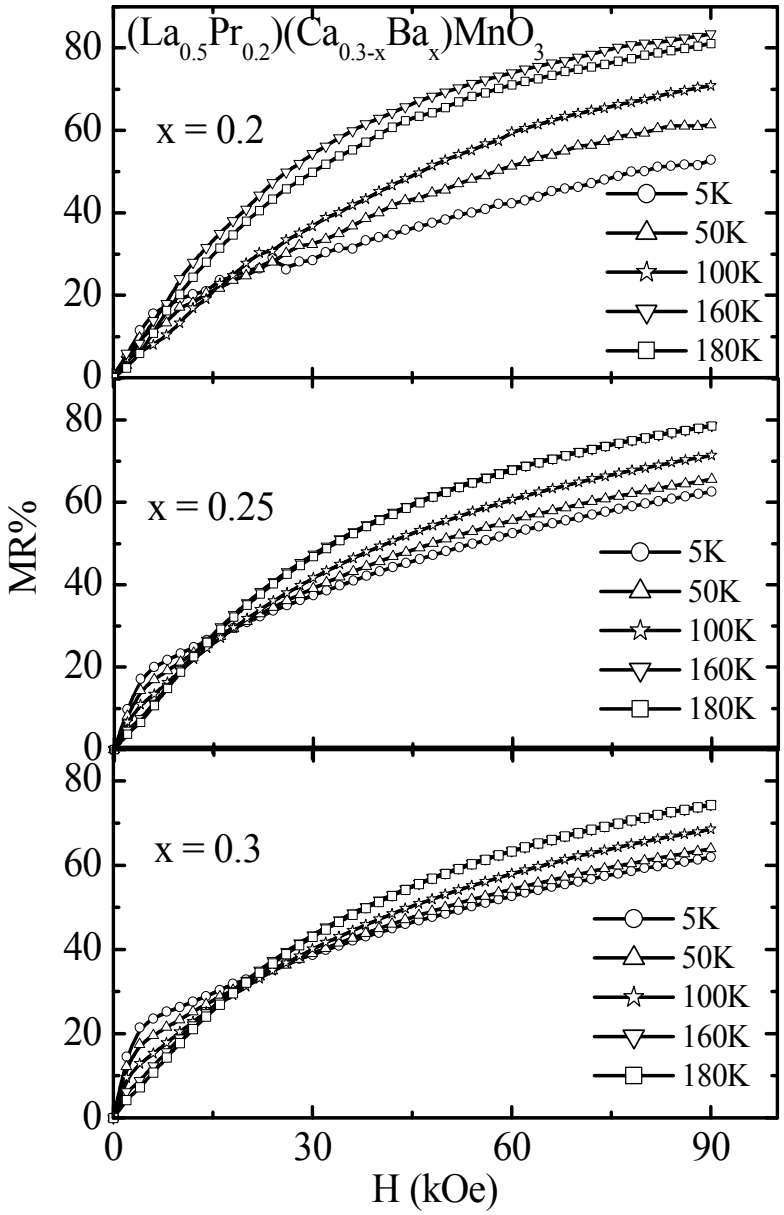

Figure: 4.15 Magnetoresistance (MR%) as a function of magnetic field (H) at various temperatures for $(La_{0.5}Pr_{0.2})(Ca_{0.3-x}Ba_x)MnO_3$ ($0.20 \leq x \leq 0.30$) samples.

In figs. 4.14 & 4.15, we observe that at lower Ba^{2+} substitution, the maximum MR of ~95% for x=0.05 decreases to a maximum of ~75 % for x=0.30 sample in the vicinity of their respective I-M transition temperatures. As the temperature decreases below the I-M transition temperature, the MR starts decreasing. Interestingly, we see two clear trends in MR with decreasing temperature and increasing Ba^{2+} concentration. As the temperature goes below 50 K [17], we observe an enhancement in MR in low-fields while the MR in high-fields decreases. Also, it is seen that the low field MR at low temperatures increases with increasing Ba^{2+} content. This trend may be explained as follows [17, 18, 19]. As Ba^{2+} content increases, the increase in T_C suggests that the spin polarization will increase at low temperatures. The enhanced spin polarization will result in larger spin-polarized inter-grain tunneling on the application of small fields. Hence, we observe increasing low-field MR as the T_C increases with increasing Ba^{2+} concentration. The high field MR at low temperatures occurs due to magnetic disorder at Mn-O-Mn bonds (due to Zener-Double-Exchange) and pinning of Mn-ion spins at the grain boundaries. As stated above the spin polarization increases and, hence, the spin magnetic disorder decreases at the Mn-O-Mn bonds, which results in a low high-field MR as the T_C increases.

4.3 Comparative study of $La_{0.5}Pr_{0.2}Ca_{0.3-x}Sr_xMnO_3$ (LPCSMO); x = 0.0-0.30 (0.05) and $La_{0.5}Pr_{0.2}Ca_{0.3-x}Ba_xMnO_3$ (LPCBMO); x = 0.0-0.30 (0.05)

The substitution of Sr^{2+}(~1.31 Å) and Ba^{2+}(~1.47 Å) in $La_{0.5}Pr_{0.2}Ca_{0.3}MnO_3$ results in the LPCSMO and LPCBMO series, which have mixed impact of tolerance factor and size-disorder on the transport and magnetic and magnetotransport properties. Here we compare some of the properties of these two series. In both LPCSMO and LPBMO series, the tolerance factor and size-disorder increases with increasing substitution of Sr^{2+} and Ba^{2+} respectively. The respective increase in average A-site cation radius ($<r_A>$, which

represents the tolerance factor) and A-site cation disorder in both the series is depicted in Fig. 4.16.

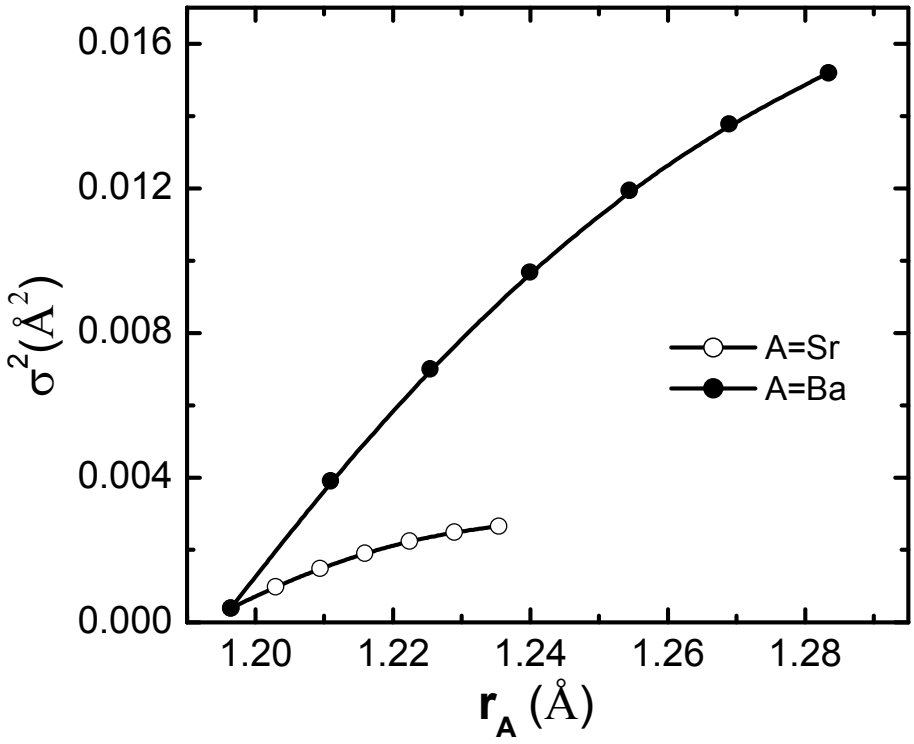

Figure 4.16: Variation of A-site cation size-disorder as a function of $<r_A>$ for both the LPCSMO and LPCBMO series.

It is seen from Fig. 4.16 that the increase in σ^2 with increasing $<r_A>$ is too large in LPCBMO as compared to that in LPCSMO series. However, in spite of large $<r_A>$ (and, therefore, the tolerance factor) of LPBMO series, its electronic and magnetic transition temperatures are lower as compared to LPCSMO series. Table-4.3 lists, for comparison, values of various structural parameters and electronic transition temperatures of these two series.

Table – 4.3: Average A-site cation radius ($<r_A>$), size-disorder (σ^2) and insulator-metal transition temperature (T_p) for $(La_{0.5}Pr_{0.2})(Ca_{0.3-x}A_x)MnO_3$ (A=Sr and Ba).

x	$<r_A>$ (Å) A= Ba(Sr)	σ^2 (Å^2) A=Ba(Sr)	T_p (K) A=Ba(Sr)
0.0	1.196(1.196)	0.00039(0.00039)	140(140)
0.05	1.211(1.203)	0.00391(0.00098)	145(170)
0.10	1.225(1.209)	0.00701(0.00149)	150(205)
0.15	1.239(1.216)	0.00969(0.00191)	164(230)
0.20	1.254(1.222)	0.01195(0.00224)	171(260)
0.25	1.269(1.228)	0.01378(0.00249)	172(----)
0.30	1.284(1.235)	0.0152(0.00266)	175(313)

Similarly, we find a variation in I-M transition temperatures (T_p) as a function of varying size variance (σ^2) for pair of samples of the two series with constant $<r_A>$. Figure 4.17 shows the T_c vs size variance plots for a fixed average A-site ionic radius for $La_{0.5}Pr_{0.2}Ca_{0.3-x}A_xMnO_3$, A = Ba & Sr. For $<r_A>$ =1.21 Å, Ba = 0.05 and Sr = 0.10; for $<r_A>$ = 1.22Å, Ba = 0.10, Sr = 0.20 and for $<r_A>$ = 1.23 Å, Ba = 0.15, Sr = 0.30.

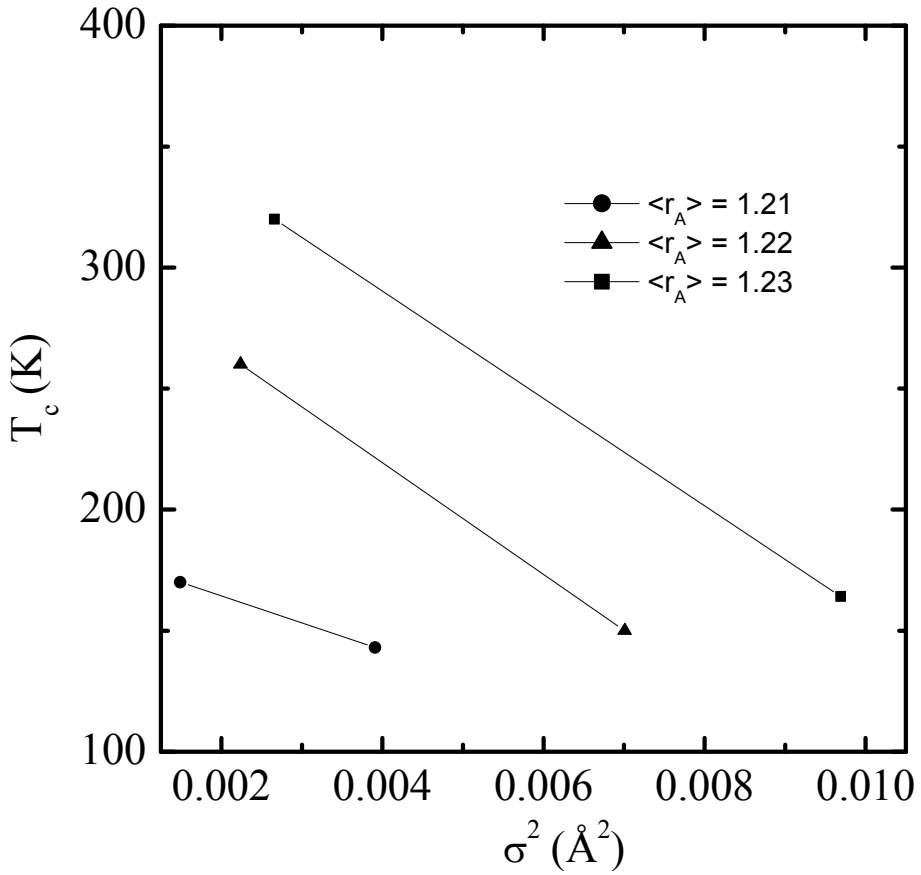

Figure 4.17: Variation of I-M transition temperature (T_p) as a function of varying size-disorder of a pair of samples having constant <r_A> from both the LPCSMO and LPCBMO series.

It is observed from the fig. 4.17 that, the fall in T_c for the set of Sr-Ba doped samples with < r_A> = 1.23 is maximum as compared to samples with < r_A> = 1.22 and 1.21. The samples with maximum drop in T_c possess large variation in the size variance. The values given in Table-3.1 and figs 4.16 and 4.17 reveal that the LPCSMO has more impact of increasing <r_A> on the large enhancement of T_p as the Sr^{2+} concentration increases. In LPCBMO series, though <r_A> increases significantly and should enhance the T_p more than that in LPCSMO series with increasing substitution. However, it is not the

case as the T_p enhancement is slow in LPCBMO series and this may be attributed to the detrimental effect of increasing size-disorder on the T_p.

The Ba being a larger cation puts a strain on the lattice, which is evident from the low rate of rise in T_c and broader nature of transition. The size mismatch at A-site due to larger Ba cation results in the random displacement of oxygen ions and hence influences the Mn-O hybridization [20]. This induces the local spin and position dependent fluctuations in the lattice. The increasing Ba concentration increases the size variance at A site and this affects the motion of electrons significantly. If the size variance at A site increases beyond a limit then structural deformation leads to phase segregation which is evident from the structural studies on $La_{0.4}Pr_{0.3}Ba_{0.3}MnO_3$ sample in which the Pr concentration was increased to enhance the variance for a constant carrier density.

4.4 Conclusions

Effects of competing tolerance factor and size-disorder at A-site on the structural and transport properties have been studied in Sr^{2+} and Ba^{2+} substituted nearly low-bandwidth $La_{0.5}Pr_{0.2}Ca_{0.3}MnO_3$ systems, resulting in the two series as $La_{0.5}Pr_{0.2}Ca_{0.3-x}Sr_xMnO_3$ ($0 \leq x \leq 0.30$) and $La_{0.5}Pr_{0.2}Ca_{0.3-x}Ba_xMnO_3$ ($0 \leq x \leq 0.30$). An increase in substitution of larger cation Ba at Ca site as compared to Sr, results in an enhanced size mismatch, thereby increasing the strain on the lattice and affecting the motion of electrons significantly. This decreases the rate of T_C enhancement due to Ba substitution and results in broader resistive transitions.

References

1. Ramirez A P, J. Phys: Condens. Mater, **9**, 5171 (1997)
2. Coey J M D, Viret M and Von Molnar S, Advances in Phys., **48**, 2, 167 (1999)
3. Von Helmolt R, Wecker J, Holzapsfel B, Schultz L and Samwar K, Phys. Rev. Lett., **71**, 2331 (1993)
4. Gooenough J B, Aust. J. of Phys., **52**, 155 (1999)
5. Rodriguez-Martinez L M and Attfield J P, Phys. Rev. B, **54**, R15622 (1996)
6. Emin D and Holstein T, Phys. Rev. B, **13**, 647 (1976)
7. Ziese Michael, Srinitiwarawong Chatchai, Phys. Rev. B, **58**, 11519 (1998)
8. Coey J M D, Viret M, Ranno L, Ounadjela K, Phys. Rev. Lett., **75,** 3910 (1995)
9. Viret M, Ranno L, Coey J M D, J. Appl. Phys., **81,** 4964 (1997)
10. Gupta A, Gong G Q, Xiao Gang, Duncombe P R, Lecoeur P, Trouilloud P, Wang YY, Dravid V P and Sun J Z, Phys. Rev. B, **54**, 629 (1996)
11. Hwang H Y, Cheong S-W, Ong N P and Batlogg B, Phys. Rev. Lett., **77**, 2041 (1996)
12. Ju Sheng, Sun H, Li Zhen-Ya, Phys Letts A, **300**, 666 (2002)
13. Hielman A K, Xue Y Y, Lorenz B, Campbell B J, Cmaidalka J, Wang R L, Chu C W, Phys. Rev.B, **65**, 214423 (2002)
14. I. E. Dzyaloshinskii, Zh. Eksp. Teor. Fiz. **72**, 1930 (1977) [Sov. Phys. JETP **45**, 1014 (1977)]
15. A. de Andrés, M. García-Hernández, and J. L. Martínez, Phys. Rev. B, **60,** 7328 (1999)
16. E. Dagotto, Takashi Hotta and Adriana Moreo Physics Reports **344**, 1-153, (2003)

17. H. Y. Hwang, S. W. Cheong, N. P. Ong, and B. Batlogg, Phys. Rev. Lett. **77**, 2041 (1996)

18. X. W. Li, A. Gupta, G. Xiao, and G. Q. Gong, Appl. Phys. Lett. **71**, 1124 (1997)

19. J. M. D. Coey, *Philos.* Trans. R. Soc. London, Ser. A*,* **356**, 1539 (1998)

20. H. L. Ju, J. Gopalakrishnan, J. L. Peng, Qi Li, G. C. Xiong, T. Venkatesan, and R. L. Greene, Phys. Rev. B **51**, 6143 (1995)

List of Publications in published in International Journals

1. Size disorder effect in $La_{0.5}Pr_{0.2}(Ca_{0.3-X}Ba_X)MnO_3$ manganite.
   Thaker C. M, Markna J. H., Parmar R.N., Rana D. S., Bhalodia J.A. , Kulkarni N.A., Kuberkar D.G.and Malik S.K
   Thin Solid Film (In Press 2005)

2. IV behavior of superconductor manganite Y-123/$LaAlO_3$/$La_{0.7}Sr_{0.3}MnO_3$ of hetrostructure.
   Sanghamitra Khatua, **C. M. Thaker**, J. John, D.G. Kuberkar, R. Pinto and S. K. Malik.
   Journal of Solid State Phenomena (communicated 2005)

3. Half Metallic Nature up to 200 K with High MR % at Room Temperature in LPSMO Epitaxial Thin Films Grown By Pulsed Laser Deposition.
   J. H. Markna, D. S. Rana, R. N. Parmar, **C. M. Thaker**, J. A. Bhalodia , D. G. Kuberkar, P. K. Misra, L. M. Kukreja and S. K. Malik
   Journal of Electro Ceramics (communicated 2005)

4. Large magnetoresistance in low temperature metallic region of manganites compounds $(La_{0.7-2x}Eu_x)(Ca_{0.3}Sr_x)MnO_3$ $(0.05 \leq x \leq 0.15)$ compounds.
   D. S. Rana, **C. M. Thaker**, K. R. Mavani, D. G. Kuberkar and S. K. Malik.
   Solid State Communications 133, 505**, 2005**

5. Electrical and magnetic properties of Eu and Sr substituted $La_{0.7}Ca_{0.3}MnO_3$.
   D. S. Rana, **C. M. Thaker**, K. R. Mavani, D. G. Kuberkar and S. K. Malik.
   Hyperfine Interaction (In Press 2005)

6. Low temperature Bond Valence Sum study of $La_{2-x}Dy_xCa_{2x}Ba_2Cu_{4+2x}O_z$ oxide superconductors.
   Rohini Parmar, J. H. Markna, D. S. Rana, **C. M. Thaker**, N. A. Shah, J. A. Bhalodia, D. G. Kuberkar, S. Rayaprol, Keka R. Chakraborty, P. S. R. Krishna and M.Ramnadham.
   Journal of Solid State Phenomena (In press 2005)

7. Magnetism and electronic transport of $(La_{0.7-2x}Eu_x)(Ca_{0.3}Sr_x)MnO_3$: Effect of simultaneous size disorder and carrier density.
   D.S. Rana, **C. M. Thaker**, K.R. Mavani, D.G. Kuberkar, Darshan C. Kundaliya and S.K. Malik,
   Journal of Applied Physics 95, 4934 **(2004)**

8. Disorder effects in $(LaTb)_{0.5}(CaSr)_{0.5}MnO_3$ compounds.
   D.S. Rana, K.R. Mavani, **C. M. Thaker**, D.G. Kuberkar, D.C. Kundaliya and S.K. Malik.
   Journal of Applied Physics 95 (2004)

9. Electronic transport, magnetism and magnetoresistance of $(La_{0.7-3x}Tb_x)(Ca_{0.3}Sr_{2x})MnO_3$ $(0.025 \leq x \leq 0.125)$ compounds.
   D. S. Rana, K.R. Mavani, **C. M. Thaker**, D.G. Kuberkar, D.C. Kundaliya, S.K. Malik.
   Journal of Magnetism and Magnetic Materials 271, 215 **(2004)**

10. Ferromagnetism and charge-ordering in $(LaR)_{0.50}(CaSr)_{0.50}MnO_3$ (R=Nd,Eu,Tb) compounds.
    D. G. Kuberkar, D. S. Rana**,** K.R. Mavani, **C. M. Thaker**, Darshan C. Kundaliya and S.K. Malik.
    Journal of Magnetism and Magnetic Materials 272, 1823 **(2004)**

11. Study of 200 MeV Ag ion irradiation effects on oxygen stoichiometry of La-2125 type superconducting thin films using ERDA.
    K. R. Mavani, S. Rayaprol, D. S. Rana, **C. M. Thaker**, D.G. Kuberkar, J. John, R. Pinto, S.V.S. Nageswara Rao, S.A. Khan, S.K. Srivastava, Anjana Dogra, Ravi Kumar, D.K. Avasthi.
    Radiation Measurements 36, 733 **(2003)**

12. Studies on $La_{2-x}Pr_xCa_yBa_2Cu_{4+y}O_z$ (x = 0.1-0.5, y=2x) type mixed oxide superconductors.
S. Rayaprol, K. R. Mavani, D. S. Rana, **C. M. Thaker**, Manglesh Dixit, Shovit Bhattacharya and D.G. Kuberkar.
Solid State Communications 128, 97 **(2003)**

13. Effect of Mo substitution on the superconductivity, flux pinning and critical currents of $La_{1.5}Nd_{0.5}Ca_1Ba_2Cu_5O_z$.
S. Rayaprol, Krushna Mavani, **C. M. Thaker**, D. S. Rana, R.G. Kulkarni, D.G. Kuberkar, Darshan C. Kundaliya and S. K. Mailk.
Physica C 391, 237 **(2003)**

14. Effect of bandwidth and size disorder on the electronic and magnetic properties of $LaMnO_3$ perovskite.
C. M. Thaker, D. S. Rana, Krushna Mavani, S. Rayaprol, M. Shasrabudhe, S. I. Patil, N. A. Kulakarni and D.G. Kuberkar.
Indian Journal of Engineering and Materials Sciences 10, 324 **(2003)**

15. Structural Investigations of La-2125 mixed oxide superconducting system.
S. Rayaprol, Krushna Mavani, D. S. Rana, **C.M. Thaker**, R. S. Thampi, D. G. Kuberkar, R.G. Kulkarni and S. K. Malik.
Journal of Superconductivity 15, 211(**2002)**

16. Effect of Pr-Ca substitution on the transport and magnetic behavior of $LaMnO_3$ perovskite.
C. M. Thaker, S. Rayaprol, Krushna Mavani, D. S. Rana, M. Sahasrabudhe, S.I. Patil, D.G. Kuberkar.
Pramana - Journal of Physics, 58, 1035 **(2002)**

17. Structural studies and T_c dependence in $La_{2-x}Dy_xBa_2Ca_yCu_{4+y}O_z$ type mixed oxide 8superconductors.
S. Rayaprol, Krushna Mavani, **C. M. Thaker**, D. S. Rana, Nilesh A. Kulkarni, Keka Chakravorty, S. K. Paranjape, M. Ramanadham and D.G. Kuberkar.
Pramana - Journal of Physics, 58, 877 **(2002)**